

Field Line Resonance in Two and a Half Dimensions

DRAFT VERSION CREATED ON APRIL 4, 2016

1

© Charles A. McEachern 2016

2



3

The text of this work is licensed under a Creative Commons

Attribution-ShareAlike 4.0 International license.

4

⁵ Acknowledgements

⁶ Acknowledgement placeholder.

⁷ Dedication

⁸ Dedication placeholder.

Abstract

¹⁰ Abstract placeholder.

Contents

¹¹	Acknowledgements	i
¹³	Dedication	ii
¹⁴	Abstract	iii
¹⁵	List of Tables	vii
¹⁶	List of Figures	viii
¹⁷	1 Introduction	1
¹⁸	1.1 Structure of the Present Work	2
¹⁹	2 The Near-Earth Environment	4
²⁰	2.1 The Outer Magnetosphere	4
²¹	2.2 The Inner Magnetosphere	6
²²	2.3 The Ionosphere	8
²³	2.4 Geomagnetic Storms and Substorms	9
²⁴	3 Field Line Resonance	11
²⁵	3.1 Harmonic Structure	14
²⁶	3.2 Azimuthal Modenumber	16
²⁷	3.3 Poloidal and Toroidal Polarizations	18
²⁸	3.4 Giant Pulsations	20
²⁹	3.5 Motivations for the Present Work	21

30	4 Waves in Cold Resistive Plasma	24
31	4.1 Guided Propagation	26
32	4.2 Compressional Propagation	27
33	4.3 High Altitude Limit	29
34	4.4 Implications to the Present Work	30
35	5 “Tuna Half” Dimensional Model	32
36	5.1 Coordinate System	33
37	5.2 Physical Parameter Profiles	37
38	5.3 Driving	40
39	5.4 Maxwell’s Equations	43
40	5.5 Boundary Conditions	47
41	6 Electron Inertial Effects	52
42	6.1 The Boris Factor	53
43	6.2 Parallel Currents and Electric Fields	55
44	6.3 Inertial Length Scales	61
45	6.4 Discussion	62
46	7 Numerical Results	64
47	7.1 Finite Poloidal Lifetimes: Dayside	65
48	7.2 Spatial Distribution of Energy: Dayside	70
49	7.3 Finite Poloidal Lifetimes: Nightside	75
50	7.4 Spatial Distribution of Energy: Nightside	79
51	7.5 Ground Signatures and Giant Pulsations	82
52	7.6 Discussion	86
53	8 Observations	88
54	8.1 Sampling Bias and Event Selection	89
55	8.2 Overall Rate of Pc4 Events	95
56	8.3 Pc4 Events by Mode	99
57	8.4 Pc4 Events Inside and Outside the Plasmapause	103
58	8.5 Poloidal Pc4 Events by Compressional Coupling	104

59	8.6	Pc4 Events by Spectral Width	108
60	8.7	Double-Triggering Events	114
61	8.8	Discussion	115
62	9	Conclusion	116
63	9.1	Summary of Results	116
64	9.2	Future Work	116
65	References		118

⁶⁶ List of Tables

⁶⁷	3.1 IAGA Magnetic Pulsation Frequency Bands	12
⁶⁸	5.1 Typical Parameters for the Tuna Density Profile	38
⁶⁹	5.2 Integrated Atmospheric Conductivity	48

⁷⁰ List of Figures

⁷¹ 2.1	Outer Magnetosphere Cutaway	5
⁷² 2.2	Inner Magnetosphere Cutaway	7
⁷³ 3.1	Alfvén Bounce Frequencies	13
⁷⁴ 3.2	First and Second Harmonic Resonances	15
⁷⁵ 3.3	Large and Small Azimuthal Modenumbers	17
⁷⁶ 3.4	Poloidal Mode Structure	19
⁷⁷ 3.5	Toroidal Mode Structure	20
⁷⁸ 4.1	Compressional Alfvén Wave Cutoff Frequencies	31
⁷⁹ 5.1	Nonorthogonal Dipole Grid	37
⁸⁰ 5.2	Alfvén Speed Profiles	39
⁸¹ 5.3	Ionospheric Conductivity Profiles	40
⁸² 5.4	Decreasing Penetration with Increasing Modenumber	42
⁸³ 5.5	Sym-H for June 2013 Storm	43
⁸⁴ 6.1	Plasma Frequency Profile	54
⁸⁵ 6.2	Electric Field Snapshots	56
⁸⁶ 6.3	Current and Poynting Flux at 100 km	57
⁸⁷ 6.4	Current and Poynting Flux at 1000 km	59
⁸⁸ 6.5	Power Density at the Ionosphere	60
⁸⁹ 6.6	Parallel Electric Fields by Perpendicular Grid Resolution	62
⁹⁰ 7.1	Poloidal and Toroidal Energy: Quiet Day, Typical Plasmasphere	68
⁹¹ 7.2	Poloidal and Toroidal Energy: Quiet Day, Large Plasmasphere	69
⁹² 7.3	Radial Distribution of Poloidal Energy: Quiet Day, Typical Plasmasphere	72
⁹³ 7.4	Radial Distribution of Poloidal Energy: Quiet Day, Large Plasmasphere	73

94	7.5 Radial Distribution of Toroidal Energy: Quiet Day	74
95	7.6 Poloidal and Toroidal Energy: Active Night, Driving at $L = 5$	77
96	7.7 Poloidal and Toroidal Energy: Active Night, Driving at $L = 6$	78
97	7.8 Radial Distribution of Poloidal Energy: Active Night, Driving at $L = 6$	80
98	7.9 Radial Distribution of Toroidal Energy: Active Night	81
99	7.10 Dayside Ground Magnetic Fields	84
100	7.11 Nightside Ground Magnetic Fields	85
101	8.1 Distribution of Usable Van Allen Probe Data: Fine Resolution	91
102	8.2 Distribution of Usable Van Allen Probe Data	92
103	8.3 Distribution of Usable Van Allen Probe Data: $Dst \geq -30 \text{ nT}$	93
104	8.4 Distribution of Usable Van Allen Probe Data: $Dst < -30 \text{ nT}$	94
105	8.5 Pc4 Rate	96
106	8.6 Pc4 Rate: $Dst \geq -30 \text{ nT}$	97
107	8.7 Pc4 Rate: $Dst < -30 \text{ nT}$	98
108	8.8 Pc4 Rate by Mode	100
109	8.9 Pc4 Rate by Mode: $Dst \geq -30 \text{ nT}$	101
110	8.10 Pc4 Rate by Mode: $Dst < -30 \text{ nT}$	102
111	8.11 Pc4 Rate Inside and Outside the Plasmapause	103
112	8.12 Pc4 Rate Inside and Outside the Plasmapause by Mode	104
113	8.13 Poloidal Pc4 Rate by Compressional Coupling	105
114	8.14 Poloidal Pc4 Rate by Compressional Coupling: $Dst \geq -30 \text{ nT}$	106
115	8.15 Poloidal Pc4 Rate by Compressional Coupling: $Dst < -30 \text{ nT}$	107
116	8.16 Poloidal Pc4 Rate by Spectral Width	108
117	8.17 Poloidal Pc4 Rate by Spectral Width: $Dst \geq -30 \text{ nT}$	109
118	8.18 Poloidal Pc4 Rate by Spectral Width: $Dst < -30 \text{ nT}$	110
119	8.19 Toroidal Pc4 Rate by Spectral Width	111
120	8.20 Toroidal Pc4 Rate by Spectral Width: $Dst \geq -30 \text{ nT}$	112
121	8.21 Toroidal Pc4 Rate by Spectral Width: $Dst < -30 \text{ nT}$	113
122	8.22 Dual Poloidal + Toroidal Pc4 Events	115

¹²³ **Chapter 1**

¹²⁴ **Introduction**

¹²⁵ 1859 was a pivotal year in human history. The United States moved steadily toward
¹²⁶ the American Civil War, which would abolish slavery and consolidate the power of
¹²⁷ the federal government. A slew of conflicts in Southern Europe, such as the Austro-
¹²⁸ Sardinian War, set the stage for the unification of Italy. The Taiping Civil War — one
¹²⁹ of the bloodiest conflicts of all time — is considered by many to mark the beginning
¹³⁰ of modern Chinese history. *Origin of Species* was published. The first transatlantic
¹³¹ telegraph cable was laid.

¹³² Meanwhile, ambivalent to humanity, the Sun belched an intense burst of charged parti-
¹³³ cles and magnetic energy directly at Earth. The resulting geomagnetic storm¹ caused
¹³⁴ telegraph systems to fail across the Western hemisphere, electrocuting operators and
¹³⁵ starting fires[36, 98]. Displays of the northern lights were visible as far south as Cuba.

¹³⁶ The Solar Storm of 1859 was perhaps the most powerful in recorded history, but by no
¹³⁷ means was it a one-time event. The Sun discharges hundreds of coronal mass ejections
¹³⁸ (CMEs) per year, of all sizes, in all directions. In fact, a comparably large CME narrowly
¹³⁹ missed Earth in 2012[74]. Had it not, it's estimated it would have caused widespread,
¹⁴⁰ long-term electrical outages, with a damage toll on the order of 10^{12} dollars[68].

¹The Solar Storm of 1859 is also called the Carrington Event, after English astronomer Richard Carrington. He drew a connection between the storm's geomagnetic activity and the sunspots he had observed the day before.

141 The Sun’s extreme — and temperamental — effect on Earth’s magnetic environment
142 makes a compelling case for the ongoing study of space weather. Such research has
143 evolved over the past century from sunspot counts and compass readings to multi-
144 satellite missions and supercomputer simulations. Modern methods have dramatically
145 increased humanity’s understanding of the relationship between the Sun and the Earth;
146 however, significant uncertainty continues to surround geomagnetic storms, substorms,
147 and the various energy transport mechanisms that make them up.

148 The present work focuses in particular on the phenomenon of field line resonance: Alfvén
149 waves bouncing between the northern and southern hemispheres. Such waves play an
150 important part in the energization of magnetospheric particles, the transport of energy
151 from high to low altitude, and the driving of currents at the top of the atmosphere.

152 1.1 Structure of the Present Work

153 Chapter 2 surveys the near-Earth environment. Prominent features of the magneto-
154 sphere are defined. The response of the magnetosphere to transient solar wind events
155 is summarized.

156 Chapter 3 introduces the field line resonance phenomenon, in terms of both the under-
157 lying physics and notable work on the topic. Jargon is introduced to clarify important
158 elements of wave structure. Several open questions about field line resonances (FLRs)
159 are offered as motivations for the present work.

160 Chapter 4 lays the groundwork for a numerical model by exploring the fundamental
161 equations of waves in a cold, resistive plasma — such as Earth’s magnetosphere. Char-
162 acteristic scales are gleaned from the resulting dispersion relations.

163 Chapter 5 presents Tuna, a new two and a half dimensional simulation designed specif-
164 ically for the realistic modeling of FLRs. Tuna’s non-orthogonal geometry, height-
165 resolved ionosphere, novel driving mechanism, and coupling to the atmosphere are ex-
166 plained.

167 Chapter 6 considers the addition of electron inertial effects to Tuna, touches on what
168 can be learned from them, and shows that they incur an unreasonable computational
169 cost. (Electron inertia is neglected in the results presented in other chapters.)

170 Chapter 7 describes the core numerical results of the work, unifying several of the
171 questions posed in Chapter 3. Significant depth is added to past work on finite poloidal
172 lifetimes[66, 80]. Interplay between poloidal-toroidal coupling, shear-compressional cou-
173 pling, and Joule dissipation is considered from several angles.

174 Chapter 8 puts the numerical results in physical context through the analysis of data
175 from the Van Allen Probes mission. FLR occurrence rates are considered in terms of
176 location, mode structure, and polarization – parameters which have been only partially
177 addressed by other recent FLR surveys[17, 72].

178 Chapter 9 briefly summarizes the results shown in the above chapters — the code
179 development, analysis of numerical results, and satellite observation — and suggests
180 further directions.

¹⁸¹ **Chapter 2**

¹⁸² **The Near-Earth Environment**

¹⁸³ From Earth’s surface to a height of a hundred kilometers or so, the atmosphere is a
¹⁸⁴ well-behaved fluid: a collisional ensemble of neutral atoms. Higher up, its behavior
¹⁸⁵ changes dramatically. As altitude increases, solar ultraviolet radiation becomes more
¹⁸⁶ intense, which ionizes atmospheric atoms. Density also decreases, slowing collisional
¹⁸⁷ recombination. Whereas the neutral atmosphere is held against Earth’s surface by
¹⁸⁸ gravity, the motion of charged particles is dominated by Earth’s geomagnetic field, as
¹⁸⁹ well as the electromagnetic disturbances created as that field is hammered by the solar
¹⁹⁰ wind.

¹⁹¹ The present section outlines the structure of the magnetosphere; that is, the region of
¹⁹² space governed primarily by Earth’s magnetic field. Particular emphasis is placed on
¹⁹³ structures which relate closely to field line resonance.

¹⁹⁴ **2.1 The Outer Magnetosphere**

¹⁹⁵ Plasma behavior within Earth’s magnetosphere is ultimately driven by the solar wind: a
¹⁹⁶ hot (~ 100 eV), fast-moving (~ 100 km/s) plasma threaded by the interplanetary magnetic
¹⁹⁷ field (~ 1 nT)¹. The density of the solar wind is on the order of 10^6 /cm³; in a laboratory

¹Listed values correspond to the solar wind at Earth’s orbit.

198 setting, this would constitute an ultra-high vacuum (atmospheric density at sea level is
199 $\sim 10^{19} / \text{cm}^3$), but compared to much of the magnetopause it's quite dense.



Figure 2.1: TODO: The outer magnetosphere...

200 The magnetosphere's outer boundary represents a balance between the solar wind dy-
201 namic pressure and the magnetic pressure of Earth's dipole field. On the dayside, the
202 dipole is compressed, pushing this boundary to within about $10 R_E$ of Earth². The
203 nightside magnetosphere is stretched into a long tail which may exceed $50 R_E$ in width
204 and $100 R_E$ in length.

205 When the interplanetary magnetic field opposes the geomagnetic field at the nose of
206 the magnetosphere, magnetic reconnection occurs. Closed magnetospheric field lines
207 "break," opening up to the interplanetary magnetic field³. They then move tailward

²Distances in the magnetosphere are typically measured in units of Earth radii: $1 R_E \equiv 6378 \text{ km}$.

³Closed field lines connect at both ends to the magnetic dynamo at Earth's core. Open field lines meet Earth at only one end; the other connects to the interplanetary magnetic field. The distinction is important because charged particle motion is guided by magnetic field lines, as discussed in Chapter 3.

208 across the poles, dragging their frozen-in plasma with them⁴. Reconnection in the tail
209 allows magnetic field lines to convect back to the day side, across the flanks. This
210 process is called the Dungey cycle[23].

211 Viewed from the north, the Dungey cycle involves a clockwise flow of flux and plasma on
212 the dusk side and a counterclockwise flow on the dawn side. The motion is accompanied
213 by a convection electric field, per Ohm's law⁵.

214 **TODO:** Jets from magnetic reconnection... release of magnetic tension!

215 Consistent with Ampère's law, the interplanetary magnetic field is separated from the
216 magnetosphere by a current sheet: the magnetopause. On the dayside, the magne-
217 topause current flows duskward; on the nightside, it flows downward around the mag-
218 netotail.

219 Plasma within the tail is cool ($\sim 100 \text{ eV}$) and rarefied ($\sim 10^{-2} / \text{cm}^3$). Earth's dipole is
220 significantly deformed in the magnetotail; field lines in the northern lobe of the tail
221 points more or less Earthward, and vice versa. The two lobes are divided by the plasma
222 sheet, which is comparably hot ($\sim 10^3 \text{ eV}$) and dense ($\sim 1 / \text{cm}^3$). The plasma sheet
223 carries a duskward current which connects to the magnetopause current.

224 2.2 The Inner Magnetosphere

225 Within about **TODO:** $L \sim 10$ (where L is the McIlwain parameter⁶), the dipole
226 magnetic field is not appreciably deformed by the solar wind. As a result, the structures
227 in the inner magnetosphere follow closely from the motion of charged particles in an
228 ideal dipole field.

⁴In the outer magnetosphere (as well as most of the inner magnetosphere), collisions are so infrequent that magnetic flux is said to be “frozen in” to the plasma. Charged particles move freely along magnetic field lines, but cannot cross from one line to another. Compression of the magnetic field is synonymous with compression of the ambient plasma.

⁵In the case of an ideal plasma, Ohm's law takes the form $\underline{E} + \underline{U} \times \underline{B} = 0$.

⁶The McIlwain parameter L is used to index field lines in Earth's dipole geometry: $L \equiv \frac{r}{\sin^2 \theta}$ for colatitude θ and radius r in Earth radii. For example, the $L = 5$ field line passes through the equatorial plane at a geocentric radius of $5 R_E$, then meets the Earth at a colatitude of $\arcsin \sqrt{\frac{1}{5}} \sim 27^\circ$ (equally, a latitude of $\arccos \sqrt{\frac{1}{5}} \sim 63^\circ$).

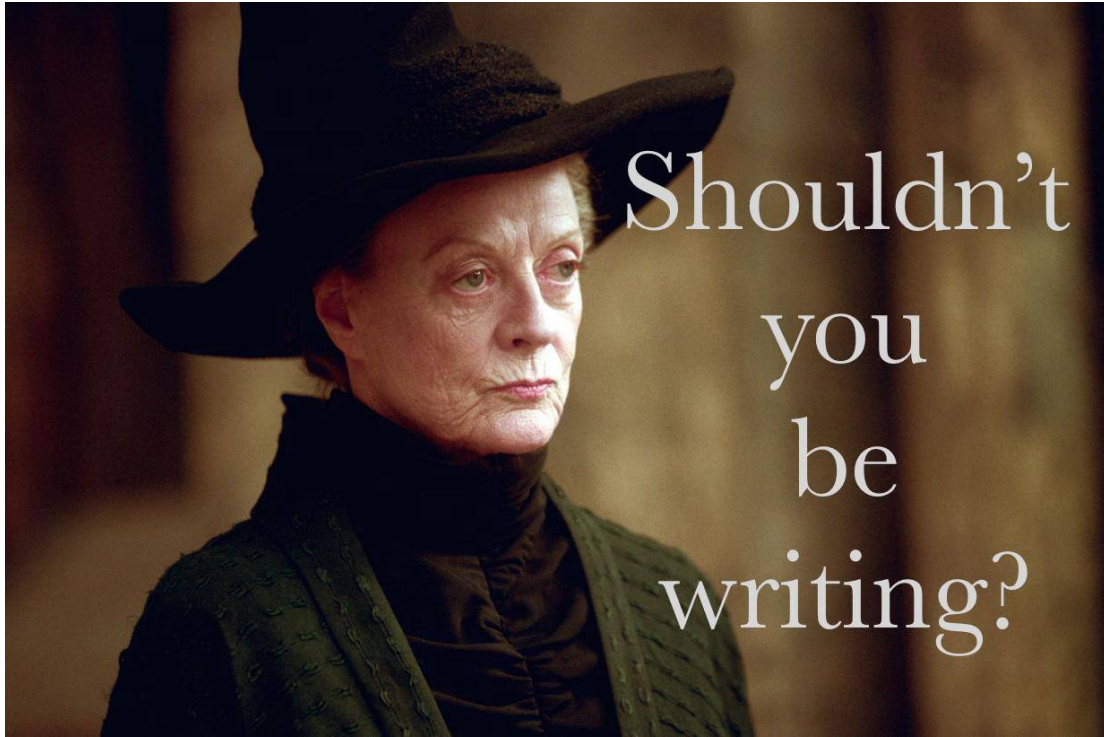


Figure 2.2: TODO: The inner magnetosphere...

- 229 The plasmasphere — a cold (~ 1 eV), dense ($10^2 / \text{cm}^3$ to $10^4 / \text{cm}^3$) torus of corotating
230 plasma — is formed by the outward drift of atmospheric ions along magnetic closed
231 field lines. Its outer boundary, is thought to represent a balance between the corotation
232 electric field (per the rotation of Earth's magnetic dipole) and the convection electric
233 field (associated with the convection of magnetic flux during the Dungey cycle). Particle
234 density drops sharply at the edge of the plasmasphere; the boundary is called the
235 plasmapause. The plasmapause typically falls around $L = 4$, though during prolonged
236 quiet times it can extend to $L = 6$ or larger.
- 237 Energetic particles trapped within the inner magnetosphere are divided into two popu-
238 lations.
- 239 The Van Allen radiation belts are made up of particles with energy above 10^5 eV or
240 so. The inner belt ($L \lesssim 2$) is primarily composed of protons, the decay remnants of

241 neutrons freed from the atmosphere by cosmic rays. The outer belt ($L \gtrsim 4$) is primarily
242 composed of high-energy electrons.

243 Particles with energies of 10^3 eV to 10^5 eV make up the ring current, which extends
244 from $L \sim 3$ to $L \sim 5$. Gradient-curvature drift carries ions and electrons in opposite
245 directions; the net result is a westward current. During quiet times, the ring current
246 causes magnetic a southward magnetic field on the order of 1 nT at Earth's equator⁷.

247 2.3 The Ionosphere

248 Earth's neutral atmosphere is an excellent insulator. Collisions are so frequent that
249 charged particles quickly thermalize and recombine. The breakdown of air molecules
250 into a conductive plasma (as happens during a lightning strike, for example) requires
251 electric fields on the order of 10^9 mV/m.

252 Currents are also suppressed by the magnetosphere. In the absence of collisions, elec-
253 trons and ions drift alongside one another in response to an electric field, creating no
254 net current perpendicular to the magnetic field⁸. Magnetic field lines are (to a good
255 approximation) equipotential contours; electric fields do not form along them to drive
256 parallel currents.

257 The ionosphere is a sweet spot between the two regimes. Collisions are frequent enough
258 to disrupt the drift of ions, but not frequent enough to immobilize the electrons. The
259 result is nonzero Pedersen and Hall conductivity, corresponding to current along the
260 electric field and in the $\underline{B} \times \underline{E}$ direction respectively. Collisions in the ionosphere
261 also give rise to a finite parallel conductivity, allowing for the formation of potential
262 structures along the magnetic field line.

263 **TODO: Field-aligned currents depend on the level of geomagnetic activity... but do**
264 **they ever completely go away?**

⁷For comparison, Earth's dipole field points north at the equator with a magnitude over 10^4 nT.

⁸The so-called E -cross- B drift is associated with a velocity of $\underline{U} = \frac{1}{B^2} \underline{E} \times \underline{B}$, independent of a charged particle's mass or sign.

265 The convection electric field (associated with the Dungey cycle, Section 2.1) drives Ped-
266 ersen currents in the ionosphere. It is these currents that give rise to the strongest mag-
267 netic fields on the ground. Pedersen currents flow downward on the flanks and duskward
268 across the poles. The currents remain divergence-free by connecting to field-aligned cur-
269 rents at the edges of the polar cap. The field-aligned currents, in turn, connect to the
270 magnetopause current, the cross-tail current, and the (partial) ring current.

271 When electron density is low, thermal velocities may be unable to carry enough current
272 to satisfy $\nabla \cdot \underline{J} = 0$. This leads to the formation of potential structures along geomagnetic
273 field lines in the ionosphere. Such structures accelerate particles along magnetic field
274 lines, leading to the precipitation of energetic particles into the atmosphere. As the
275 particles thermalize, they excite atmospheric atoms. The resulting spontaneous emission
276 is often in the visible spectrum, giving rise to the aurora.

277 **TODO:** Particles can also be excited by Alfvén waves... this probably goes in Chapter 3.

278

279 **2.4 Geomagnetic Storms and Substorms**

280 The quiet geomagnetic behavior described above is periodically disturbed by transient
281 solar phenomena such as corotating interaction regions (CIRs) and coronal mass ejec-
282 tions (CMEs). CMEs, as noted in Chapter 1, are bursts of unusually dense solar wind
283 which are ejected from regions of high magnetic activity on the Sun; they are most
284 common at the height of the eleven-year solar cycle. CIRs, on the other hand, occur
285 when a relatively fast region of the solar wind catches up to an earlier and slower-moving
286 pocket of solar wind, resulting in a pair of shockwaves.

287 During a storm, increased solar wind intensity results in enhanced magnetic reconnection
288 on the dayside. As the newly-opened field lines are swept tailward, the convection
289 electric field is strengthened. The plasmasphere — the outer boundary of which is
290 set by a balance between the convection electric field and the (more or less constant)
291 corotation electric field — sheds its outer layers. A large number of energetic particles
292 are also injected into the ring current[70].

293 The strength of the storm is gauged by the size of the magnetic perturbation created
294 by the ring current⁹. A small storm has a magnitude of 50 nT to 100 nT. Large storms
295 may reach 250 nT to 500 nT. The Carrington Event, mentioned in Chapter 1, is thought
296 to have exceeded 1700 nT[98].

297 The main phase of a storm typically lasts for several hours. Storm recovery — the grad-
298 ual return of the storm index to zero — typically lasts several days. The plasmapause
299 refilling occurs on timescales of **TODO: ???**. Geomagnetic storms occur tens of times
300 per year at the height of the solar cycle, and just a few times per year otherwise.

301 Whereas storms are prompted by large solar wind events on the dayside, geomagnetic
302 substorms are primarily a nightside occurrence. As flux accumulates in the tail, mag-
303 netic tension builds in the stretched field lines. A substorm is an impulsive release of
304 that tension.

305 **TODO: Phases of a substorm.** Definition of a substorm comes from [1]. Revised by [71].

306

307 At substorm onset, a burst of reconnection occurs in the tail. A jet of plasma is launched
308 Earthward from the reconnection site (and another is launched tailward, and lost to the
309 solar wind). The Earthward plasma injection injects particles into the ring current.
310 The outer radiation belt is depleted, then repopulated. Energetic particles precipitate
311 into the atmosphere, giving rise to a distinctive **TODO: hour-long** sequence of auroral
312 signatures.

313 Concurrent with substorm onset, impulsive Alfvén waves are observed with periods of
314 a minute or two. The precise ordering of events — whether reconnection causes the
315 waves, or vice versa, or if they share a common cause — remains controversial.

316 Each substorm lasts several hours, including the time it takes for the ring current to
317 return to pre-substorm levels. Several substorms may occur per day during quiet times.
318 During a storm, substorms become far more frequent; by the time one has ended,
319 another may have already begun.

⁹The most commonly used storm index is Dst, which is computed hourly using measurements from several ground magnetometers near the equator. The Sym-H index, used in Section 5.3, is computed once per minute.

320 **Chapter 3**

321 **Field Line Resonance**

322 The motion of a charged particle in a dipole field can be described in terms of three
323 fundamental motions. The first is cyclotron motion: a particle orbits around a magnetic
324 field line in accordance with the Lorentz force. The second is bounce motion: while
325 orbiting, the particle moves along the field line like a bead on a wire, back and forth
326 between the northern and southern hemispheres¹. The third is drift motion: as particles
327 orbit and bounce, they also move azimuthally around Earth per the gradient-curvature
328 drift.

329 Characteristic timescales for each of the above motions depend on particle energy. Elec-
330 tron cyclotron motion is on the order of TODO: ... in the ionosphere, and closer to
331 TODO: ... in the tail; ions gyrate slower by three orders of magnitude due to their
332 larger mass. TODO: Bounce... Drift...

333 Wave-particle resonance arises when a particle's periodic motion matches with the fre-
334 quency of a coincident electromagnetic wave[25, 65, 76, 87]. In the particle's rest frame,
335 the wave then appears as a net electric field. This allows a net movement of energy

¹As a particle approaches Earth, it experiences an ever-stronger magnetic field. The particle's perpendicular kinetic energy increases in proportion with the magnetic field in order to conserve its first adiabatic invariant. When the perpendicular kinetic energy can no longer increase — that is, when the parallel kinetic energy is zero — the particle bounces back. (If the parallel kinetic energy is sufficiently large, the particle doesn't bounce; it precipitates into the atmosphere.)

336 between the wave and the particle. The interaction is analogous to a surfer moving
 337 along with — and being accelerated by — a wave in the ocean.

338 In the present work, the waves in question are field line resonances (FLRs). An FLR
 339 is a standing harmonic on a geomagnetic field line. It can also be envisioned as a
 340 superposition of traveling waves, reflecting back and forth between its northern and
 341 southern foot points at the conducting ionosphere. These waves travel at the Alfvén
 342 speed². The fundamental equations of field line resonance were presented by Dungey in
 343 1954[22]; since then, they have remained a topic of active study.

344 So-called ultra low frequency waves — of which FLRs are a subset — are categorized
 345 by morphology. Continuous (long-lived) pulsations are termed Pc, while irregular pul-
 346 sations are called Pi. Within each are a number of frequency bands; see Table 3.1[46].

Table 3.1: IAGA Magnetic Pulsation Frequency Bands

	Pc1	Pc2	Pc3	Pc4	Pc5	Pi1	Pi2
Period (s)	0.2–5	5–10	10–45	45–150	150–600	1–40	40–150
Frequency (mHz)	200–5000	100–200	22–100	7–22	2–7	25–1000	7–25

347 FLRs fall into the Pc3, Pc4, and Pc5 ranges. The present work focuses specifically
 348 on the Pc4 band: waves with periods of a minute or two. Frequencies in the Pc4
 349 range typically coincide with Alfvén bounce times³ near the plasmapause: $L \sim 4$ to
 350 $L \sim 6$ [3, 17, 26, 57]⁴. In fact, the large radial gradients in the Alfvén speed near the
 351 plasmapause act as an effective potential well, trapping FLRs[16, 51, 54, 55, 64, 90].

352 In addition to being radially localized, FLRs in the Pc4 frequency band (also called Pc4
 353 pulsations, or just Pc4s) are localized in magnetic local time (MLT⁵). They have also

²The Alfvén speed is given by v_A is given by $v_A^2 \equiv \frac{B^2}{\mu_0 \rho}$, where B is the magnitude of the magnetic field, μ_0 is the magnetic constant, and ρ is the mass density of the ambient plasma. It can vary by several orders of magnitude over the length of a magnetic field line.

³The Alfvén frequency is the inverse of the Alfvén bounce time: $\frac{2\pi}{\omega_A} \equiv \oint \frac{dz}{v_A}$.

⁴Not coincidentally, these are the same L -shells where the Van Allen Probes spend most of their time; see Chapter 8.

⁵Noon points toward the Sun and midnight away from it, with 06:00 and 18:00 at the respective dawn and dusk flanks.

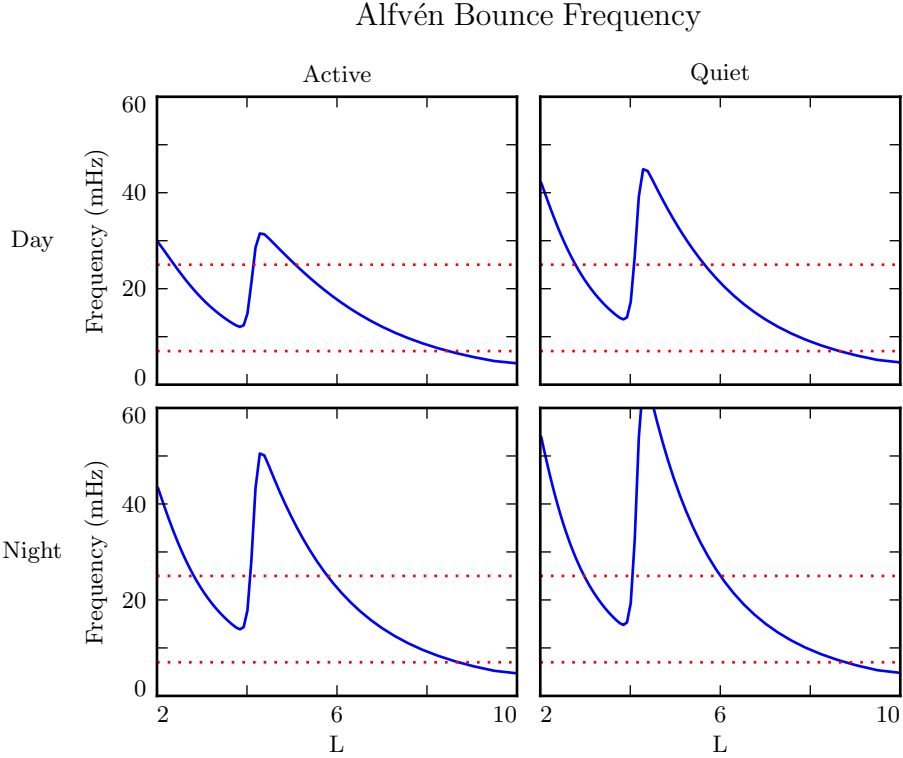


Figure 3.1: The above are bounce frequencies for an Alfvén wave moving back and forth along a geomagnetic field line. Alfvén speeds are computed based on profiles from Kelley[49], as discussed in Section 5.2. Notably, the bounce frequency depends significantly on the position of the plasmasphere, taken here to be at $L = 4$. Dotted lines indicate the Pc4 frequency range: 7 mHz to 25 mHz.

354 been shown to occur preferentially on the dayside, during storms or storm recovery[3,
 355 17, 26, 53, 57, 99].

356 In the inner magnetosphere, the Alfvén frequency — and thus the frequency of FLRs
 357 — often coincides with integer or half-integer⁶ multiples of particle drift frequencies[18].
 358 The resulting wave-particle interactions can give rise to significant energization and
 359 radial diffusion of the particles. In some cases, the waves also include an electric field
 360 parallel to the background magnetic field, contributing to the precipitation of energetic
 361 particles into the neutral atmosphere[33, 34, 95, 105].

⁶See Section 3.1.

362 The present chapter introduces the structural characteristics of FLRs, how those charac-
363 teristics affect wave behavior, and several unresolved questions related to that behavior.

364 **TODO:** The polarization of long-period Alfven waves is rotated by $\sim 90^\circ$ when passing
365 through the ionosphere[42]. A wave that is azimuthally polarized in space is polarized
366 north-south on the ground, and vice versa. It has been noted specifically that Pgs
367 exhibit east-west polarized ground signatures[94].

368 **TODO:** Other planets[32]? Seems exciting but maybe not relevant.

369 3.1 Harmonic Structure

370 Wave structure along a geomagnetic field line is indicated by harmonic number. The
371 first (or fundamental) harmonic has a wavelength twice as long as the field line. It
372 exhibits an antinode in the perpendicular electric field at the equator, along with a
373 node in the perpendicular magnetic field. The second harmonic is a single wavelength
374 along the field line. Its perpendicular magnetic perturbation has an antinode at the
375 equator, while its perpendicular electric field has a node. Figure 3.2 shows a qualitative
376 sketch of each: a series of snapshots in time, in the rest frame of the wave. Perpendicular
377 electric and magnetic field perturbations are shown in blue and red respectively.

378 A first-harmonic FLR that is periodic or localized in the azimuthal direction is conducive
379 to drift-resonant wave-particle interactions[18, 77]. The particle is like a child on a swing:
380 whenever the path of the particle (or child) gets close to the wave (parent), it gets a
381 push, and always in the same direction. The wave fields spend half its time pointing
382 the other direction, just as the parent must shift their weight backward to get ready for
383 the next push, but at that point the particle (child) is far away.

384 Second-harmonic FLRs interact with particles through the drift-bounce resonance, which
385 is slightly more complicated. As the particle drifts azimuthally, it also zig-zags north-
386 south. The combination of those two periodic motions must align with the phase of
387 the wave electric field. An example path is shown by the purple line in Figure 3.2: the
388 particle experiences a rightward electric field throughout the wave’s oscillation.

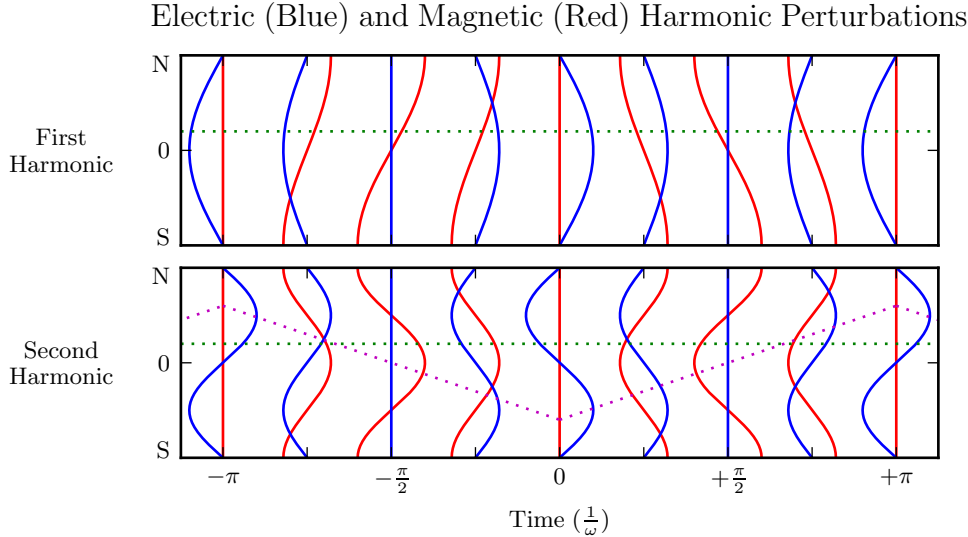


Figure 3.2: The first (or fundamental) harmonic has an antinode in its perpendicular electric field (blue) at the equator, along with a node in its perpendicular magnetic field perturbation (red). A single satellite can identify the first harmonic by the relative phase of the electric and magnetic field perturbations: an observer north of the equator (green) will see the magnetic field perturbation lead the electric field by 90° . The second harmonic is the opposite: it has an electric field node at the equator, and an observer north of the equator will see the magnetic field perturbation lag the electric field by 90° . The purple line sketches the path of a particle in drift-bounce resonance; in the particle's rest frame, the electric field is always to the right. **TODO:** Actually, toroidal waves are flipped — Faraday's law gives $\frac{\partial}{\partial t} B_x \sim \frac{\partial}{\partial z} E_y$ but $\frac{\partial}{\partial t} B_y \sim -\frac{\partial}{\partial z} E_x$.

The drift and drift-bounce resonance conditions are written, respectively[91]:

$$\omega - m\omega_D = 0 \quad \text{and} \quad \omega - m\omega_D = \omega_B \quad (3.1)$$

389 Where ω is the frequency of the wave, ω_D and ω_B are the particle's drift and bounce
390 frequencies respectively, and m is the wave's azimuthal modenumber, as discussed in
391 Section 3.2.

392 In principle, the first and second harmonics can be distinguished by their frequencies,
393 even from a single-point observation[15, 35]. In practice, however, this is not a reliable

394 approach[92]. There are significant uncertainties surrounding the number density profile
395 — and thus the Alfvén speed profile — along a geomagnetic field line.

396 Harmonic structure can also be deduced by noting the phase offset between the wave
397 magnetic field and its electric field (or the plasma velocity)[17, 94]. In Figure 3.2,
398 the green line indicates an observer just north of the magnetic equator. For the first
399 harmonic, the observer sees the electric field waveform lead the magnetic field by a
400 phase of 90° ; for the second harmonic, the electric field waveform lags by 90° . (South
401 of the equator, the signs are reversed.) Notably, this approach has only become viable
402 with the advent of satellites carrying both electric and magnetic field instrumentation,
403 such as THEMIS in 2007[4] and the Van Allen Probes⁷ in 2012[88].

404 Strictly speaking, the the phase offset of the electric and magnetic fields does not provide
405 the harmonic number — only its parity. It's reasonably safe to assume that an even mode
406 is the second harmonic; the second harmonic is by far the most commonly observed[45,
407 85, 93], due in part to its excitement by the antisymmetric balloon instability[9, 11,
408 13, 87]. However, the distinction between the first and third harmonics is not always
409 clear; this issue is discussed further in Chapter 8. Higher harmonics than that are not
410 expected in the Pc4 frequency band.

411 TODO: Second-harmonic FLRs are unlikely to cause ground signatures[94].

412 TODO: Dai found a nice event[18] that was unambiguously determined to be a fundamental-
413 mode Pc4 in drift-resonant interaction with $\sim 10^5$ eV ions. Consistent with [96]. Other
414 observations of odd harmonics: [106, 27].

415 3.2 Azimuthal Modenumber

416 The wavelength of an FLR in the azimuthal direction is indicated by its azimuthal
417 wavelength. A wave with modenumber m has an azimuthal wavelength that spans $\frac{24}{m}$
418 hours in MLT.

⁷The Van Allen Probes were previously called RBSP, for Radiation Belt Storm Probes.

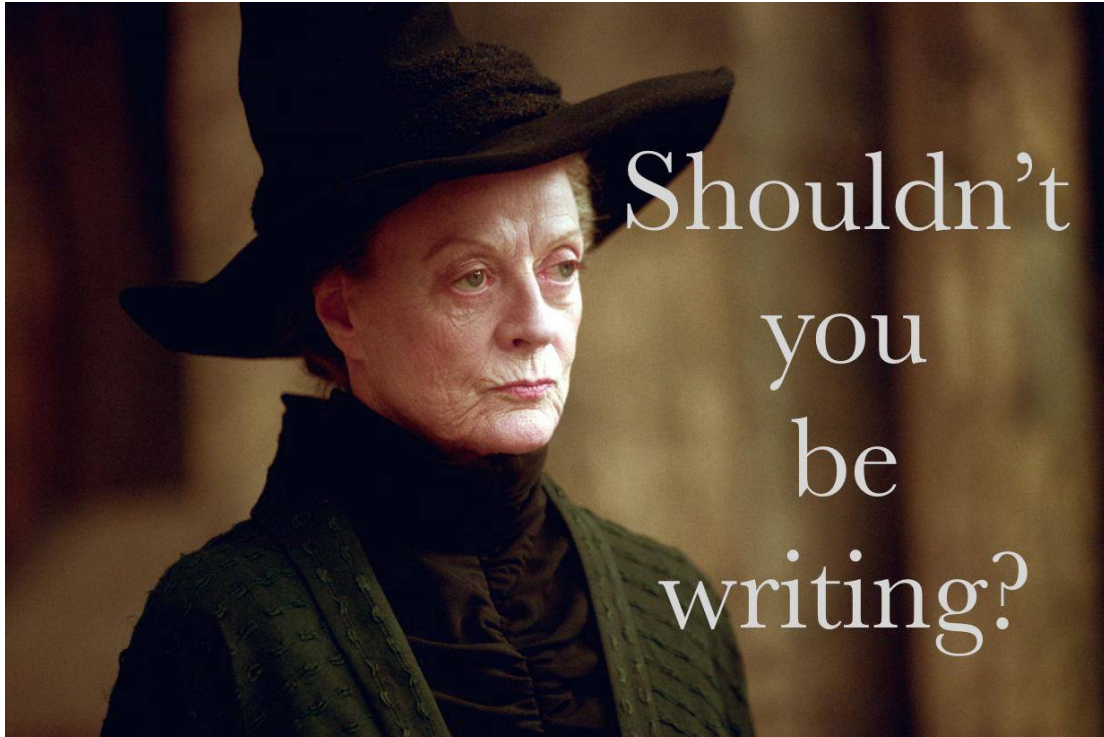


Figure 3.3: TODO: Large and small azimuthal modenumbers.

- 419 Waves with small azimuthal modenumbers ($0 < m < 10$) are typically driven by broad-
420 band energy sources at the magnetosphere's boundary, such as variations in the so-
421 lar wind pressure[19, 39, 50, 109, 110], sporadic magnetic reconnection[43], or Kelvin-
422 Helmholtz waves on the magnetopause[10, 59, 86]. In the low- m regime, the shear and
423 compressional Alfvén waves are coupled, which allows energy to move across field lines
424 until the driving frequency lines up with the local Alfvén frequency[61]. Because of their
425 broadband energy source, low- m FLRs often have a mishmash of frequencies present in
426 their spectra[17].
- 427 When the azimuthal modenumber is large (or, equally, when the azimuthal wavelength
428 is small), the shear and compressional Alfvén waves are decoupled[15, 80]⁸. As a result,
429 FLRs must be driven from within the magnetosphere. Proposed energy sources include

⁸Equally, the strength of a wave's parallel component hint at its modenumber, a point which is revisited in Chapter 8.

430 phase space gradients near the plasmapause[18], particularly as the plasmasphere refills
431 after a storm or substorm[26, 56].

432 The ionosphere is known to attenuate waves with small spatial extent in the perpendic-
433 ular direction[44, 104, 108]. As a result, FLRs may create no signature on the ground if
434 their azimuthal modenumber is large. For example, a recent paper by Takahashi shows
435 a strong (2 nT at $L \sim 10$), clear resonance with $|m| \gtrsim 70$ and no corresponding ground
436 signature[92].

Southwood[87] and Glassmeier[30] show that a low frequency wave passing through the ionosphere on its way to Earth will be attenuated per

$$\frac{B_E}{B_I} = \frac{\Sigma_H}{\Sigma_P} \exp\left(-m \frac{R_I - R_E}{R_E \sin \theta}\right) \quad (3.2)$$

437 Where B_E and B_I are the magnetic field strengths at R_E (Earth's surface, 6783 km
438 geocentric) and R_I (the ionosphere, \sim 6900 km geocentric) respectively. The integrated
439 ionospheric Pedersen and Hall conductivities, Σ_P and Σ_H , are typically within a factor
440 of two of one another. Field lines near the plasmapause can be traced to Earth at
441 $\sin \theta \sim 0.4$. That is, by the time it reaches the ground, the magnetic field from an FLR
442 with $m = 10$ is weaker by a factor of two; at $m = 100$, the factor is closer to 100.

443 3.3 Poloidal and Toroidal Polarizations

444 Based on polarization, each FLR can be classified as either poloidal or toroidal. The
445 poloidal mode is a field line displacement in the meridional plane, as shown in Figure 3.4,
446 with an accompanying electric field in the azimuthal direction. The toroidal mode's
447 magnetic displacement is azimuthal, per Figure 3.5; the associated electric field is in the
448 meridional plane.

449 Both poloidal and toroidal waves are noted for their ability to contribute to the energiza-
450 tion and radial diffusion of trapped particles. The poloidal mode interacts more strongly,

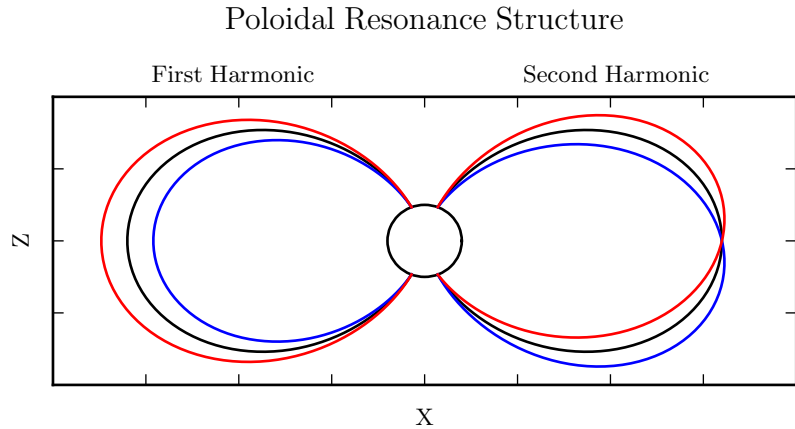


Figure 3.4: The poloidal resonance is a magnetic field in the meridional plane. The displacement is radial near the equator, and can be accompanied by enhancement in the parallel magnetic field near the ionosphere. The first harmonic is shown on the left, and the second harmonic on the right. Lines are colored red and blue only to contrast with the unperturbed black field line.

451 since its electric field is aligned with the trapped particles’ drift motion. Poloidally-
 452 polarized waves are also more prone to creating magnetic signatures on the ground, due
 453 to ducting in the ionosphere[28, 37].

454 Toroidal modes have been shown to far outnumber poloidal modes[3]. Perhaps not
 455 coincidentally, poloidally-polarized waves rotate asymptotically to the toroidal mode[66,
 456 67, 80]. Poloidal waves with low azimuthal modenumber — such as those driven by
 457 broadband sources at the magnetopause — rotate on timescales comparable to their
 458 oscillation periods.

459 **TODO:** Fishbone instability[12, 69]. Like the poloidal mode, but for lab plasmas.

460 **TODO:** Poloidal and toroidal modes are coupled by the ionospheric Hall conductivity[48].
 461 The Hall conductivity also increases the “ringtime” of these resonances, allowing them
 462 to oscillate through the inductive process rather than be dissipated as Joule heating[102].

463

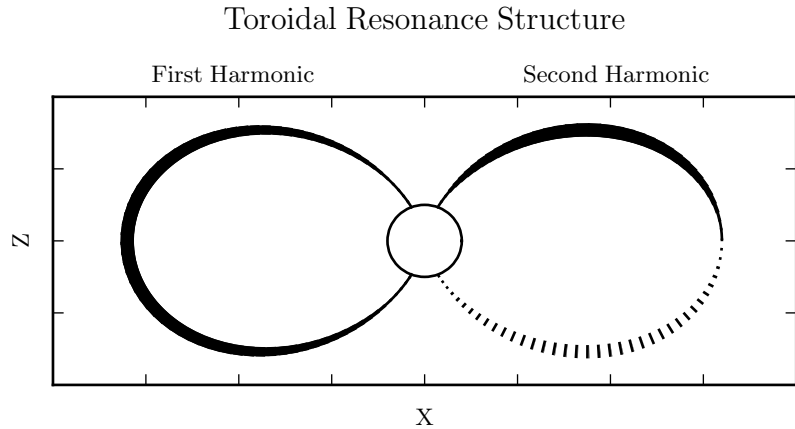


Figure 3.5: A toroidally-polarized FLR has a magnetic perturbation in the azimuthal direction, as shown. Bold lines are taken to be above the page, and dotted lines below the page, with the displacement indicated by the line’s width. The first harmonic — where the entire field line oscillates in and out of the page — is shown on the left. The second harmonic is on the right, with northern and southern halves perturbed in opposite directions.

464 TODO: Toroidal modes show a clear frequency dependence with L . Poloidal modes less
465 so. Citation...?

466 3.4 Giant Pulsations

467 The study of geomagnetic pulsations long predates satellites, sounding rockets, or even
468 the word “magnetohydrodynamics”⁹. Large, regular oscillations in the magnetic field
469 were noted as early as 1901[5]. Eventually, the term “giant pulsation,” or Pg, arose to
470 describe such pulsations.

471 On the ground, Pgs are notable for their strikingly sinusoidal waveforms, their eastward
472 drifts, and their specific occurrence pattern: Pgs are typically seen pre-dawn, at latitudes
473 of 60° to 70° . Pgs generally fall into the Pc4 frequency band¹⁰. Their harmonic structure

⁹The term was first used by Alfvén in the 1940s[2].

¹⁰The Pc4 range is periods of 45 s to 140 s, while Pgs are often said to range from 60 s to 200 s[7].

474 was a source of controversy for decades, but recent multisatellite observations seem to be
475 in agreement that they are odd harmonics, probably fundamental[31, 41, 52, 53, 91, 94].
476 They are poloidally polarized, with modenumbers $10 \lesssim m \lesssim 40$ [29, 41, 77, 83, 94].

477 Whereas FLRs are waves in space which may produce ground signatures, “giant pulsation”
478 refers to the ground signature specifically¹¹. That is, Takahashi’s satellite ob-
479 servation of a sinusoidal, morningside, high- m , fundamental poloidal resonance was not
480 classified as a Pg because it did not produce a signal on the ground[92].

481 **TODO:** Pgs are localized to within 2° to 5° in latitude[72, 91, 100].

482 Due to their remarkably clear waveforms, Pgs are typically found by “visual inspection
483 of magnetometer data”[72]. Over the course of the past century, a number of multi-year
484 (sometimes multi-decade[7]) surveys have totaled nearly one thousand Pg events. On
485 average, a ground magnetometer near 66° magnetic latitude observes ~ 10 Pg events per
486 year[7, 40, 82, 89]. Observations are not distributed uniformly; rather, giant pulsations
487 become more common near the equinox and during times of low solar activity.

488 Unlike Pc4 pulsations in general, Pgs show no particular correlation with storm phase[72].
489 However, they do often occur as the magnetosphere recovers from a substom[72, 83].

490 3.5 Motivations for the Present Work

491 A great deal has been learned — and continues to be learned — through observations of
492 field line resonance. However, the cost-to-benefit ratio is climbing. As summarized in the
493 sections above, FLR behavior depends significantly on harmonic structure, azimuthal
494 modenumber, and polarization — not to mention frequency, spectral width, and so
495 on. With each degree of freedom comes the necessity for an additional simultaneous
496 observation.

¹¹Historically, the wave designations shown in Table 3.1 all referred to ground phenomena. Over time, they have come to describe satellite observations as well, including those without corresponding signatures on the ground.

497 Similarly, as FLRs have been shown to depend on ever-more-specific magnetospheric
498 conditions, analytical techniques have fallen out of favor. The height-resolved iono-
499 sphere, the multidimensional Alfvén speed profile, and the inconvenient geometry com-
500 bine to create a problem beyond the reasonable purview of pencil and paper.

501 That is, the topic of field line resonance is ripe for numerical modeling.

502 Past models of the magnetosphere have been ill-suited for the consideration of FLRs.
503 Reasons include overly-simplified treatment of the ionospheric boundary, no consider-
504 ation of the plasmapause, limited range in m , and the inability to compute ground
505 signatures. Chapter 5 presents a model which addresses these issues, allowing the com-
506 putation of field line resonance with unparalleled attention to realism.

507 The model allows a bird’s-eye view of the structure and evolution of FLRs. As such,
508 not only can several open questions be addressed, but their answers serve to unify a
509 number of seemingly-disparate properties described in the sections above.

510 The rotation of poloidally-polarized waves to the toroidal mode is investigated. Par-
511 ticular attention is paid to the importance of azimuthal modenumber and ionospheric
512 conductivity. The interplay between said rotation and the transport of energy across
513 field lines — which also depends on azimuthal modenumber — is considered as well.

514 By their nature, drifting particles have the potential to spur wave-particle interactions
515 at all MLT. However, Pc4 observations are strongly peaked on the dayside. In a 2015
516 paper, Dai notes, “It is not clear why noncompressional [high- m] Pc4 poloidal waves,
517 which are presumably driven by instability within the magnetosphere, preferentially
518 occur on the dayside”[17]. Motoba, later that year, echoes, “It is unclear whether other
519 generation mechanisms of fundamental standing waves ... can explain the localization
520 of Pgs in local time”[72]. This, too, is considered numerically: to what degree is field
521 line resonance affected by the (day-night asymmetric) conditions of the ionosphere?

522 **TODO:** Transition... With the above in mind, what data would be super helpful?

523 It’s been shown that a ground magnetometer 66° north of the magnetic equator observes
524 ~10 Pg events per year. It’s also been shown that poloidal Pc4s are rare compared to
525 toroidal ones, and that most poloidal Pc4s are even harmonics. However, little attention

526 has been paid to how these rates line up with one another. Given the relative occurrence
527 rate of poloidal and toroidal waves, of odd and even harmonics, and of diffuse and sharp
528 spectral peaks, just how unusual are giant pulsations?

529 **Chapter 4**

530 **Waves in Cold Resistive Plasma**

531 Before delving into the implementation of the numerical model, it's instructive to consider the fundamental equations of waves in a cold, resistive plasma.

The evolution of electric and magnetic fields is governed by Ampère's law and Faraday's law. Notably, the present work takes the linearized versions of Maxwell's equations; the vectors \underline{E} and \underline{B} indicate perturbations above the zeroth-order magnetic field.

$$\underline{\epsilon} \cdot \frac{\partial}{\partial t} \underline{E} = \frac{1}{\mu_0} \nabla \times \underline{B} - \underline{J} \quad \frac{\partial}{\partial t} \underline{B} = -\nabla \times \underline{E} \quad (4.1)$$

Current follows Ohm's law. For currents perpendicular to the background magnetic field, Kirchhoff's formulation is sufficient. Conductivity is much higher along the magnetic field lines¹, so it's appropriate to also include the electron inertial term².

$$0 = \underline{\sigma}_{\perp} \cdot \underline{E}_{\perp} - \underline{J}_{\perp} \quad \frac{1}{\nu} \frac{\partial}{\partial t} J_z = \sigma_0 E_z - J_z \quad (4.2)$$

¹The dipole coordinate system is defined rigorously in Section 5.1; at present, it's sufficient to take \hat{z} parallel to the zeroth-order magnetic field, and \hat{x} and \hat{y} perpendicular to \hat{z} (and to each other).

²Electron inertial effects are not included in the model described in Chapter 5, or in the results in Chapter 7; however, their implementation and impact are explored in Chapter 6.

Derivatives in Equations (4.1) and (4.2) can be evaluated by performing a Fourier transform. They can then be combined, eliminating the magnetic field and current terms.

$$\begin{aligned} 0 &= \underline{\underline{E}}_{\perp} + \frac{v_A^2}{\omega^2} (\underline{k} \times \underline{k} \times \underline{E})_{\perp} + \frac{i}{\epsilon_{\perp}\omega} \underline{\sigma}_{\perp} \cdot \underline{\underline{E}}_{\perp} \\ 0 &= E_z + \frac{c^2}{\omega^2} (\underline{k} \times \underline{k} \times \underline{E})_z + \frac{i\omega_P^2}{\omega(\nu - i\omega)} E_z \end{aligned} \quad (4.3)$$

The speed of light, Alfvén speed (including the displacement current correction), plasma frequency, and parallel conductivity are defined in the usual way:

$$c^2 \equiv \frac{1}{\mu_0\epsilon_0} \quad v_A^2 \equiv \frac{1}{\mu_0\epsilon_{\perp}} \quad \omega_P^2 \equiv \frac{ne^2}{m_e\epsilon_0} \quad \sigma_0 \equiv \frac{ne^2}{m_e\nu} \quad (4.4)$$

Using the vector identity $\underline{k} \times \underline{k} \times \underline{E} = \underline{k} \underline{k} \cdot \underline{E} - k^2 \underline{E}$, Equation (4.3) can be reassembled into a single expression,

$$0 = \left(\underline{\underline{\mathbb{I}}} + \frac{1}{\omega^2} \underline{\underline{V}}^2 \cdot \underline{k} \underline{k} - \frac{k^2}{\omega^2} \underline{\underline{V}}^2 + \frac{i}{\omega} \underline{\underline{\Omega}} \right) \cdot \underline{E} \quad (4.5)$$

Where $\underline{\underline{\mathbb{I}}}$ is the identity tensor and in x - y - z coordinates,

$$\underline{\underline{V}}^2 \equiv \begin{bmatrix} v_A^2 & 0 & 0 \\ 0 & v_A^2 & 0 \\ 0 & 0 & c^2 \end{bmatrix} \quad \text{and} \quad \underline{\underline{\Omega}} \equiv \begin{bmatrix} \frac{\sigma_P}{\epsilon_{\perp}} & \frac{-\sigma_H}{\epsilon_{\perp}} & 0 \\ \frac{\sigma_H}{\epsilon_{\perp}} & \frac{\sigma_P}{\epsilon_{\perp}} & 0 \\ 0 & 0 & \frac{\omega_P^2}{(\nu - i\omega)} \end{bmatrix} \quad (4.6)$$

⁵³³ In Equation (4.5), the expression in parentheses is the dispersion tensor. Nontrivial
⁵³⁴ solutions exist only when its determinant is zero. This gives rise to a seventh-order
⁵³⁵ polynomial in ω , so rather than a direct solution it's necessary to consider limits of
⁵³⁶ specific interest.

⁵³⁷ Without loss of generality, the wave vector \underline{k} may be taken to lie in the x - z plane — that
⁵³⁸ is, with $k_y = 0$. The distinction between the two perpendicular directions is discussed
⁵³⁹ in Section 4.4.

540 **4.1 Guided Propagation**

541 The wave vector of a field line resonance aligns closely to the background magnetic
542 field. By supposing that the two align exactly (that is, taking $k_x = 0$), the parallel and
543 perpendicular components of the dispersion relation are decoupled.

The parallel-polarized component — that is, the solution when $E_x = E_y = 0$ — is quadratic, and thus can be solved directly.

$$0 = \omega^2 + i\nu\omega - \omega_P^2 \quad \text{so} \quad \omega = -\frac{i\nu}{2} \pm \sqrt{\omega_P^2 - \frac{\nu^2}{4}} \quad (4.7)$$

544 It bears noting that the plasma frequency is large — not just compared to Pc4 frequencies,
545 but even compared to the collision frequencies in the ionosphere³.

Expanding Equation (4.7) with respect to large ω_P , the dispersion relation becomes

$$\omega^2 = \omega_P^2 \pm i\nu\omega_P + \dots \quad (4.8)$$

546 Equation (4.8) can hardly be called a wave, as it does not depend on the wave vector
547 \underline{k} . Rather, it is the plasma oscillation⁴: electrons vibrating in response to a charge
548 separation along the background magnetic field.

549 The plasma oscillation is not specifically relevant to the study of field line resonance.
550 The two phenomena are separated by six orders of magnitude in frequency. The topic
551 is revisited in Chapter 6 insomuch as it is inseparable from the electron inertial effects
552 in Ohm's law.

³The collision frequency may match or exceed the plasma frequency for a thin slice at the bottom of the ionosphere, where the density of neutral atoms is large; however, it falls off quickly. Above an altitude of 200 km, conservatively[75], the plasma frequency exceeds the collision frequency by an order of magnitude or more.

⁴The plasma oscillation is also called the Langmuir wave, after Irving Langmuir.

The perpendicular ($E_z = 0$) components of the dispersion relation give an expression quartic in ω .

$$0 = \omega^4 + 2i\frac{\sigma_P}{\epsilon_\perp}\omega^3 - \left(2k_z^2v_A^2 + \frac{\sigma_P^2 + \sigma_H^2}{\epsilon_\perp^2}\right)\omega^2 - 2ik_z^2v_A^2\frac{\sigma_P}{\epsilon_\perp}\omega + k_z^4v_A^4 \quad (4.9)$$

Like the parallel-polarized component above, Equation (4.9) can be solved directly. Noting that \pm and \oplus are independent,

$$\omega = \left(\frac{\pm\sigma_H - i\sigma_P}{2\epsilon_\perp}\right) \oplus \sqrt{k_z^2v_A^2 + \left(\frac{\pm\sigma_H - i\sigma_P}{2\epsilon_\perp}\right)^2} \quad (4.10)$$

Also like the parallel-polarized component, the exact solution is less useful than its Taylor expansion. The Pedersen and Hall conductivities are large near the ionospheric boundary, but fall off quickly; for the vast majority of the field line, the ratios $\frac{\sigma_P}{\epsilon_\perp}$ and $\frac{\sigma_H}{\epsilon_\perp}$ are small compared to field line resonance frequencies. Expanding with respect to small conductivity gives

$$\omega^2 = k_z^2v_A^2 \oplus k_zv_A\frac{\sigma_H \pm i\sigma_P}{\epsilon_\perp} + \dots \quad (4.11)$$

553 This is the shear Alfvén wave, with a shift to its frequency due to the conductivity of
 554 the ionosphere. It travels along the background magnetic field like a bead on a string,
 555 with electric and magnetic field perturbations perpendicular to the magnetic field line
 556 (and to one another).

557 4.2 Compressional Propagation

558 The partner to guided motion is compressional motion; in order for energy to move
 559 across field lines, the wave vector must have a component perpendicular to \hat{z} . If the
 560 wave vector is completely perpendicular to the magnetic field line ($k_z = 0$), the parallel
 561 and perpendicular components of the dispersion relation decouple, as in Section 4.1.

The parallel-polarized ($E_x = E_y = 0$) component of the dispersion relation is

$$0 = \omega^3 + i\nu\omega^2 - (k_x^2 c^2 + \omega_P^2) \omega - ik_x^2 c^2 \nu \quad (4.12)$$

Equation (4.12) can be solved directly, though its solution (as a cubic) is far too long to be useful. Expanding with respect to the large plasma frequency, gives

$$\omega^2 = k^2 c^2 + \omega_P^2 - i\nu\omega_P + \dots \quad (4.13)$$

562 This is the O mode, a compressional wave with an electric field perturbation along
 563 the background magnetic field. Like the plasma oscillation discussed in Section 4.1, its
 564 frequency is very large compared to that of a field line resonance.

The perpendicular-polarized ($E_z = 0$) component of the compressional dispersion relation is also cubic.

$$0 = \omega^3 + 2i\frac{\sigma_P}{\epsilon_\perp}\omega^2 - \left(2k_x^2 v_A^2 + \frac{\sigma_P^2 + \sigma_H^2}{\epsilon_\perp^2}\right) \omega - ik_x^2 v_A^2 \frac{\sigma_P}{\epsilon_\perp} \quad (4.14)$$

A wave moving across magnetic field lines near the ionospheric boundary will encounter large $\frac{\sigma_P}{\epsilon_\perp}$ and $\frac{\sigma_H}{\epsilon_\perp}$, while at moderate to high altitudes those ratios will be small. Solving Equation (4.14) in those two limits respectively gives:

$$\omega^2 = k_x^2 v_A^2 \pm ik_x v_A \frac{\sigma_P}{\epsilon_\perp} + \dots \quad \text{and} \quad \omega^2 = k_x^2 v_A^2 + \left(\frac{\sigma_H \pm i\sigma_P}{\epsilon_\perp}\right)^2 + \dots \quad (4.15)$$

565 In both limits, Equation (4.15) describes a compressional Alfvén wave. The magnetic
 566 field perturbation is along the background magnetic field — indicating compression of
 567 the frozen-in plasma — while the electric field perturbation is perpendicular to both
 568 the magnetic field and the wave vector.

569 **TODO: Double check terminology. Jesse's dissertation disagrees with Bob's notes.**

570 4.3 High Altitude Limit

571 In the limit of large radial distance, it's reasonable to take the collision frequency to
 572 zero; doing so also neglects the Pedersen and Hall conductivities.

Whereas in Sections 4.1 and 4.2 it was the parallel-polarized component of the dispersion relation that factored out from the other two, the high altitude limit decouples the component polarized out of the x - z plane. The y -polarized dispersion ($E_x = E_z = 0$) is simply:

$$\omega^2 = k^2 v_A^2 \quad (4.16)$$

573 Equation (4.16) describes an Alfvén wave with an arbitrary angle of propagation. De-
 574 pending on the angle between the wave vector and the background magnetic field, it
 575 could be guided, compressional, or somewhere in between. Regardless of propagation
 576 angle, the electric field perturbation is perpendicular to both the direction of propaga-
 577 tion and the magnetic field perturbation.

The other two components (from $E_y = 0$) of the high altitude dispersion tensor give an expression quadratic in ω^2 :

$$0 = \omega^4 - (k_x^2 c^2 + k_z^2 v_A^2 + \omega_P^2) \omega^2 + k_z^2 v_A^2 \omega_P^2 \quad (4.17)$$

Which can be solved for

$$\omega^2 = \frac{1}{2} (k_x^2 c^2 + k_z^2 v_A^2 + \omega_P^2) \pm \sqrt{\frac{1}{4} (k_x^2 c^2 + k_z^2 v_A^2 + \omega_P^2)^2 - k_z^2 v_A^2 \omega_P^2} \quad (4.18)$$

Noting again that ω_P is very large, the two roots can be expanded to

$$\omega^2 = k_z^2 v_A^2 \left(1 + \frac{k_x^2 c^2 + k_z^2 v_A^2}{\omega_P^2} \right) + \dots \quad \text{and} \quad \omega^2 = k_x^2 c^2 + k_z^2 v_A^2 + \omega_P^2 + \dots \quad (4.19)$$

578 The first is a shear Alfvén wave, as in Equation (4.11). The second oscillates faster than
579 the plasma frequency; like the plasma oscillation in Equation (4.8) and the O mode in
580 Equation (4.13), it's far outside the Pc4 frequency range.

581 4.4 Implications to the Present Work

582 The present section's findings carry three significant implications for the present work.
583 First — with the exception of the plasma oscillation and similar modes, which are
584 revisited in Chapter 6 — waves propagate at the Alfvén speed. This, in combination
585 with the grid configuration, will constrain the time step that can be used to model them
586 numerically. The time step must be sufficiently small that information traveling at the
587 Alfvén speed cannot “skip over” entire grid cells⁵.

Second, the results of the present section allow an estimate of the magnitude of parallel electric field that might be expected from a field line resonance compared to its perpendicular electric field. Between the full dispersion tensor form in Equation (4.5) and the Alfvén wave described by Equation (4.19),

$$\left| \frac{E_z}{E_x} \right| = \frac{k_x k_z c^2}{\omega^2 - k_x^2 c^2 - \omega_P^2} \sim \frac{k^2 c^2}{\omega_P^2} \quad (4.20)$$

588 In essence, the relative magnitudes of the parallel and perpendicular electric fields should
589 be in proportion to the square of the relative magnitudes of the electron inertial length
590 (1 km to 100 km) and the wavelength ($\sim 10^5$ km). That is, parallel electric fields should
591 be smaller than the perpendicular electric fields by six or more orders of magnitude.

592 Finally, the dispersion relations shown above indicate how the behavior of a field line
593 resonance should behave as the azimuthal modenumber becomes large.

594 Whereas the shear Alfvén wave's dispersion relation depends only on the parallel component
595 of the wave vector, the compressional Alfvén wave depends on its magnitude:
596 $\omega^2 = k^2 v_A^2$. If the frequency is smaller than $k v_A$, the wave will become evanescent. The

⁵As is the convention, the time step is scaled down from the smallest Alfvén zone crossing time by a Courant factor, typically 0.1, meaning that it takes at least ten time steps to cross a grid cell.

597 wave vector's magnitude can be no smaller than its smallest component, however, and
 598 the azimuthal component scales with the azimuthal modenumber: $k_y \sim \frac{m}{2\pi r}$.

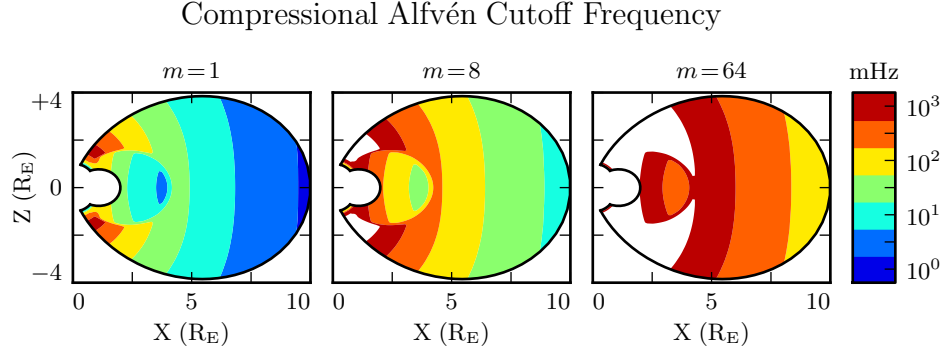


Figure 4.1: Taking $k_y \sim \frac{m}{2\pi r}$ as a lower bound for the magnitude of the wave vector, the above figure demonstrates the lowest frequency at which compressional Alfvén waves may propagate as a function of position and m . Regions shown in white are off the color scale — they have a lower bound on the order of 10^4 mHz or more. The above Alfvén frequency profile is from Kelley[49], for quiet dayside conditions, as discussed in Section 5.2.

599 This imposes a frequency cutoff on compressional Alfvén waves which scales with the
 600 azimuthal modenumber, as shown in Figure 4.1. At small values of m , most of the mag-
 601 netosphere is conducive to compressional Alfvén waves in the Pc4 frequency range. As
 602 m increases, and the wave vector with it, the inner magnetosphere becomes increasingly
 603 inaccessible to them.

604 **Chapter 5**

605 **“Tuna Half” Dimensional Model**

606 The present section describes the implementation of Tuna, a new two and a half dimensional
607 Alfvén wave code based largely on work by Lysak[60, 63].

608 The half-integer dimensionality refers to the fact that Tuna’s spatial grid resolves a
609 two-dimensional slice of the magnetosphere, but that electric and magnetic fields —
610 as well as their curls — are three-dimensional vectors. This apparent contradiction is
611 reconciled by the use of a fixed azimuthal modenumber, m . Electric and magnetic fields
612 are taken to be complex-valued, varying azimuthally per $\exp(im\phi)$; derivatives with
613 respect to ϕ are then replaced by a factor of im .

614 Unlike a fully three-dimensional code, Tuna cannot resolve the evolution of wave structures
615 in the azimuthal direction. Furthermore, the model does not allow coupling between
616 the dayside and nightside magnetospheres. What Tuna does offer is efficiency.
617 The model’s economical geometry allows it to include a realistic Earthward boundary:
618 grid spacing on the order of 10 km, a height-resolved ionospheric conductivity tensor,
619 and even the computation of magnetic field signatures at the ground. Such features are
620 computationally infeasible for a large global code.

621 Tuna was developed with field line resonance in mind. As discussed in Chapter 3,
622 such waves are azimuthally localized, minimizing the importance of Tuna’s missing half
623 dimension. Moreover, because field line resonances are known to be affected by both

624 the ionosphere and the plasmasphere, a faithful treatment of the inner magnetosphere
625 is a crucial part of studying them numerically.

626 Perhaps the most exciting feature of Tuna is its novel driving mechanism: ring current
627 perturbation. Codes similar to Tuna have traditionally been driven using compressional
628 pulses at the outer boundary[60, 63, 102, 103]. This has precluded the investigation of
629 waves with large azimuthal modenumber — such as giant pulsations — which are guided,
630 and thus must be driven from within the magnetosphere.

631 TODO: The dipole geometry isn't super new, but it's not widely used. The height-
632 resolved ionosphere is new and exciting! Ground signatures are new and exciting!

633 TODO: The support software — the driver and the plotter — are also significant. Do
634 they get mentioned here? Does the Git repository where the code can be accessed get
635 mentioned here?

636 5.1 Coordinate System

Field line resonance has traditionally been modeled by straightening the field lines into a rectangular configuration[22, 66], by unrolling the azimuthal coordinate into a cylindrical coordinate system[80], or through the use of dipole coordinates[79]¹:

$$x \equiv -\frac{\sin^2 \theta}{r} \quad y \equiv \phi \quad z \equiv \frac{\cos \theta}{r^2} \quad (5.1)$$

637 Where r , θ , and ϕ take on their usual spherical meanings of radial distance, colatitude,
638 and azimuthal angle respectively.

639 The dipole coordinate x is constant over each equipotential shell², y is azimuthal angle,
640 and z indexes each field line from south to north. The unit vectors \hat{x} , \hat{y} , and \hat{z} point

¹The dipole coordinates x , y and z are perhaps more commonly named μ , ϕ , and ν respectively; however, in the present work, μ and ν take other meanings.

²In fact, x is inversely proportional to the McIlwain parameter L .

641 in the crosswise³ (radially outward at the equator), azimuthal (eastward), and parallel
 642 (northward at the equator) directions respectively.

Notably, the dipole coordinates in Equation (5.1) are normal to one another. While mathematically convenient, they do not readily accommodate a fixed-altitude boundary at the ionosphere, nor do they allow the dipole magnetic field to intersect the boundary at an oblique angle, as Earth's field does. As a solution, a nonorthogonal set of dipole coordinates was developed numerically by Proehl[78], then formalized analytically by Lysak[60] in terms of their contravariant components:

$$u^1 = -\frac{R_I}{r} \sin^2 \theta \quad u^2 = \phi \quad u^3 = \frac{R_I^2}{r^2} \frac{\cos \theta}{\cos \theta_0} \quad (5.2)$$

643 Above, R_I is the position of the ionosphere relative to Earth's center; it's typically taken
 644 to be $1 R_E + 100 \text{ km}$.

645 Like the dipole coordinates x , y , and z , Lysak's coordinates u^1 , u^2 , and u^3 correspond to
 646 L -shell, azimuthal angle, and position along a field line respectively. However, compared
 647 to z , u^3 has been renormalized using the invariant colatitude⁴ θ_0 . As a result, u^3 takes
 648 the value $+1$ at the northern ionospheric boundary and -1 at the southern ionospheric
 649 boundary for all field lines.

Because Lysak's coordinate system is not orthogonal⁵, it's necessary to consider covariant and contravariant basis vectors separately.

$$\hat{e}_i \equiv \frac{\partial}{\partial u^i} \underline{x} \quad \hat{e}^i \equiv \frac{\partial}{\partial \underline{x}} u^i \quad (5.3)$$

Covariant basis vectors \hat{e}_i are normal to the curve defined by constant u^i , while contravariant basis vectors \hat{e}^i are tangent to the coordinate curve (equivalently, \hat{e}^i is normal

³In the context of in situ measurements taken near the equatorial plane, \hat{x} is referred to as the radial direction; however, the present work extends the dipole grid to low altitudes, where \hat{x} can be more horizontal than vertical. The term "crosswise" is meant to indicate that \hat{x} is defined by the cross product of \hat{y} and \hat{z} .

⁴The invariant colatitude is the colatitude θ at which a field line intersects the ionosphere. It is related to the McIlwain parameter by $\cos \theta_0 \equiv \sqrt{1 - \frac{R_I}{L}}$.

⁵Curves of constant u^1 and curves of constant u^3 can intersect at non-right angles.

to the plane defined by constant u^j for all $j \neq i$). These vectors are reciprocal⁶ to one another, and can be combined to give components of the metric tensor $\underline{\underline{g}}$ [20].

$$\hat{e}^i \cdot \hat{e}_j = \delta_j^i \quad g_{ij} \equiv \hat{e}_i \cdot \hat{e}_j \quad g^{ij} \equiv \hat{e}^i \cdot \hat{e}^j \quad (5.4)$$

The metric tensor allows rotation between covariant and contravariant representations of vectors.

$$A_i = g_{ij} A^j \quad \text{and} \quad A^i = g^{ij} A_j \quad \text{where} \quad A_i \equiv \underline{A} \cdot \hat{e}_i \quad \text{and} \quad A^i \equiv \underline{A} \cdot \hat{e}^i \quad (5.5)$$

In addition, the determinant of the metric tensor is used to define cross products and curls⁷.

$$(\underline{A} \times \underline{B})^i = \frac{\varepsilon^{ijk}}{\sqrt{g}} A_j B_k \quad \text{and} \quad (\nabla \times \underline{A})^i = \frac{\varepsilon^{ijk}}{\sqrt{g}} \frac{\partial}{\partial u^j} A_k \quad \text{where} \quad g \equiv \det \underline{\underline{g}} \quad (5.6)$$

Explicit forms of the basis vectors and metric tensor can be found in the appendix of Lysak's 2004 paper[60]. At present, it's sufficient to note the mapping between Lysak's basis vectors and the usual dipole unit vectors.

$$\hat{x} = \frac{1}{\sqrt{g^{11}}} \hat{e}^1 \quad \hat{y} = \frac{1}{\sqrt{g^{22}}} \hat{e}^2 \quad \hat{z} = \frac{1}{\sqrt{g^{33}}} \hat{e}^3 \quad (5.7)$$

650 TODO: Do these need to be written out? Referring people to the code, which will be
651 in a public Git repository, is also a possibility.

The basis vectors can also be mapped to the spherical unit vectors, though Equation (5.8) is valid only at the ionospheric boundary.

$$\hat{\theta} = \frac{1}{\sqrt{g_{11}}} \hat{e}_1 \quad \hat{\phi} = \frac{1}{\sqrt{g_{22}}} \hat{e}_2 \quad \hat{r} = \frac{1}{\sqrt{g_{33}}} \hat{e}_3 \quad (5.8)$$

⁶The symbol δ_j^i is the Kronecker delta; the present work also makes use of the Levi-Civita symbol ε^{ijk} and Einstein's convention of implied summation over repeated indeces[24].

⁷The square root of the determinant of the metric tensor is called the Jacobian. It's sometimes denoted using the letter J , which is reserved for current in the present work.

652 The coordinates converge at the equatorial ionosphere, so an inner boundary is necessary
653 to maintain finite grid spacing. It's typically placed at $L = 2$. The outer boundary is
654 at $L = 10$. The dipole approximation of Earth's magnetic field is tenuous at the outer
655 boundary (particularly on the dayside); however, in practice, wave activity is localized
656 inside $L \sim 7$. The grid is spaced uniformly in u^1 , which gives finer resolution close to
657 Earth and coarser resolution at large distances.

658 Spacing in u^3 is set by placing grid points along the outermost field line. The points are
659 closest together at the ionosphere, and grow towards the equator. The spacing increases
660 in a geometric fashion, typically by 3%.

661 Typically, Tuna uses a grid 150 points in u^1 by 350 points in u^3 . The result is a resolution
662 on the order of 10 km at the ionosphere, which increases to the order of 10^3 km at the
663 midpoint of the outermost field line.

664 There are no grid points in u^2 due to the two-and-a-half-dimensional nature of the
665 model. Fields are assumed to vary as $\exp(imu^2)$ — equally, $\exp(im\phi)$ — so derivatives
666 with respect to u^2 are equivalent to a factor of im . In effect, the real component of
667 each field is azimuthally in phase with the (purely real) driving, while imaginary values
668 represent behavior that is azimuthally offset.

669 The simulation's time step is set based on the grid spacing. As is the convention, δt is
670 set to match the smallest Alfvén zone crossing time, scaled down by a Courant factor
671 (typically 0.1). It bears noting that the smallest crossing time need not correspond to
672 the smallest zone; the Alfvén speed peaks several thousand kilometers above Earth's
673 surface, in the so-called Ionospheric Alfvén Resonator[63]. A typical time step is on the
674 order of 10^{-5} s.

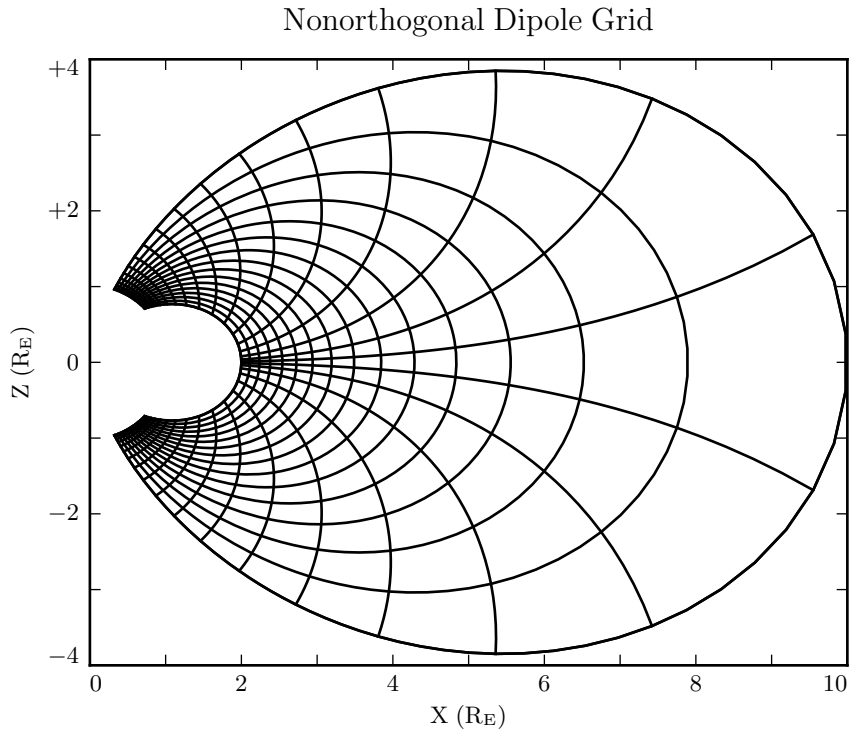


Figure 5.1: The model’s nonorthogonal dipole grid. Every fifth point is shown in each direction. The high concentration of grid points near Earth’s equator is a consequence of the coordinate system, which converges at the equatorial ionosphere. Earth (not shown) is centered at the origin with unit radius.

675 **5.2 Physical Parameter Profiles**

Tuna models Earth’s magnetic field to be an ideal dipole, so the zeroth-order field strength is written in the usual form:

$$\underline{B}_0 = 3.1 \times 10^4 \text{ nT} \left(\frac{R_E}{r} \right)^3 \left(2 \cos \theta \hat{r} - \sin \theta \hat{\theta} \right) \quad (5.9)$$

Number density is taken to be the sum of an inverse-radial-dependent auroral profile and a plasmaspheric profile dependent on the L -shell[63]:

$$n = n_{AZ} \frac{r_{AZ}}{r} + n_{PS} \exp\left(\frac{-L}{L_{PS}}\right) \left(\frac{1}{2} - \frac{1}{2} \tanh \frac{L - L_{PP}}{\delta L_{PP}} \right) \quad (5.10)$$

676 Where typical values are shown in Table 5.1.

Table 5.1: Typical Parameters for the Tuna Density Profile

Variable	Value	Description
L_{PS}	1.1	Scale L of the plasmasphere.
L_{PP}	4.0	Location of the plasmapause.
δL_{PP}	0.1	Thickness of the plasmapause.
n_{AZ}	$10 / \text{cm}^3$	Number density at the base of the auroral zone.
n_{PS}	$10^4 / \text{cm}^3$	Number density at the base of the plasmasphere.
r_{AZ}	1 R_E	Scale height of the auroral density distribution.

The perpendicular component of the electric tensor, ϵ_{\perp} , is computed based on Kelley's[49] tabulated low-density values, ϵ_K , which are adjusted to take into account the effects of high density in the plasmapause.

$$\epsilon_{\perp} = \epsilon_K + \frac{Mn}{B_0^2} \quad (5.11)$$

677 Where M is the mean molecular mass, which is large ($\sim 28 \text{ u}$) at 100 km altitude, then
678 drops quickly (down to 1 u by $\sim 1000 \text{ km}$)[63].

679 The Alfvén speed profile is computed from the perpendicular electric constant in the
680 usual way, $v_A^2 \equiv \frac{1}{\mu_0 \epsilon_{\perp}}$. This form takes into account the effect of the displacement
681 current, which becomes important in regions where the Alfvén speed approaches the
682 speed of light.

683 While the density profile is held constant for all runs discussed in the present work,
684 the Alfvén speed profile is not. Four different profiles are used for the low-density

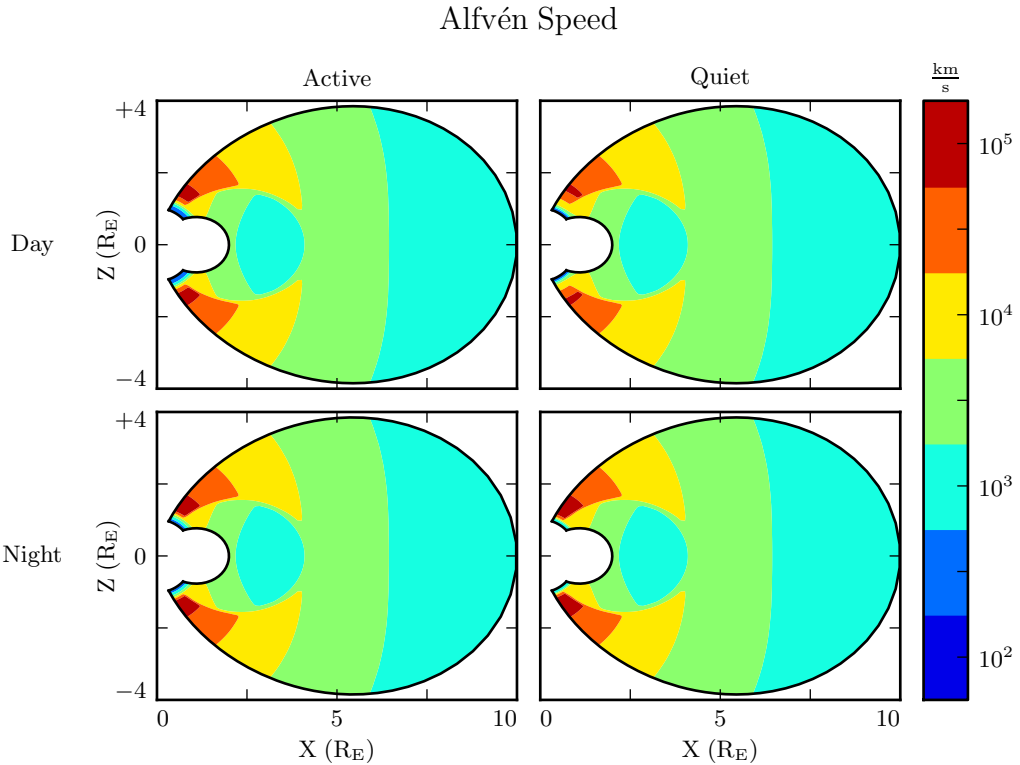


Figure 5.2: Alfvén speed profiles are based on low-density values tabulated by Kelley[49]. They are adjusted to take into account the density of the plasmapause and mass loading near the Earthward boundary.

685 perpendicular electric constant ϵ_K , corresponding to the differing ionospheric conditions
 686 between the dayside and the nightside, and between the high and low points in the
 687 solar cycle. These differences are visible in Figure 5.2, particularly in the size of the
 688 ionospheric Alfvén resonator (the peak in Alfvén speed in the high-latitude ionosphere).

689 **TODO:** Runs are only carried out for day and night... is it even worth showing the
 690 flank profile?

691 Ionospheric conductivity profiles are also based on values tabulated by Kelley, adjusted
 692 by Lysak[63] to take into account the abundance of heavy ions near the Earthward
 693 boundary. Pedersen, Hall, and parallel conductivities are each resolved by altitude, as
 694 shown in Figure 5.3.

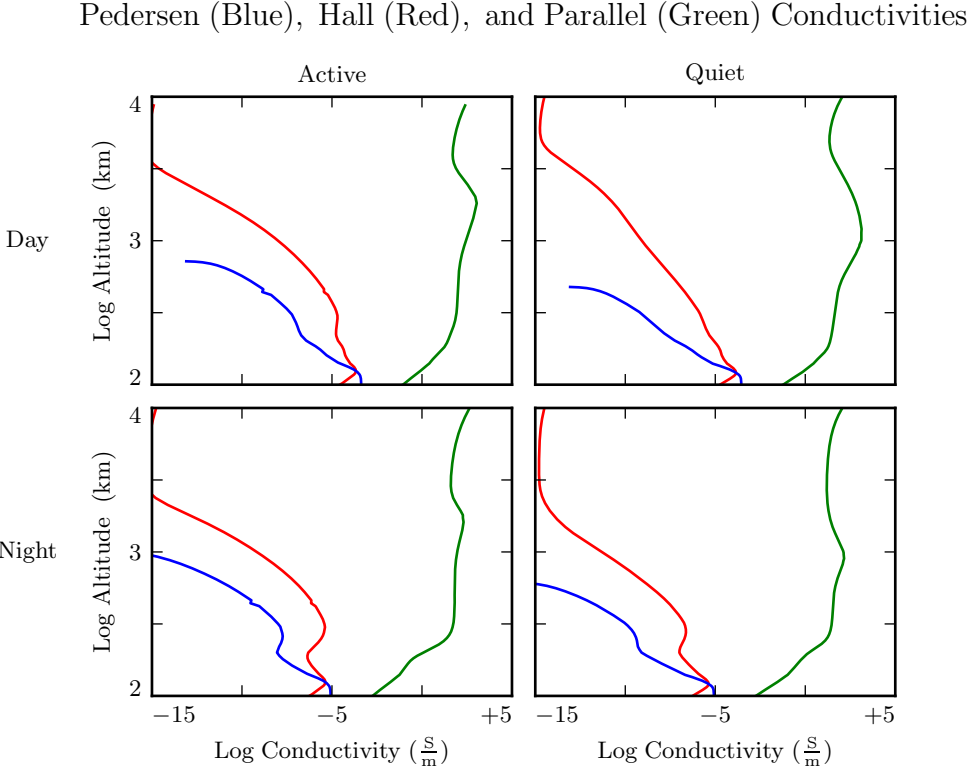


Figure 5.3: Ionospheric conductivity profiles are adapted by Lysak[63] from Kelley's tabulated values[49]. These profiles allow Tuna to simulate magnetosphere-ionosphere coupling under a variety of conditions.

695 Tuna's physical parameter profiles are static over the course of each run. Even so-called
 696 ultra low frequency waves like Pc4 pulsations are fast compared to convective timescales
 697 in the magnetosphere.

698 5.3 Driving

699 Models similar to Tuna have traditionally been driven using compression at the outer
 700 boundary[60, 63, 102, 103]. Such driving acts as a proxy for solar wind compression,
 701 Kelvin-Helmholtz effects at the magnetopause, and so on. However, because of the

702 constraints imposed by the dispersion relation for Alfvén waves⁸, simulations driven from
703 the outer boundary are constrained to the consideration of waves with low azimuthal
704 modenumber (equivalently, large azimuthal wavelength).

705 This issue is demonstrated in Figure 5.4. At low modenumber, energy delivered at
706 the outer boundary propagates across field lines in order to stimulate resonances in
707 the inner magnetosphere. However, as modenumber increases, Alfvén waves become
708 increasingly guided, and the inner magnetosphere is unaffected by perturbations at the
709 outer boundary.

710 In order to simulate high-modenumber Alfvén waves in the inner magnetosphere — such
711 as giant pulsations — a new driving mechanism is necessary. Perturbation of the ring
712 current is a natural choice, as Alfvén waves in the Pc4 range are known to interact with
713 ring current particles through drift and drift-bounce resonances. The ring current is a
714 dynamic region, particularly during and after geomagnetic storms; it's easy to imagine
715 the formation of localized inhomogeneities.

716 In order to estimate an appropriate magnitude for perturbations of the ring current,
717 the Sym-H storm index is used. The index is measured once per minute, and so cannot
718 directly detect ring current modulations in the Pc4 frequency range. Instead, the index
719 is transformed into the frequency domain, allowing a fit of its pink noise⁹.

720 **TODO:** Sym-H is basically the same as Dst[101].

721 As shown in Figure 5.5, a Fourier transform of the Sym-H index (taken here from the
722 June 2013 storm) suggests that magnetic field perturbations at Earth's surface due to
723 ring current activity in the Pc4 frequency range could be up to the order of 10^{-2} nT.
724 Supposing that the ring current is centered around $5 R_E$ geocentric, that corresponds to
725 a current on the order of 0.1 MA. Tuna's driving is spread using a Gaussian profile in
726 u^1 (typically centered at $L = 5$) and u^3 (typically centered just off the equator), with a
727 characteristic area of $1 R_E^2$; this gives a current density on the order of $10^{-4} \mu\text{A}/\text{m}^2$.

⁸See Section 4.4.

⁹Pink noise, also called $\frac{1}{f}$ noise, refers to the power law decay present in the Fourier transforms of all manner of physical signals.

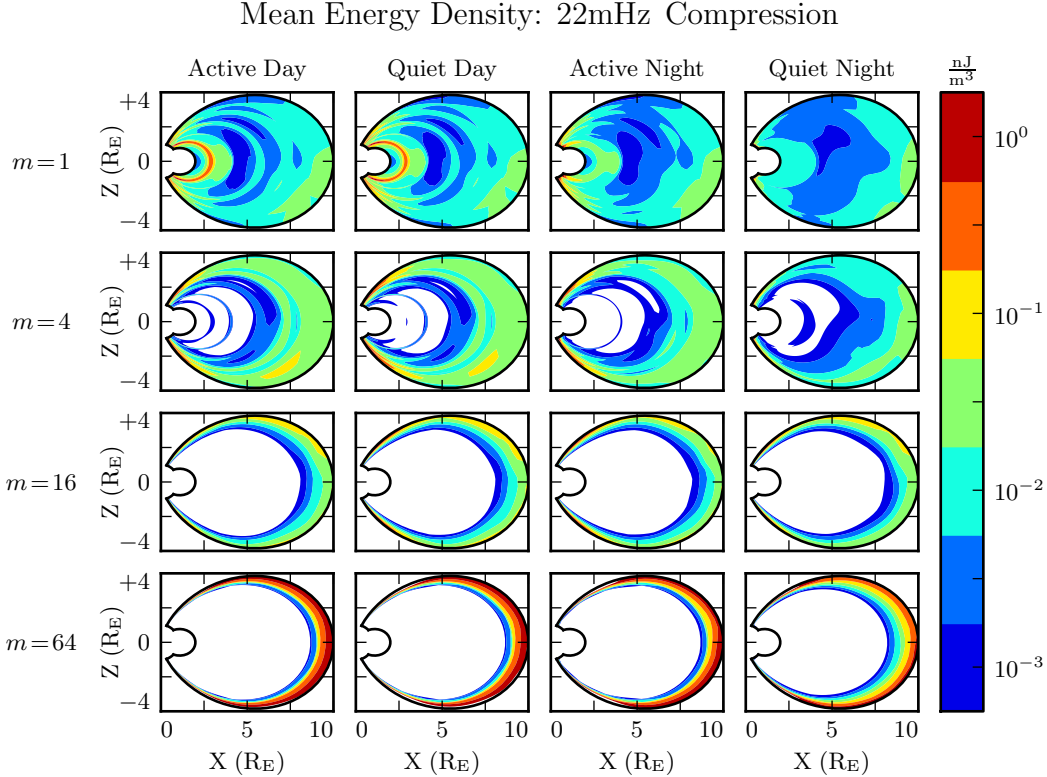


Figure 5.4: Each cell presents the mean energy density over the course of a 300s run, as a function of position, due to compressional driving at the outer boundary. Azimuthal modenumber varies by row, and ionospheric conditions vary by column. For runs with small azimuthal modenumber, it's clear that energy is able to propagate across field lines and stimulate wave activity in the inner magnetosphere. When the modenumber is large, energy is unable to penetrate to the inner magnetosphere. Notably, the large values on the bottom row should be taken with a grain of salt; it's not clear that the model's results are reliable when waves are continuously forced against the boundary.

- 728 TODO: Admittedly, estimating the strength of localized perturbations using Sym-H —
 729 an index averaged over the entire globe — is a bit of a kludge.
- 730 In situ observations of Pc4 pulsations and giant pulsations have shown waves with
 731 modenumbers across the range $1 \lesssim m \lesssim 100$ [17, 18, 92]. Simulations are carried out
 732 across that range, corresponding to ring current perturbations with azimuthal extent as
 733 small as $0.5 R_E$.

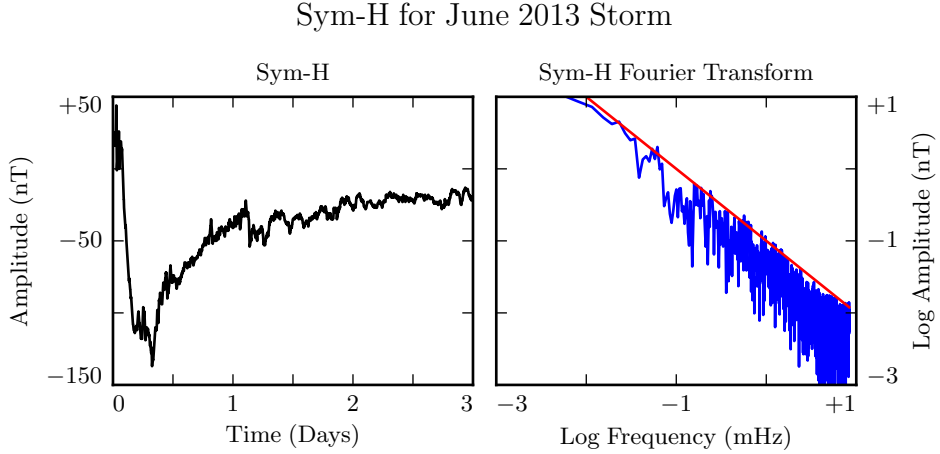


Figure 5.5: The Sym-H storm index[73] measures magnetic perturbations on Earth’s surface due to ring current activity. The amplitude of oscillations in the Pc4 range is estimated by fitting the pink noise in its Fourier transform.

734 TODO: Driving is delivered in the azimuthal component of the current only.

735 TODO: Driving is sinusoidal.

736 TODO: In case it’s not clear: Chapter 7 discusses ONLY simulations using ring current driving. The only compressional driving we look at is Figure 5.4.

738 5.4 Maxwell’s Equations

739 Tuna simulates the evolution of electromagnetic waves in accordance with Ampère’s
740 law and Faraday’s law. Computation is carried out on a Yee grid[107]: electric fields
741 and magnetic fields are offset by half a time step, and each field component is defined
742 on either odd or even grid points in each dimension to ensure that curls are computed
743 using centered differences.

The Ohmic current in Ampère’s law is replaced with $\underline{\sigma} \cdot \underline{E}$ per Kirchhoff’s formulation of Ohm’s law. Then, taking \underline{J} to represent the driving current discussed in Section 5.3,

Maxwell's equations can be written

$$\frac{\partial}{\partial t} \underline{B} = -\nabla \times \underline{E} \quad \underline{\epsilon} \cdot \frac{\partial}{\partial t} \underline{E} = \frac{1}{\mu_0} \nabla \times \underline{B} - \underline{J} - \underline{\sigma} \cdot \underline{E} \quad (5.12)$$

It is convenient to introduce shorthand for the curl of each field: $\underline{C} \equiv \nabla \times \underline{E}$ and $\underline{F} \equiv \nabla \times \underline{B} - \mu_0 \underline{J}$. Or, recalling Equation (5.6),

$$C^i = \frac{\varepsilon^{ijk}}{\sqrt{g}} \frac{\partial}{\partial u^j} E_k \quad F^i = \frac{\varepsilon^{ijk}}{\sqrt{g}} \frac{\partial}{\partial u^j} B_k - J^i \quad (5.13)$$

In these terms, Faraday's law can simply be written:

$$\frac{\partial}{\partial t} B^i = -C^i \quad (5.14)$$

Writing each component out explicitly, and using the metric tensor (per Equation (5.5)) to eliminate contravariant magnetic field components¹⁰, Equation (5.14) becomes:

$$\begin{aligned} B_1 &\leftarrow B_1 - g_{11} \delta t C^1 - g_{13} \delta t C^3 \\ B_2 &\leftarrow B_2 - g_{22} \delta t C^2 \\ B_3 &\leftarrow B_3 - g_{31} \delta t C^1 - g_{33} \delta t C^3 \end{aligned} \quad (5.15)$$

⁷⁴⁴ Note that the \leftarrow operator is used in Equation (5.15) to indicate assignment, rather than equality. Terms on the left are new, while those on the right are old.

Unlike Faraday's law, Ampère's law cannot be trivially solved. Not only does the derivative of \underline{E} depend on its own future value, but the crosswise and azimuthal components of the equation are coupled by the Hall terms in the conductivity tensor. Fortunately,

¹⁰Fields are stored only in terms of their covariant components, and curls in terms of their contravariant components. This reduces Tuna's memory footprint (since each field need not be stored twice) as well as its computational cost (since time need not be spent rotating between bases). As a result, Tuna's solutions to Maxwell's equations are linear expressions whose coefficients are a mishmash of physical constants and geometric factors. To save time, each coefficient is computed once and stored, rather than being multiplied out from scratch with each time step.

the electric tensor can be inverted, allowing a solution by integrating factors:

$$\underline{\epsilon} \cdot \frac{\partial}{\partial t} \underline{E} = \frac{1}{\mu_0} \underline{F} - \underline{\sigma} \cdot \underline{E} \quad \text{becomes} \quad \left(\underline{\Omega} + \underline{\mathbb{I}} \frac{\partial}{\partial t} \right) \cdot \underline{E} = \underline{V}^2 \cdot \underline{F} \quad (5.16)$$

Where $\underline{\mathbb{I}}$ is the identity tensor and in x - y - z coordinates¹¹,

$$\underline{V}^2 \equiv \frac{1}{\mu_0} \underline{\epsilon}^{-1} = \begin{bmatrix} v_A^2 & 0 & 0 \\ 0 & v_A^2 & 0 \\ 0 & 0 & c^2 \end{bmatrix} \quad \text{and} \quad \underline{\Omega} \equiv \underline{\epsilon}^{-1} \cdot \underline{\sigma} = \begin{bmatrix} \frac{\sigma_P}{\epsilon_{\perp}} & \frac{-\sigma_H}{\epsilon_{\perp}} & 0 \\ \frac{\sigma_H}{\epsilon_{\perp}} & \frac{\sigma_P}{\epsilon_{\perp}} & 0 \\ 0 & 0 & \frac{\sigma_0}{\epsilon_0} \end{bmatrix} \quad (5.17)$$

Multiplying through by $\exp(\underline{\Omega} t)$ and applying the product rule, Equation (5.16) becomes¹²

$$\frac{\partial}{\partial t} \left(\exp(\underline{\Omega} t) \cdot \underline{E} \right) = \exp(\underline{\Omega} t) \cdot \underline{V}^2 \cdot \underline{F} \quad (5.18)$$

Equation (5.18) can then be integrated over a small time step δt and expressed in terms of the assignment operator introduced in Equation (5.15).

$$\underline{E} \leftarrow \exp(-\underline{\Omega} \delta t) \cdot \underline{E} + \delta t \exp(-\underline{\Omega} \frac{\delta t}{2}) \cdot \underline{V}^2 \cdot \underline{F} \quad (5.19)$$

The tensor exponential can be evaluated by splitting $\underline{\Omega}$ into the sum of its diagonal and Hall components¹³. The Hall exponential condenses into sines and cosines, giving a rotation around the magnetic field line:

$$\underline{E} \leftarrow \exp(-\underline{\Omega}' \delta t) \cdot \underline{R}_z \left(\frac{-\sigma_H \delta t}{\epsilon_{\perp}} \right) \cdot \underline{E} + \delta t \underline{V}^2 \cdot \exp(-\underline{\Omega}' \frac{\delta t}{2}) \cdot \underline{R}_z \left(\frac{-\sigma_H \delta t}{2\epsilon_{\perp}} \right) \cdot \underline{F} \quad (5.20)$$

¹¹Note the parallel component of the present definition of $\underline{\Omega}$ differs slightly from that used in Chapter 4, due to the present neglect of inertial effects; see Chapter 6.

¹²Tensor exponentiation is analogous to scalar exponentiation[38]: $\exp(\underline{T}) \equiv \sum_n \frac{1}{n!} \underline{T}^n$.

¹³For tensors, $\exp(\underline{S} + \underline{T}) = \exp(\underline{S}) \exp(\underline{T})$ as long as $\underline{S} \cdot \underline{T} = \underline{T} \cdot \underline{S}$.

Where

$$\underline{\underline{R}}_z(\theta) = \begin{bmatrix} \cos \theta & -\sin \theta & 0 \\ \sin \theta & \cos \theta & 0 \\ 0 & 0 & 1 \end{bmatrix} \quad \text{and} \quad \underline{\underline{\Omega}}' \equiv \begin{bmatrix} \frac{\sigma_P}{\epsilon_{\perp}} & 0 & 0 \\ 0 & \frac{\sigma_P}{\epsilon_{\perp}} & 0 \\ 0 & 0 & \frac{\sigma_0}{\epsilon_0} \end{bmatrix} \quad (5.21)$$

The parallel component of term of Equation (5.20) is simply

$$E_z \leftarrow E_z \exp\left(\frac{-\sigma_0 \delta t}{\epsilon_0}\right) + c^2 \delta t F_z \exp\left(\frac{-\sigma_0 \delta t}{2\epsilon_0}\right) \quad (5.22)$$

Or, using Equation (5.7) to map to the covariant basis,

$$E_3 \leftarrow E_3 \exp\left(\frac{-\sigma_0 \delta t}{\epsilon_0}\right) + c^2 \delta t (g_{31} F^1 + g_{33} F^3) \exp\left(\frac{-\sigma_0 \delta t}{2\epsilon_0}\right) \quad (5.23)$$

⁷⁴⁶ Tuna's conductivity profile gives a minimum value of $\frac{\sigma_0 \delta t}{\epsilon_0}$ on the order of 10^3 , making
⁷⁴⁷ $\exp\left(\frac{-\sigma_0 \delta t}{\epsilon_0}\right)$ far too small to be stored in a double precision variable¹⁴. That is, this
⁷⁴⁸ model takes E_3 (and, proportionally, E_z) to be uniformly zero. This issue is revisited
⁷⁴⁹ in Chapter 6.

The perpendicular components of Equation (5.20) give the expressions:

$$\begin{aligned} E_1 + \frac{g^{13}}{g^{11}} E_3 &\leftarrow E_1 \cos\left(\frac{-\sigma_H \delta t}{\epsilon_{\perp}}\right) \exp\left(\frac{-\sigma_P \delta t}{\epsilon_{\perp}}\right) \\ &\quad + E_2 \sin\left(\frac{-\sigma_H \delta t}{\epsilon_{\perp}}\right) \exp\left(\frac{-\sigma_P \delta t}{\epsilon_{\perp}}\right) \sqrt{\frac{g^{22}}{g^{11}}} \\ &\quad + E_3 \cos\left(\frac{-\sigma_H \delta t}{\epsilon_{\perp}}\right) \exp\left(\frac{-\sigma_P \delta t}{\epsilon_{\perp}}\right) \frac{g^{13}}{g^{11}} \\ &\quad + F^1 \cos\left(\frac{-\sigma_H \delta t}{2\epsilon_{\perp}}\right) \exp\left(\frac{-\sigma_P \delta t}{2\epsilon_{\perp}}\right) \frac{v_A^2 \delta t}{g^{11}} \\ &\quad + F^2 \sin\left(\frac{-\sigma_H \delta t}{2\epsilon_{\perp}}\right) \exp\left(\frac{-\sigma_P \delta t}{2\epsilon_{\perp}}\right) \frac{v_A^2 \delta t}{\sqrt{g^{11} g^{22}}} \end{aligned} \quad (5.24)$$

¹⁴Not coincidentally, $\frac{\sigma_0}{\epsilon_0}$ can also be written $\frac{\omega_P^2}{\nu}$. At the ionosphere, the collision frequency ν is fast compared to field line resonance timescales, but it's still slow compared to the plasma frequency.

and

$$\begin{aligned}
E_2 \leftarrow & -E_1 \sin\left(\frac{-\sigma_H \delta t}{\epsilon_{\perp}}\right) \exp\left(\frac{-\sigma_P \delta t}{\epsilon_{\perp}}\right) \sqrt{\frac{g^{11}}{g^{22}}} \\
& + E_2 \cos\left(\frac{-\sigma_H \delta t}{\epsilon_{\perp}}\right) \exp\left(\frac{-\sigma_P \delta t}{\epsilon_{\perp}}\right) \\
& - E_3 \sin\left(\frac{-\sigma_H \delta t}{\epsilon_{\perp}}\right) \exp\left(\frac{-\sigma_P \delta t}{\epsilon_{\perp}}\right) \frac{g^{13}}{\sqrt{g^{11} g^{22}}} \\
& - F^1 \sin\left(\frac{-\sigma_H \delta t}{2\epsilon_{\perp}}\right) \exp\left(\frac{-\sigma_P \delta t}{2\epsilon_{\perp}}\right) \frac{v_A^2 \delta t}{\sqrt{g^{11} g^{22}}} \\
& + F^2 \cos\left(\frac{-\sigma_H \delta t}{2\epsilon_{\perp}}\right) \exp\left(\frac{-\sigma_P \delta t}{2\epsilon_{\perp}}\right) \frac{v_A^2 \delta t}{g^{22}}
\end{aligned} \tag{5.25}$$

750 The E_3 terms in Equations (5.24) and (5.25) can be ignored at present. They are
751 revisited in Chapter 6.

752 It bears recalling that the driving current is defined as part of \underline{F} , per Equation (5.13).
753 When the driving current is purely azimuthal ($J^1 = J^3 = 0$), the driving is in principle
754 applied to both the poloidal and the toroidal electric fields through F^2 . However,
755 in practice, the driving applied to the toroidal electric field is vanishingly small. The
756 driving current J^2 is localized around $5 R_E$ geocentric, and $\exp\left(\frac{-\sigma_P \delta t}{2\epsilon_{\perp}}\right)$ drops off quickly
757 with altitude.

758 5.5 Boundary Conditions

759 Dirichlet and Neumann boundary conditions are applied to the electric field components
760 and magnetic field components respectively. That is, electric fields are forced to go to
761 zero at the inner and outer boundaries, and magnetic fields are forced to have a zero
762 derivative normal to the inner and outer boundaries.

763 These boundary conditions can in principle cause nonphysical reflections at the bound-
764 ary¹⁵. However, in practice, wave activity is concentrated well within the simulation
765 domain. Simulation results are robust under an exchange of Dirichlet and Neumann

¹⁵See, for example, the bottom row of Figure 5.4.

766 boundary conditions (though a self-inconsistent set of boundary condidtions, such as
 767 applying Neumann boundary conditions to B_1 but Dirichlet boundary conditions to B_3 ,
 768 quickly causes instability).

769 The Earthward boundary conditions are as follows.

Between the top of the neutral atmosphere and the bottom of the ionosphere, the model includes a thin, horizontal current sheet representing the ionosphere's E layer[60]. By integrating Ampère's law over the layer, it can be shown[28] that the horizontal electric field values at the edge of the grid are determined by the jump in the horizontal magnetic fields:

$$\underline{\underline{\Sigma}} \cdot \underline{E} = \frac{1}{\mu_0} \lim_{\delta r \rightarrow 0} \left[\hat{r} \times \underline{B} \right]_{R_I - \delta r}^{R_I + \delta r} \quad (5.26)$$

The integrated conductivity tensor $\underline{\underline{\Sigma}}$ can be written in θ - ϕ coordinates as[60]:

$$\underline{\underline{\Sigma}} \equiv \begin{bmatrix} \frac{\Sigma_0 \Sigma_P}{\Sigma_0 \cos^2 \alpha + \Sigma_P \sin^2 \alpha} & \frac{-\Sigma_0 \Sigma_H}{\Sigma_0 \cos^2 \alpha + \Sigma_P \sin^2 \alpha} \\ \frac{\Sigma_0 \Sigma_H}{\Sigma_0 \cos^2 \alpha + \Sigma_P \sin^2 \alpha} & \Sigma_P + \frac{\Sigma_H^2 \sin^2 \alpha}{\Sigma_0 \cos^2 \alpha + \Sigma_P \sin^2 \alpha} \end{bmatrix} \quad (5.27)$$

770 Where α is the angle between the magnetic field and the vertical direction, given by
 771 $\cos \alpha \equiv \frac{-2 \cos \theta}{\sqrt{1+3 \cos^2 \theta}}$, and Σ_P , Σ_H , and Σ_0 are the height-integrated Pedersen, Hall,
 772 and parallel conductivities respectively. Their values are determined by integrating
 773 Kelley's[49] conductivity profiles from Earth's surface to the ionospheric boundary; val-
 774 ues are shown in Table 5.2.

Table 5.2: Integrated Atmospheric Conductivity (S)

	Σ_0	Σ_P	Σ_H
Active Day	424	0.65	6.03
Quiet Day	284	0.44	4.02
Active Night	9	0.01	0.12
Quiet Night	9	0.01	0.12

An expression for the horizontal electric fields at the boundary can be obtained by inverting Equation (5.26). After mapping to covariant coordinates per Equation (5.8), and taking $\Sigma \equiv \det \underline{\underline{\Sigma}}$,

$$\begin{aligned} E_1 &\leftarrow \frac{1}{\mu_0 \Sigma} \lim_{\delta r \rightarrow 0} \left[-\Sigma_{\theta\phi} B_1 - \sqrt{\frac{g_{11}}{g_{22}}} \Sigma_{\phi\phi} B_2 \right]_{R_I-\delta r}^{R_I+\delta r} \\ E_2 &\leftarrow \frac{1}{\mu_0 \Sigma} \lim_{\delta r \rightarrow 0} \left[\sqrt{\frac{g_{22}}{g_{11}}} \Sigma_{\theta\theta} B_1 + \Sigma_{\phi\theta} B_2 \right]_{R_I-\delta r}^{R_I+\delta r} \end{aligned} \quad (5.28)$$

775 In order to compute the atmospheric magnetic field, a scalar magnetic potential (Ψ
776 such that $\underline{B} = \nabla\Psi$) is computed as a linear combination of harmonics. The neutral
777 atmosphere is considered to be a perfect insulator, giving $\nabla \times \underline{B} = 0$. Combined with
778 $\nabla \cdot \underline{B} = 0$ (per Maxwell's equations), Ψ satisfies Laplace's equation, $\nabla^2\Psi = 0$.

Laplace's equation can be solved analytically; however, a numerical solution is preferable to ensure orthonormality on a discrete and incomplete¹⁶ grid. After separating out the radial and azimuthal dependence in the usual way, the latitudinal component of Laplace's equation can be written in terms of $s \equiv -\sin^2\theta$:

$$(4s^2 + 4s) \frac{d^2}{ds^2} Y_\ell + (4 + 6s) \frac{d}{ds} Y_\ell - \frac{m^2}{s} Y_\ell = \ell(\ell+1) Y_\ell \quad (5.29)$$

Using centered differences to linearize the derivatives, Equation (5.29) becomes a system of coupled linear equations, one per field line. It can be solved numerically for eigenvalues $\ell(\ell+1)$ and eigenfunctions Y_ℓ ¹⁷. In terms of the harmonics Y_ℓ , Ψ between the Earth's surface and the top of the atmosphere can be written using eigenweights a_ℓ and b_ℓ :

$$\Psi = \sum_\ell \left(a_\ell r^\ell + b_\ell r^{-\ell-1} \right) Y_\ell \quad (5.30)$$

¹⁶As discussed in Section 5.1, the grid is constrained to finite L , which excludes the equator as well as the poles.

¹⁷Solving Laplace's equation analytically results in spherical harmonics indexed by both ℓ and m , the separation constants for θ and ϕ respectively. In two and a half dimensions, ϕ is not explicitly resolved, so m is set manually.

As a boundary condition for Ψ , Earth is assumed to be a perfect conductor. This forces the magnetic field at Earth's surface to be horizontal; that is, $B_r = \frac{\partial}{\partial r} \Psi = 0$. Noting that solutions to Laplace's equation are orthonormal, each element of the sum in Equation (5.30) must be independently zero at R_E . This allows the coefficients a_ℓ and b_ℓ to be expressed in terms of one another.

$$b_\ell = \frac{\ell}{\ell + 1} R_E^{2\ell+1} a_\ell \quad (5.31)$$

The current sheet at the top of the atmosphere is assumed to be horizontal, so the radial component of the magnetic field must be the same just above and just below it. Taking the radial derivative of Equation (5.30) at the top of the atmosphere, and eliminating b_ℓ with Equation (5.31), gives

$$B_r = \sum_\ell \ell a_\ell R_I^{\ell-1} \left(1 - \lambda^{2\ell+1}\right) Y_\ell \quad \text{where} \quad \lambda \equiv \frac{R_E}{R_I} \sim 0.975 \quad (5.32)$$

The summation can be collapsed by “integrating” over a harmonic¹⁸. Inverse harmonics can be obtained by inverting the eigenvector matrix. Then $Y_\ell \cdot Y_{\ell'}^{-1} = \delta_{\ell\ell'}$ by construction.

$$a_\ell = \frac{1}{\ell R_I^{\ell-1}} \frac{B_r \cdot Y_\ell^{-1}}{1 - \lambda^{2\ell+1}} \quad (5.33)$$

Combining Equations (5.30), (5.31), and (5.33) allows the expression of Ψ at the top and bottom of the atmosphere as a linear combination of radial magnetic field components at the bottom of the ionosphere.

$$\begin{aligned} \Psi_E &= \sum_\ell Y_\ell \frac{R_I}{\ell (\ell - 1)} \frac{(2\ell - 1) \lambda^\ell}{1 - \lambda^{2\ell+1}} B_r \cdot Y_\ell^{-1} \\ \Psi_I &= \sum_\ell Y_\ell \frac{R_I}{\ell (\ell - 1)} \frac{(\ell - 1) + \ell \lambda^{2\ell+1}}{1 - \lambda^{2\ell+1}} B_r \cdot Y_\ell^{-1} \end{aligned} \quad (5.34)$$

¹⁸Because the functions are defined on a discrete grid, their inner product is not an integral, but a sum: $B_r \cdot Y_\ell^{-1} \equiv \sum_i B_r[i] Y_\ell^{-1}[i]$.

Horizontal magnetic fields are obtained by taking derivatives of Ψ .

$$B_1 = \frac{\partial}{\partial u^1} \Psi \quad B_2 = \frac{\partial}{\partial u^2} \Psi \quad (5.35)$$

- 779 Horizontal magnetic field values at the top of the atmosphere are used to impose bound-
780 ary conditions on the electric fields at the bottom of the ionosphere, per Equation (5.28).
781 Those at Earth's surface are valuable because they allow a direct comparison between
782 model output and ground magnetometer data, after being mapped to physical coordi-
783 nates per Equation (5.8).

784 **Chapter 6**

785 **Electron Inertial Effects**

786 As laid out in Chapter 5, Tuna resolves neither parallel currents nor parallel electric
787 fields. This is unfortunate; parallel electric fields generated by kinetic and inertial Alfvén
788 waves (including fundamental field line resonances[81, 97]) are a topic of particular
789 interest in the study of auroral particle precipitation.

Parallel currents and electric fields can be added to Tuna through the consideration of electron inertial effects in Ohm's law:

$$0 = \sigma_0 E_z - J_z \quad \text{becomes} \quad \frac{1}{\nu} \frac{\partial}{\partial t} J_z = \sigma_0 E_z - J_z \quad (6.1)$$

With the addition of the electron inertial term, it is necessary to track the parallel current independent of the parallel electric field¹. Solving by integrating factors² gives

$$J_3 \leftarrow J_3 \exp(-\nu \delta t) + \delta t \frac{ne^2}{m_e} E_3 \exp\left(-\nu \frac{\delta t}{2}\right) \quad (6.2)$$

¹The parallel current J_z is defined on the same points of the Yee grid as E_z . It is offset in time by half of a time step.

²The integrating factors technique is laid out explicitly for Ampère's law in Section 5.4.

From there, the parallel electric field can be updated directly; Equation (5.23) is replaced by the following:

$$E_3 \leftarrow E_3 + c^2 \delta t (g_{31} F^1 + g_{33} F^3) - \frac{\delta t}{\epsilon_0} J_3 \quad (6.3)$$

The present section explores the complications that arise from the addition of the electron inertial term to Ohm's law, as well as a few results that may be gleaned despite those complications. Notably — for reasons discussed in Section 6.3 — the results presented in Chapter 7 do not make use of the electron inertial term.

6.1 The Boris Factor

With the addition of the electron inertial term, a cyclical dependence appears between Ampère's law and Ohm's law:

$$\frac{\partial}{\partial t} E_z \sim -\frac{1}{\epsilon_0} J_z \quad \text{and} \quad \frac{\partial}{\partial t} J_z \sim \frac{ne^2}{m_e} E_z \quad \text{so} \quad \frac{\partial^2}{\partial t^2} E_z \sim -\omega_P^2 E_z \quad (6.4)$$

That is, electron inertial effects come hand in hand with the plasma oscillation. As mentioned in Chapter 4 and shown in Figure 6.1, plasma oscillation is quite fast — several orders of magnitude smaller than Tuna's time step as determined in Section 5.1 ($\sim 10 \mu\text{s}$). This poses a conundrum. At Tuna's usual time step, the plasma oscillation becomes unstable within seconds³. On the other hand, reducing the time step by three orders of magnitude to resolve the plasma oscillation is computationally infeasible; a run slated for an hour would require six weeks to complete. As it happens, this problem can be solved by artificially increasing the parallel electric constant above its usual value of ϵ_0 . Doing so lowers both the speed of light and the plasma frequency within the simulation. This technique — and others like it — has been widespread in numerical modeling since it was presented by Boris in 1970[6]. More recently, Lysak and Song considered its use

³For stability, $\omega_P \delta t < 1$ is necessary.

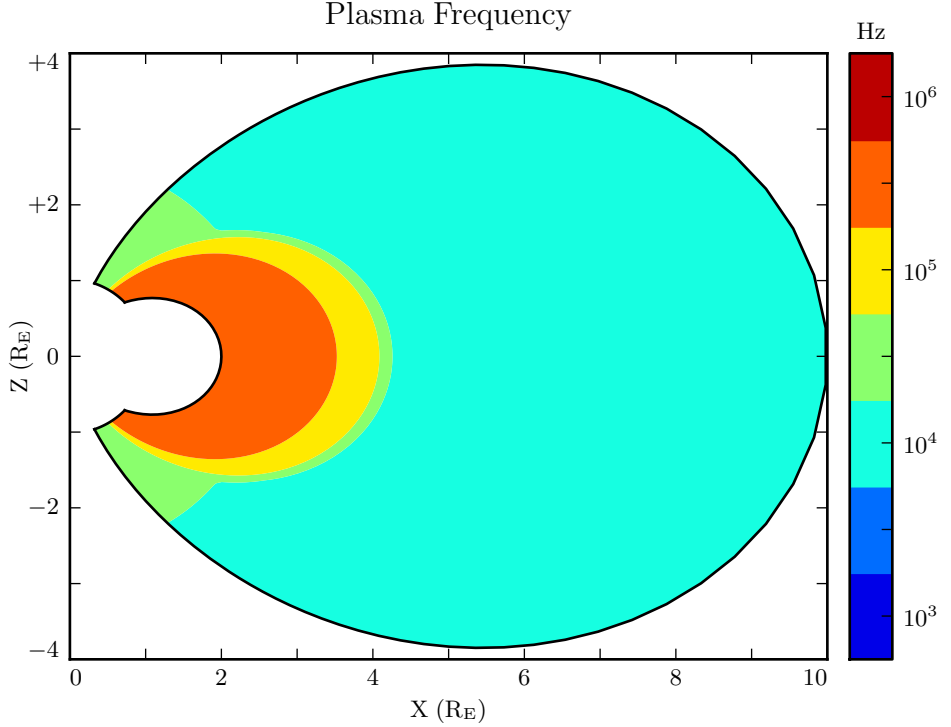


Figure 6.1: The plasma frequency reaches a peak value just under 10^6 Hz near the equator. Outside the plasmasphere, its value is closer to 10^4 Hz, which is still not well-resolved by Tuna's usual time step.

807 specifically for the case of electron inertial effects[62]. The following paraphrases their
 808 argument.

Supposing that the current and electric field are oscillating at frequency ω , the parallel components of Ampère's law and Ohm's law can be written

$$-i\omega\epsilon_0 E_z = \frac{1}{\mu_0} (\nabla \times \underline{B})_z - J_z \quad -\frac{i\omega}{\nu} J_z = \sigma_0 E_z - J_z \quad (6.5)$$

Then, eliminating the current, the parallel electric field can be related to the curl of the magnetic field by⁴

$$\left(1 - \frac{\omega^2 - i\nu\omega}{\omega_P^2}\right) E_z = \frac{c^2}{\omega_P^2} (\nu - i\omega) (\nabla \times \underline{B})_z \quad (6.6)$$

- In Equation (6.6), $\frac{c}{\omega_P}$ is the electron inertial length. While the speed of light and the plasma frequency each depend on ϵ_0 , their ratio does not. This allows an estimation of how much the model should be affected by an artificially-large electric constant (and thus an artificially-small plasma frequency). So long as $\frac{\omega^2 - i\nu\omega}{\omega_P^2}$ remains small compared to unity, the model should behave faithfully.
- For waves with periods of a minute or so, even perhaps-implausibly large Boris factors are allowed; for example, increasing ϵ_0 by a factor of 10^6 gives $\left|\frac{\omega^2 + i\omega\nu}{\omega_P^2}\right| \lesssim 0.01$.

6.2 Parallel Currents and Electric Fields

- As discussed in Section 4.4, parallel electric fields in this regime are expected to be six or more orders of magnitude smaller than the perpendicular electric fields. Numerical results show general agreement: in Figure 6.2, the parallel electric field appears comparable to its perpendicular counterparts only after its been scaled up by six orders of magnitude.
- As such, the inclusion of electron inertial effects does not appreciably impact the simulation's gross behavior; in Faraday's law, $\nabla \times \underline{E}$ is essentially unaffected. Side by side snapshots of the magnetic fields in runs carried out with and without electron inertial effects are not visibly distinguishable⁵ (not shown).
- Even if there is no significant feedback through Faraday's law, it's informative to consider the structures that arise in parallel currents and electric fields driven by perturbations in the ring current. For example, the parallel electric field perturbation (with

⁴From Equation (4.4), $c^2 \equiv \frac{1}{\mu_0 \epsilon_0}$ and $\sigma_0 \equiv \frac{ne^2}{m_e \nu}$ and $\omega_P^2 \equiv \frac{ne^2}{m_e \epsilon_0}$.

⁵In a sense, this is reassuring. It ensures that the present section does not cast doubt on the results presented in Chapter 7, where electron inertial effects are neglected.

Electric Field Snapshots: Quiet Day, 10mHz Current, $m = 16$

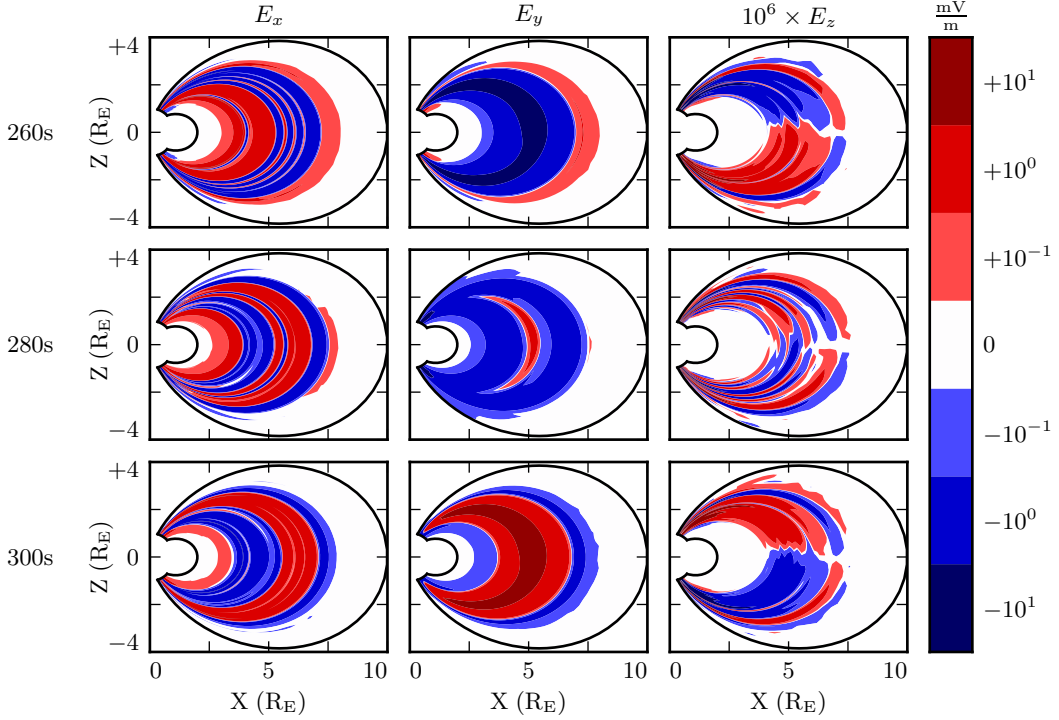


Figure 6.2: Parallel electric fields are smaller than perpendicular electric fields by about six orders of magnitude. As a result, parallel electric fields do not contribute significantly to $\nabla \times \underline{E}$ in Faraday's law.

maxima near the ionosphere) exhibits the opposite harmonic structure to the perpendicular electric field components (which peak near the equator). It is furthermore notable that the parallel electric field (and the parallel current that comes from it) exhibits real and imaginary components of comparable magnitude.

TODO: The compressional component of the magnetic field is also flipped compared to the perpendicular components. Should this have been mentioned in Chapter 3, with the figures showcasing harmonic structure?

At low altitude, where the Hall conductivity muddles all of the electric field components together, parallel currents coincide with strong Poynting flux. The imaginary component of the current lines up with the toroidal Poynting flux (which comes from imaginary E_x

Current and Poynting Flux at 100km: Quiet Day , 16mHz Current

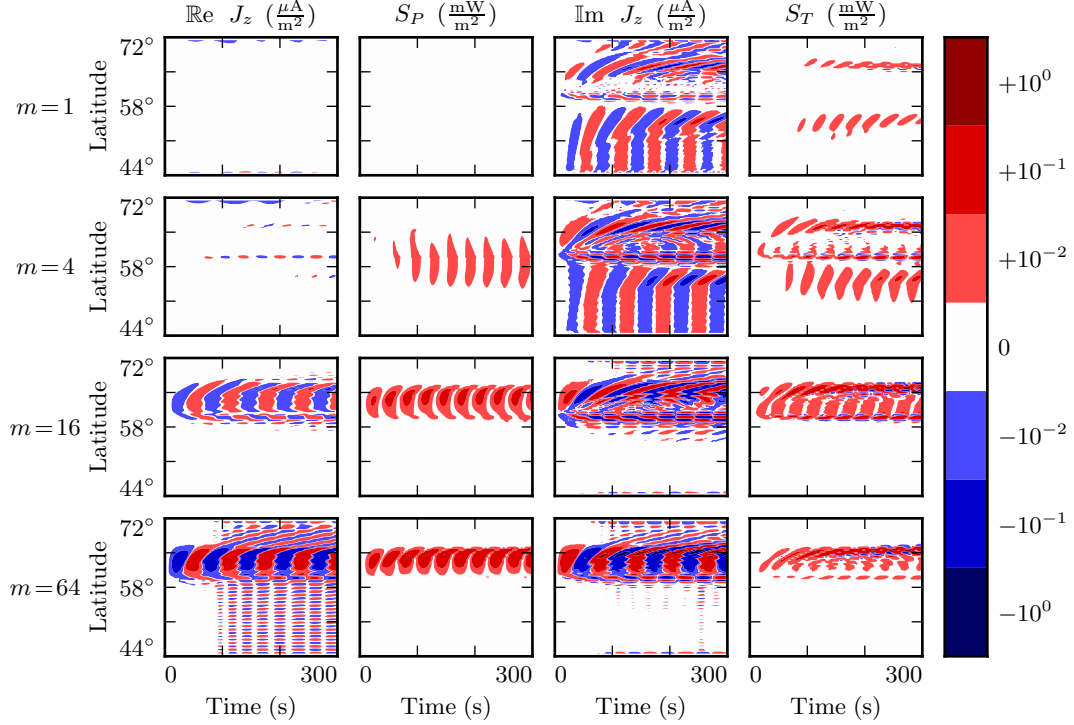


Figure 6.3: TODO: ...

and imaginary B_y^*), while the real current lines up with the poloidal Poynting flux (E_y and B_x^* are real)⁶. This is shown in Figure 6.3, which lays out the real and imaginary components of the parallel current (in the first and third column respectively) next to the poloidal and toroidal Poynting flux (second and fourth columns). Four runs are shown, one per row, with azimuthal modenumbers 1, 4, 16, and 64. Values are measured at an altitude of 100 km, the edge of the simulation.

Notably, the Poynting flux waveforms are rectified — they primarily carry energy Earthward. The current, on the other hand, alternates between upward and downward flow. This effect presumably arises because the current is a linear quantity while the Poynting

⁶As mentioned in Chapter 5, poloidal field components are in practice overwhelmingly real, indicating that they coincide azimuthally with the (real) driving. Toroidal components are overwhelmingly imaginary, which corresponds to an azimuthal offset.

848 flux is quadratic: the electric and magnetic fields that make it up oscillate in phase, so
849 their product is positive even when they are negative.

850 At higher altitude, where the Hall conductivity is small, parallel current is associated
851 only with the toroidal mode. Figure 6.4 shows data from the same runs as Figure 6.3,
852 arranged in the same way, but the values are taken at an altitude of 1000 km instead of
853 100 km.

854 In Figure 6.4, as in Figure 6.3, the imaginary component of the parallel current (third
855 column) coincides more or less with the toroidal Poynting flux (fourth column). How-
856 ever, the real component of the parallel current (first column) is vanishingly small, even
857 when the poloidal Poynting flux (second column) is strong. **TODO: Is this expected?**
858 **Tikhonchuk[97] looks specifically at the toroidal mode when considering shear Alfvén**
859 **waves. Does the poloidal mode count as compressional even when it's guided?**

860 The magnitude of the parallel current tops out over $1 \mu\text{A}/\text{m}^2$, just shy of the up-to-tens
861 of $\mu\text{A}/\text{m}^2$ inferred from ground observations and seen *in situ*[8, 47, 84].

It's also possible to consider the effect of parallel currents and electric fields on the ionosphere's energy budget, per Poynting's theorem:

$$\frac{\partial}{\partial t} u = -\nabla \cdot \underline{E} - \underline{J} \cdot \underline{E} \quad (6.7)$$

862 As shown in Figure 6.5, little energy transfer in the ionosphere is mediated by perpen-
863 dicular components of the Poynting flux. The parallel component of $\underline{J} \cdot \underline{E}$ is comparably
864 unimportant. The energy deposited in the ionosphere by the Poynting flux matches
865 closely with the energy lost to Joule dissipation — as it should, to conserve energy
866 — but according to the model, parallel currents and electric fields do not contribute
867 significantly.

Current and Poynting Flux at 1000km: Quiet Day , 16mHz Current

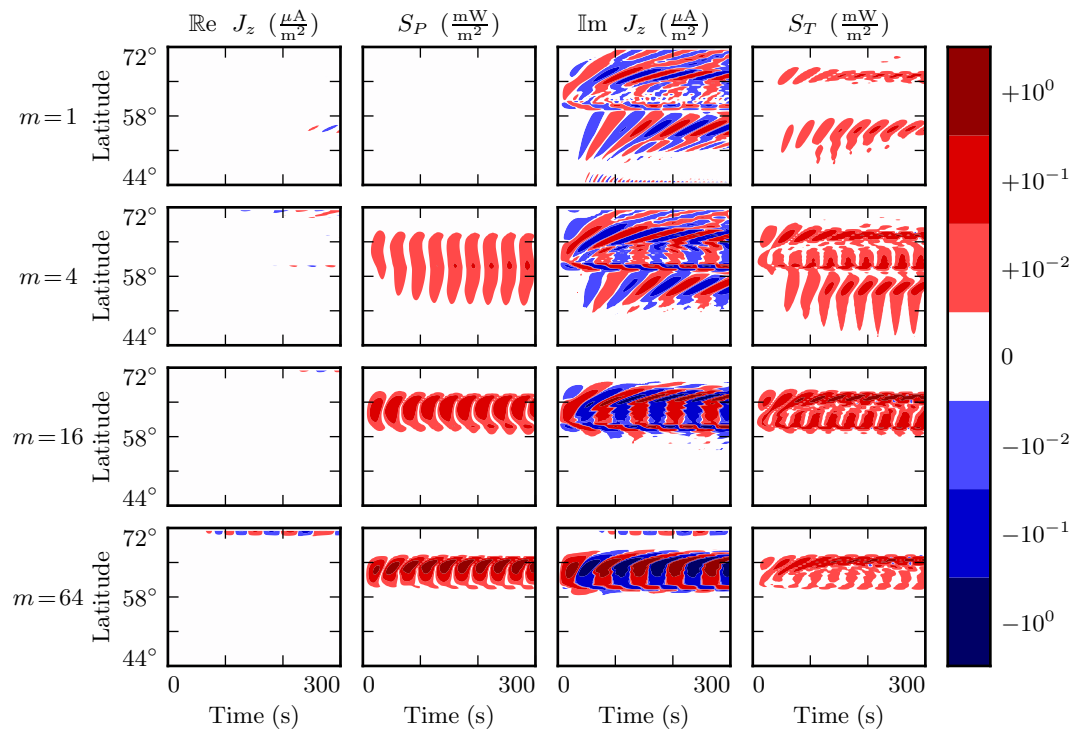


Figure 6.4: TODO: ...

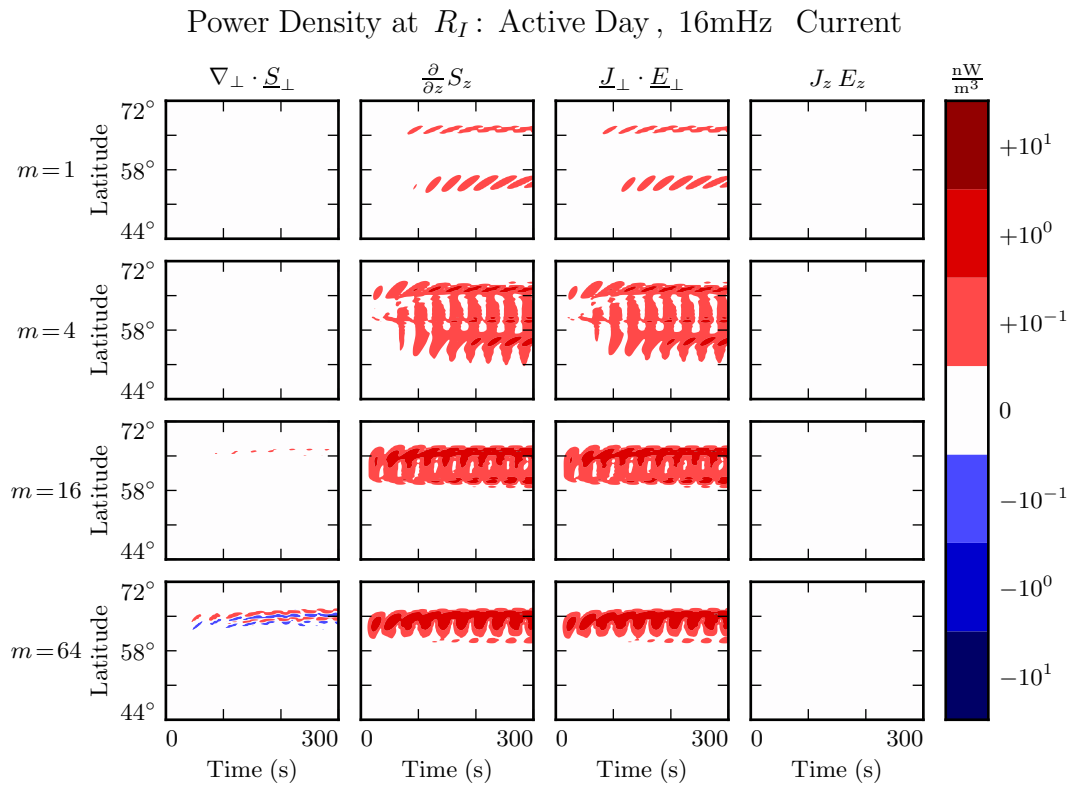


Figure 6.5: While field-aligned currents can be of significant size, they are not particularly good at depositing energy in the ionosphere. Energy deposited by the Poynting flux matches closely with Joule dissipation from the perpendicular currents, while $J_z E_z$ is smaller by several orders of magnitude.

868 **6.3 Inertial Length Scales**

869 It's not quite fair to compare the parallel and perpendicular contributions to $\nabla \times \underline{E}$ as
870 is done in Section 6.2. Perpendicular electric fields are on the order of 1 mV/m, with
871 wavelengths on the order of 10^5 km; they give rise to magnetic field gradients around
872 0.1 nT/s. Parallel electric fields, closer to 10^{-6} mV/m, would need to vary over length
873 scales of 0.1 km to match with that.

874 Such scales are believable. The characteristic length scale of the plasma oscillation is
875 the electron inertial length, $\frac{c}{\omega_p}$, which is on the order of 1 km in the auroral ionosphere
876 and 0.1 km in the low-altitude plasmasphere. However, Tuna's usual grid doesn't resolve
877 structures so fine; its resolution bottoms out closer to 10 km. That is, with the inclusion
878 of electron inertial effects, Tuna's grid is too coarse to resolve all of the waves expected
879 to be present. The model is prone to instability as a result.

880 Figure 6.6 shows a run with perpendicular resolution smaller than the electron inertial
881 length, side by side with an analogous run on the usual grid. In order to carry out
882 the inertial-scale run, several concessions were made to computational cost. The run
883 simulates only a duration of 100 s (other results in previous sections and in Chapter 7
884 show 300 s), and the grid covers only the auroral latitudes from $L = 5$ to $L = 7$.

885 Even so, the run presents a significant computational expense. Spread over 16 cores, a
886 100 s run on Tuna's usual grid takes well under an hour. The inertial-scale run barely
887 finished in 96 hours, the cutoff at the Minnesota Supercomputing Institute⁷.

888 The snapshot shown in Figure 6.6 uses a perpendicular grid resolution of 0.7 km at the
889 Earthward edge, which just satisfies the Nyquist rate for the minimum inertial length
890 of 1.7 km. It's still too coarse. There is clearly some small-scale structure developing in
891 the ionosphere, but it's not well resolved. The large number of "wiggles" portends an
892 imminent crash.

⁷Runtime goes as the inverse square of grid resolution. Not only does finer resolution require more grid cells, but it also gives rise to proportionally smaller crossing times, imposing a smaller time step.

Parallel Electric Fields: Quiet Day, 100s of 16mHz Current, $m = 16$

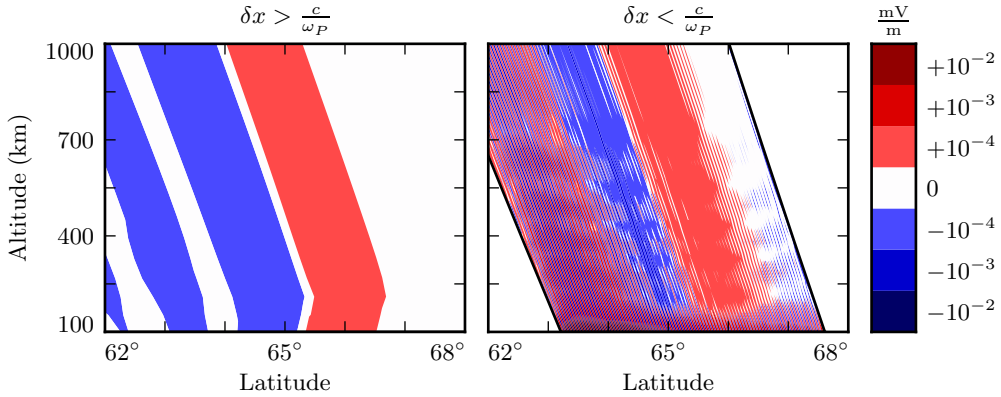


Figure 6.6: The parallel electric field develops significant structure when the perpendicular grid resolution is smaller than the electron inertial length. Unfortunately, such runs are prohibitively expensive. The lower panel — which still fails to resolve wave structure properly — represents a 100-fold increase in computational time.

893 6.4 Discussion

894 TODO: The dispersion relation in Chapter 4 suggests that parallel electric fields should
 895 be smaller than perpendicular electric fields by at least six orders of magnitude. Tuna
 896 agrees.

897 TODO: Tuna computes parallel currents a bit weaker than those that are observed —
 898 $\sim 1 \mu\text{A}/\text{m}^2$ rather than $\sim 10 \mu\text{A}/\text{m}^2$. The currents accompany the toroidal mode, but
 899 not the poloidal mode, except where the two are coupled by a strong Hall conductivity.
 900 Is this expected?

901 TODO: When inertial effects are not properly resolved, the code is prone to instability.
 902 Resolving inertial scales properly presents a prohibitive computational expense.

903 Electron inertial effects present a promising first-principles-based approach to the in-
 904 vestigation of parallel currents and electric fields associated with field line resonances.
 905 Unfortunately, because of the large differences in scale between Pc4 pulsations and the

906 plasma oscillation, the proper deployment of inertial effects presents a prohibitive com-
907 putational expense. Results shown in Chapter 7 make use of the core version of Tuna
908 presented in Chapter 5, which does not include the effects of electron inertia.

909 **Chapter 7**

910 **Numerical Results**

911 In his 1974 paper, Radoski argues that a poloidally-polarized wave should asymptoti-
912 cally rotate to the toroidal polarization[80] as a result of the curved derivative in the
913 meridional plane. The question of finite poloidal lifetimes is considered further in a 1995
914 paper by Mann and Wright[66]. Their numerical work used a straightened field line,
915 with an Alfvén speed gradient in the “radial” direction. They also found a rotation over
916 time from poloidal to toroidal polarization, with the characteristic time proportional to
917 the azimuthal modenumber.

918 **TODO:** Ding et al[21] did similar work just before Mann and Wright, but results were
919 less clear, possibly due to issues with grid resolution (as discussed in [66]).

920 **TODO:** Mann and Wright looked specifically at second harmonics. This work is on first
921 harmonics. (In principle Tuna allows arbitrary driving waveforms and spatial distribu-
922 tions.)

923 The present chapter builds on the aforementioned results by relaxing several of their
924 nonphysical assumptions. Tuna’s geometry (as described in Chapter 5) is far more
925 realistic than Radoski’s half-cylinder or the box model used by Mann and Wright.
926 Magnetic field lines are dipolar. Alfvén speed is based on an empirical profile, and
927 varies along and across field lines. The present work also features driving delivered over
928 time through perturbation of the ring current; past work has instead considered only the

929 evolution of an initial condition. Finally, the present model includes a height-resolved
 930 ionosphere (rather than perfectly-reflecting boundaries). The ionospheric conductivity
 931 provides a direct coupling between the poloidal and toroidal modes, in addition to
 932 dissipating energy.

Energy is computed per Poynting's theorem, with due consideration of the unusual geometry. Energy density is integrated over the meridional plane, but not in the azimuthal direction, giving units of gigajoules per radian; more than anything else, this serves as a reminder that the waves under consideration are azimuthally localized. The energy in the poloidal mode and the energy in the toroidal mode are, respectively,

$$U_P = \int \frac{du^1 du^3}{2\mu_0 \sqrt{g}} \left(B_x^2 + \frac{1}{v_A^2} E_y^2 \right) \quad U_T = \int \frac{du^1 du^3}{2\mu_0 \sqrt{g}} \left(B_y^2 + \frac{1}{v_A^2} E_x^2 \right) \quad (7.1)$$

933 TODO: We look at the interplay between poloidal-to-toroidal rotation, Joule dissipation,
 934 etc.

935 TODO: The overarching motivation for this work is that Pc4 pulsations vary in interesting
 936 ways with respect to azimuthal modenumber, and that prior models have been
 937 unable to give a good picture of that behavior.

938 TODO: It's possible that the contour plots (Sections 7.2 and 7.4) should go before the
 939 line plots (Sections 7.1 and 7.3). They sorta depend on one another. Unclear if there's
 940 a better way to divide things up.

941 7.1 Finite Poloidal Lifetimes: Dayside

942 Each subplot in Figures 7.1 and 7.2 is analogous to Figure 3 in Mann and Wright's
 943 paper[66]. Blue lines show the total energy in the poloidal mode as a function of time.
 944 Red lines show toroidal energy. Runs are organized such that driving frequency is
 945 constant down each column, and azimuthal modenumber is constant across each row.
 946 Axis bounds are held constant across all subplots.

947 The 28 runs shown in Figure 7.1 use a high-conductivity profile, corresponding to the
 948 dayside with low solar activity (shown in Section 5.2). The two dayside profiles —

949 active and quiet — are contrasted briefly in Section 7.5. However, the primary focus is
950 on the difference between the dayside and the nightside. The differences between the
951 two dayside profiles are minor in comparison.

952 The fact that red (toroidal) lines appear at all speaks to the coupling of the poloidal
953 and toroidal modes. As discussed in Section 5.3, driving in Tuna is delivered purely
954 into the poloidal electric field (reflecting the azimuthal direction of the ring current).

955 As expected, the rotation from poloidal to toroidal is slowest at large azimuthal mode-
956 numbers. The toroidal energy overtakes the poloidal energy within a single drive period
957 at $m = 4$; at $m = 64$, the most of the energy is in the poloidal mode for ~ 10 periods.
958 However, the relationship between azimuthal modenumber and rotation timescale is not
959 linear, as was suggested by Mann and Wright. Instead, the rotation is fastest at $m = 4$.

960 This hints at two competing effects, and there are only so many options. In addition
961 to the poloidal-to-toroidal rotation, the two modes are coupled by the ionospheric Hall
962 conductivity; energy is also lost when waves propagate out of the simulation domain,
963 when driving interferes destructively with a wave, and as a result of Joule dissipation.

964 In practice, the Hall conductivity does not move large amounts of energy between the
965 poloidal and toroidal modes. In fact, when the runs shown in Figure 7.1 are repeated
966 with Hall conductivity uniformly zero (not shown), the energy curves do not change
967 appreciably.

968 Joule dissipation — a recurring topic in the present chapter — is a major player in the
969 simulation’s energy economy, but does not depend directly on the azimuthal modenum-
970 ber. Similarly, azimuthal modenumber does not immediately impact the interference
971 between a wave and its driver.

972 That leaves the propagation of energy across field lines, which does explain the ob-
973 served behavior. As the azimuthal modenumber increases past order unity, compres-
974 sional Alfvén waves in the Pc4 band become evanescent¹. Runs in the top two rows
975 lose considerable sums of energy as a result of waves propagating out of the simulation

¹See Section 4.4.

976 domain. In contrast, runs conducted at higher modenumber do not permit the com-
977 pressional propagation of Alfvén waves, so energy does not escape through the outer
978 boundary.

979 Notably, the low-modenumber runs at 19 mHz do accumulate significant energy over
980 time, while those at 13 mHz, 16 mHz, and 22 mHz falter. This response is likely non-
981 physical, and is discussed in Section 7.2.

982 In each run, the energy of the system is asymptotically determined by the balance
983 between the energy input (from driving) and the energy loss (through Joule dissipation
984 in the ionosphere and escape through the boundary). When the driving frequency
985 matches closely with the local Alfvén frequency, energy accumulates over a number of
986 drive periods, leading to a relatively large asymptotic energy in the system.

987 The system’s resonant frequency (for a fundamental poloidal mode at $L \sim 5$) is affected
988 significantly by the size of the plasmasphere. In Figure 7.1, with the plasmapause at
989 $L_{PP} = 4$, the system resonates at 19 mHz at low m ; as m becomes large, the resonant
990 frequency is closer to 22 mHz. Figure 7.2 shows the effect of moving the plasmapause
991 to $L_{PP} = 5$: resonance is closer to 16 mHz. The runs are otherwise identical to those
992 shown in Figure 7.1.

993 **TODO:** In most cases, the energy in the toroidal mode exceeds the energy in the poloidal
994 mode.

995 **TODO:** The late, long dips in energy are probably due to “beats” in the interference
996 between the driving frequency and the bounce frequency.

Poloidal (Blue) and Toroidal (Red) Energy: Quiet Day , $L_{PP} = 4$, $L_{drive} = 5$

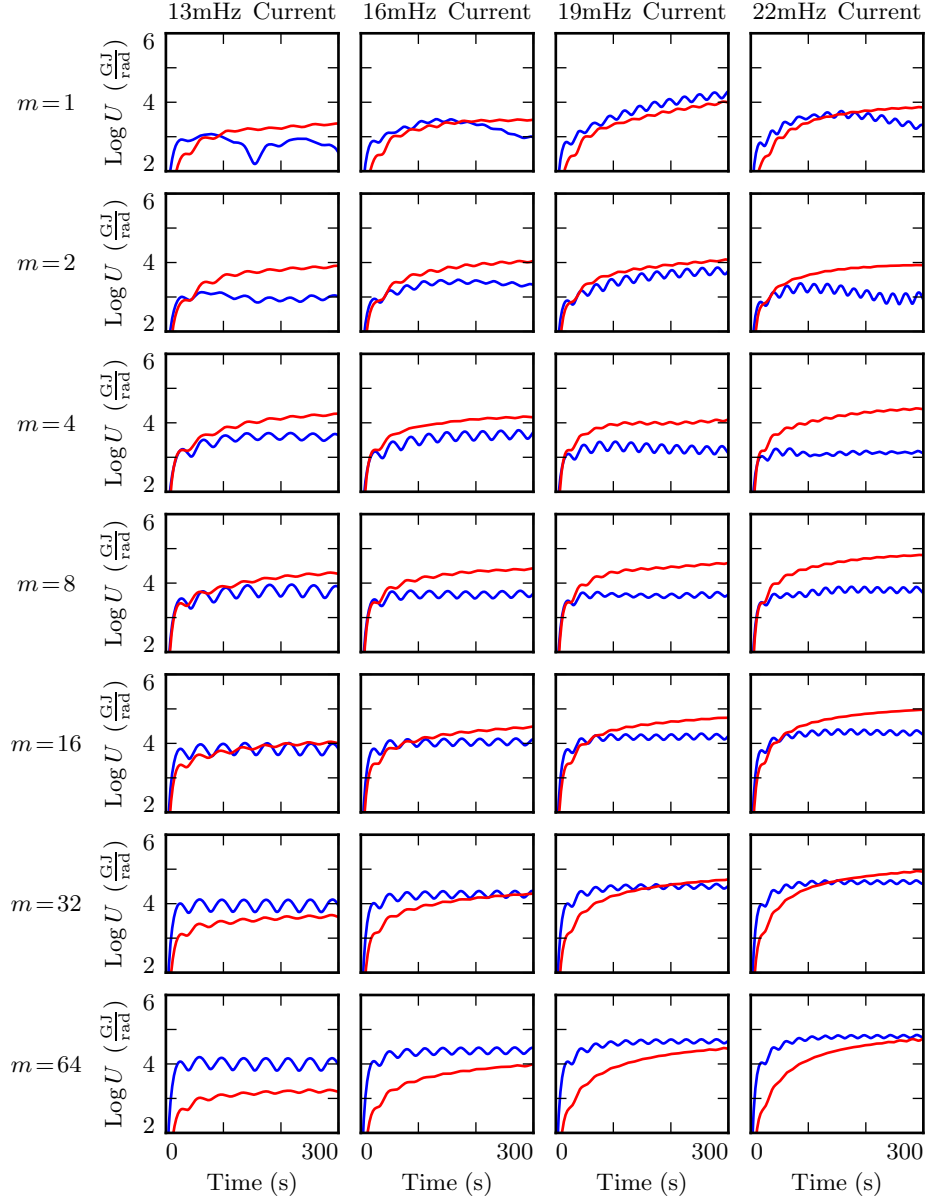


Figure 7.1: Each subplot above corresponds to a 300s run of Tuna. Driving is continuously injected into the poloidal mode (energy in blue). The waves rotate asymptotically to the toroidal mode (red). When the azimuthal modenumber (rows) is large, the rotation is slower. The driving frequency (columns) also affects the asymptotic accumulation of energy.

Poloidal (Blue) and Toroidal (Red) Energy: Quiet Day , $L_{PP} = 5$, $L_{drive} = 5$

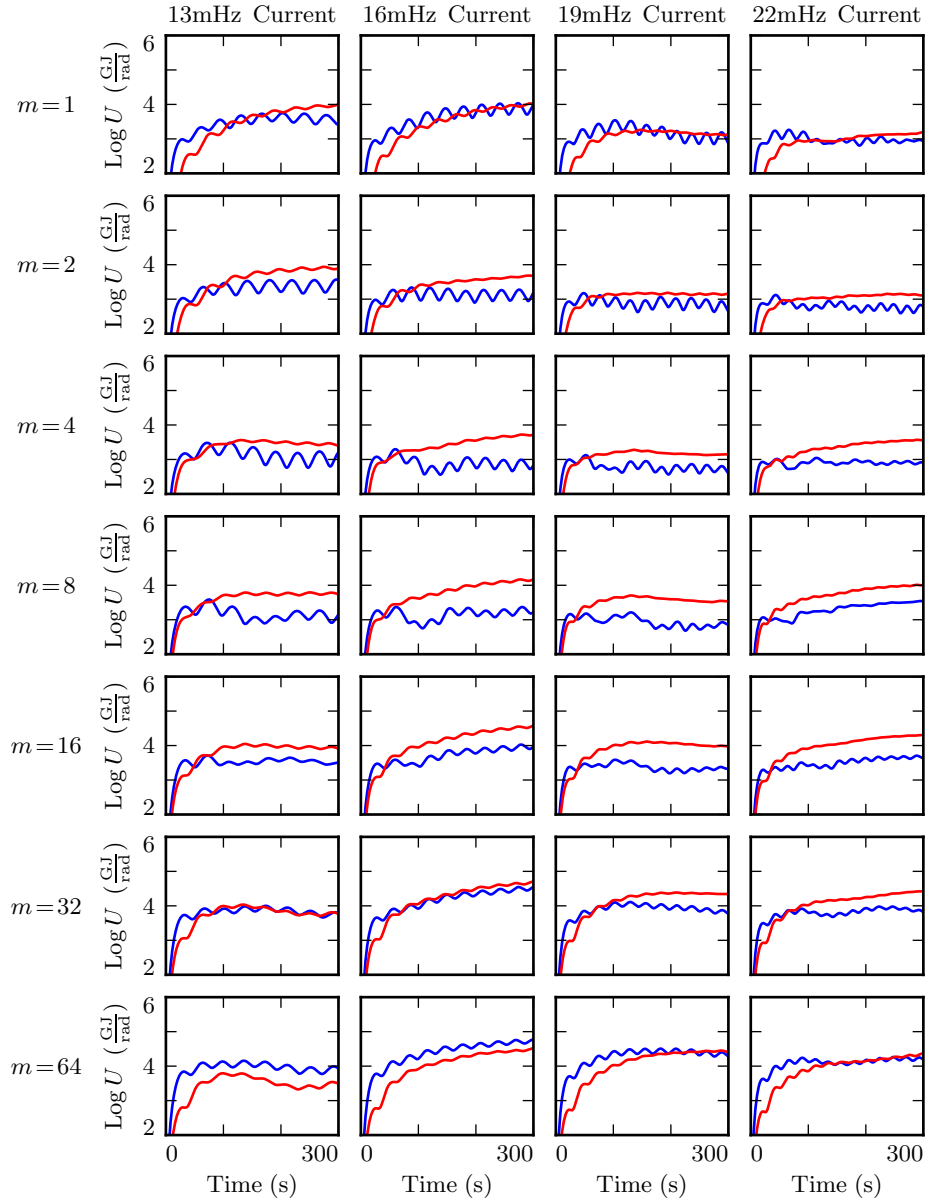


Figure 7.2: Above is a figure identical to Figure 7.1, except that the plasmapause has been moved from $L_{PP} = 4$ to $L_{PP} = 5$. This affects which driving frequency is closest to the resonant Alfvén frequency, and hence is most effective in causing a buildup of energy over time.

997 7.2 Spatial Distribution of Energy: Dayside

998 Looking a bit deeper, it's possible to comment on the structure of the poloidal and
999 toroidal modes, not just their magnitudes. The subplots in Figures 7.3 to 7.5 are
1000 arranged analogously to those in Section 7.1: each comes from a different run, mode-
1001 number is held constant across each row, and frequency down each column.

1002 Contours represent energy density, averaged over the volume of a flux tube. The vertical
1003 axis shows L -shell, while the horizontal axis is time. As above, poloidal and toroidal
1004 energy density are computed separately.

1005 Figure 7.3 shows why, at low modenumber, the poloidal mode does not resonate well.
1006 Its compressional component allows energy to be spread broadly in L — in fact, at
1007 $m = 1$, no energy buildup at all is apparent at the location of the driving.

1008 Some energy moves inward, and is trapped in the plasmapause's steep Alfvén speed
1009 gradient (particularly visible in the 16 mHz, $m = 4$ run). Some energy builds up in a
1010 third harmonic resonance near the outer boundary (shown best in runs with $m = 1$). The
1011 time spent propagating across field lines counts against the poloidal mode's finite lifetime
1012 — by the time a poloidally-polarized wave reaches the outer boundary, a significant
1013 fraction of its energy has rotated to the toroidal mode.

1014 It's likely that at 19 mHz, with $m = 1$, the response is artificially amplified through
1015 interaction with the boundary conditions. As mentioned in Section 5.5, nonphysical
1016 reflections can occur when waves are very close to the boundary. In most cases, waves
1017 are not localized at the boundary, so this is not a concern.

1018 The peak energy density in the bottom-right run (22 mHz driving, $m = 64$) is by far the
1019 largest of any run in Figure 7.3. The azimuthal modenumber is large, so the poloidal
1020 mode is purely guided; no time is wasted with movement across magnetic field lines.
1021 And, crucially, the frequency of the driving aligns closely with the resonant frequency
1022 where it's delivered. Other runs on the bottom row also have $m = 64$ (and so are also
1023 guided), but their driving frequencies do not align with the local resonant frequency.
1024 As a result, they do not accumulate energy over a large number of drive periods.

1025 Similar behavior can be seen in Figure 7.4 (which shows the same runs as Figure 7.2,
1026 with the plasmapause moved to $L_{PP} = 5$ from its default location at $L_{PP} = 4$). A third
1027 harmonic resonance can be seen at the outer boundary for runs on the top row ($m = 1$).
1028 The effect of the plasmapause is particularly visible in the middle row, $m = 8$, where
1029 energy accumulates both just inside and just outside $L_{PP} = 5$. At high modenumber,
1030 the driving resonates best at 16 mHz; at other frequencies, energy density has a lower
1031 asymptotic value, which is reached more quickly.

1032 In Figures 7.3 and 7.4, the poloidal contours show energy smeared across a swath of
1033 L -shells. On the other hand — as shown in Figure 7.5 — the toroidal mode appears
1034 only where the drive frequency matches the local eigenfrequency.

1035 A horizontal line drawn through the Alfvén speed frequency profiles (recall Figure 3.1)
1036 intersects the profile up to three times: once as the Alfvén frequency drops through the
1037 Pc4 range from its low-latitude peak, again as the Alfvén frequency rises sharply at the
1038 plasmapause, and a third time as the Alfvén frequency drops asymptotically. Toroidal
1039 waves can be seen resonating at all three of these locations in the $m = 4, 19$ mHz run
1040 in Figure 7.5, along with a third harmonic at large L .

1041 This is consistent with observations: toroidal resonances are noted for having frequencies
1042 which depend strongly on L , in contrast to the poloidal mode’s less-strict relationship
1043 between frequency and location.

1044 The dayside poloidal modes shown in Figures 7.3 and 7.4 attain an energy density on the
1045 order of 10^{-1} nJ/m³ only under ideal conditions: high modenumber runs with driving
1046 close to the local Alfvén frequency. Between the 56 dayside runs shown, such energy
1047 density appears only twice. On the other hand, the toroidal mode reaches $\sim 10^{-1}$ nJ/m³
1048 in six of the runs in Figure 7.5 alone. That is, the poloidal mode only exhibits a high
1049 energy density on the dayside only when conditions are ideal; the toroidal mode isn’t
1050 nearly so particular.

Poloidal Energy Density by L-Shell: Quiet Day , $L_{PP} = 4$, $L_{drive} = 5$

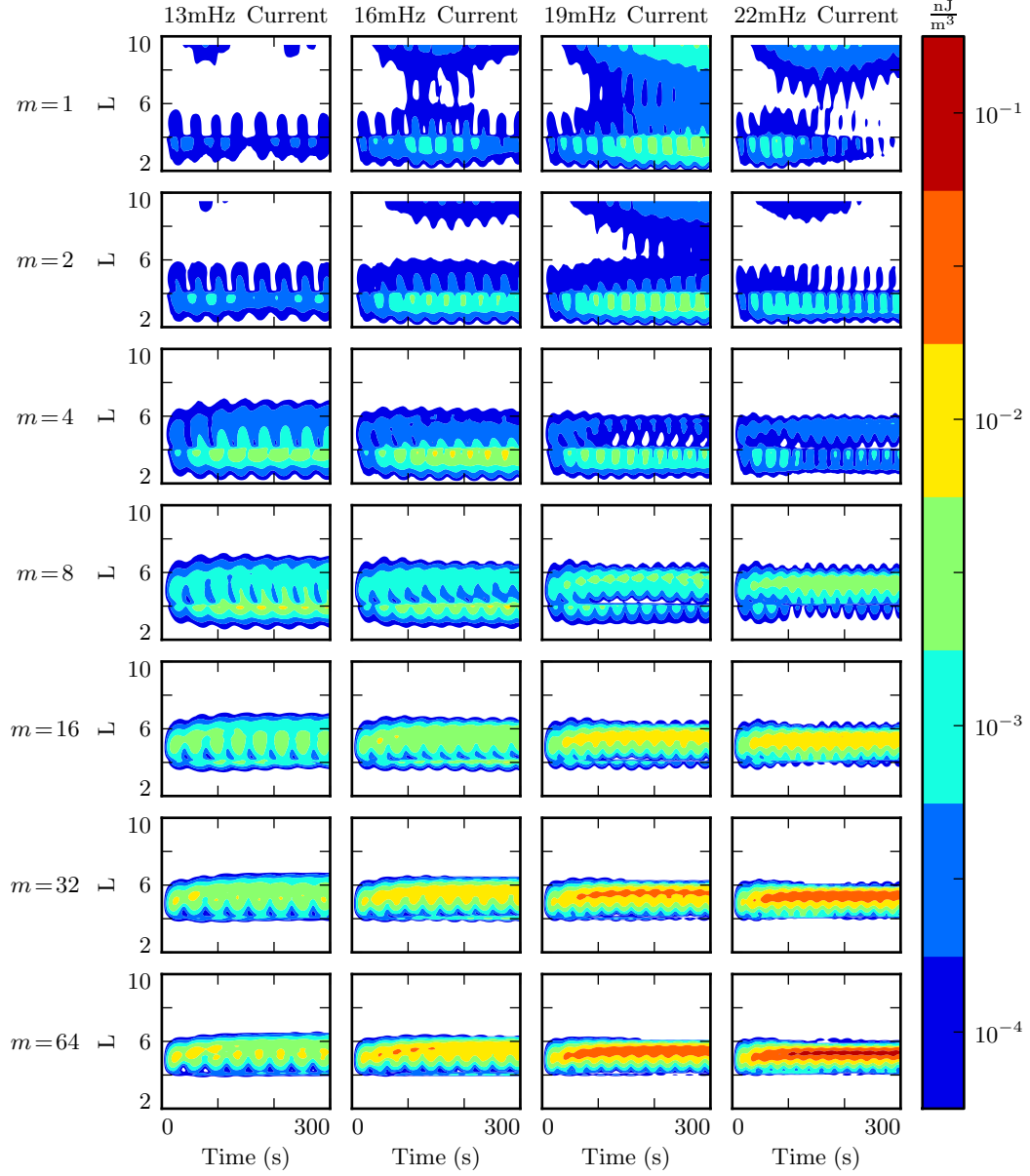


Figure 7.3: Each subplot above corresponds to a 300s run of Tuna, driven in the poloidal mode. At low m , energy instead moves radially and rotates quickly to the toroidal mode, precluding the formation of poloidal FLRs. At high m , the poloidal mode is guided, and the mode rotation is slow, allowing a strong resonance — but only when the driving frequency matches the local Alfvén frequency.

Poloidal Energy Density by L-Shell: Quiet Day , $L_{PP} = 5$, $L_{drive} = 5$

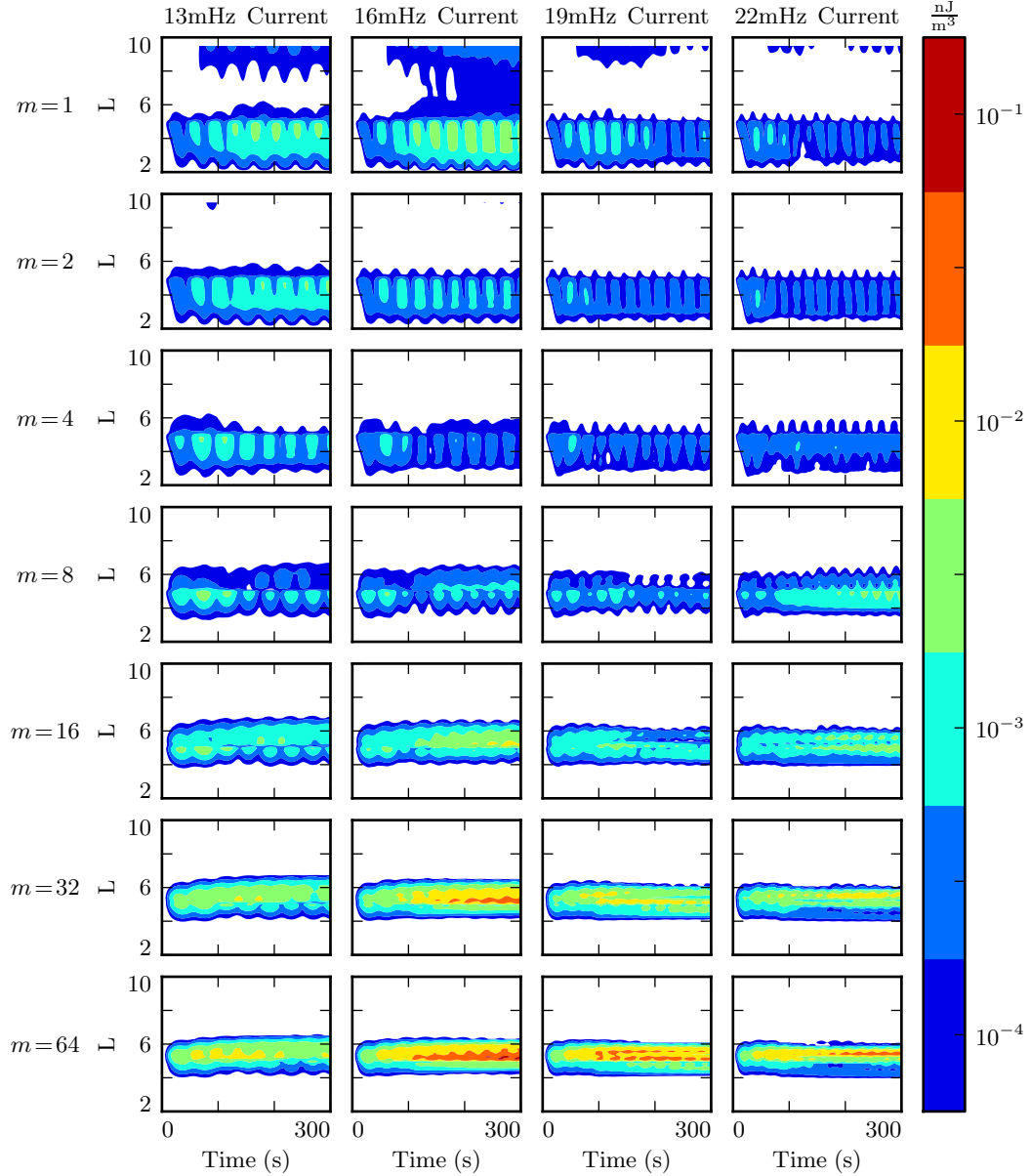


Figure 7.4: The Alfvén frequency profile is significantly affected by the size of the plasmasphere. The runs shown above are identical to those in Figure 7.3, except that the plasmapause has been moved from $L_{PP} = 4$ to $L_{PP} = 5$. As a result, the most effective resonance at $L \sim 5$ is shifted from 22 mHz to 16 mHz.

Toroidal Energy Density by L-Shell: Quiet Day , $L_{PP} = 4$, $L_{drive} = 5$

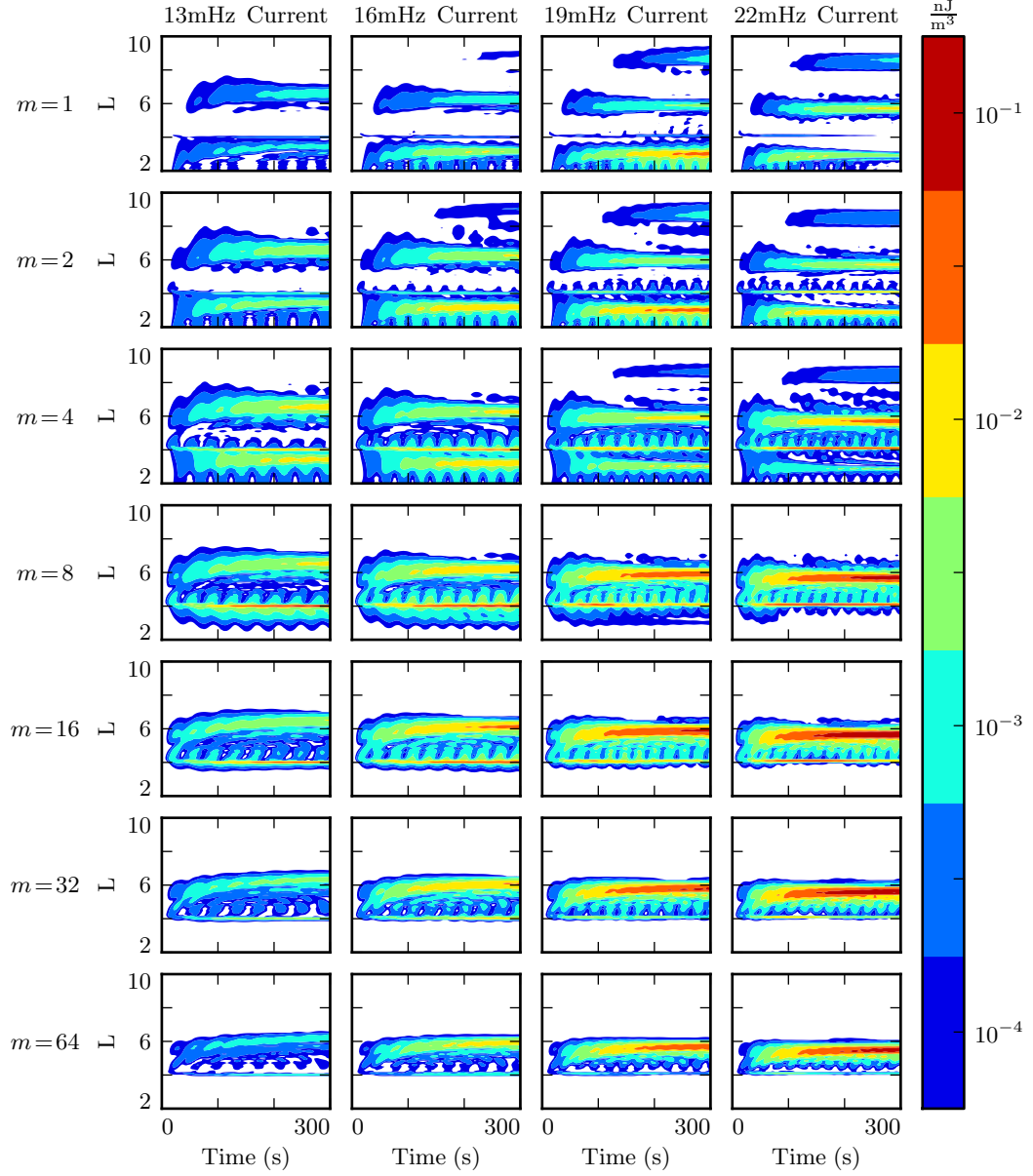


Figure 7.5: On the dayside, energy accumulates in the toroidal mode only at L values where the drive frequency matches a local eigenfrequency. This is in contrast to the more smeared appearance of the poloidal contours shown in Figures 7.3 and 7.4. Furthermore, the toroidal mode attains a high energy density under more diverse conditions than the poloidal mode.

1051 **7.3 Finite Poloidal Lifetimes: Nightside**

1052 Compared to the dayside ionosphere employed in Section 7.1, the nightside profiles
1053 exhibit two major differences. The ionospheric conductivity is lower, and the Alfvén
1054 speed is higher. The present section and Section 7.4 show results using only the active
1055 nightside profile. The differences between the quiet and active nightside ionospheric
1056 profiles are small compared to the differences between either dayside profile and either
1057 nightside profile; all four profiles are briefly compared in Section 7.5.

1058 The low conductivity on the nightside gives rise to strong Joule dissipation. Waves are
1059 damped out in just a few bounces, so asymptotic energy values are reached quickly.
1060 Even so, the poloidal-to-toroidal rotation is qualitatively the same as on the dayside.
1061 The further the azimuthal modenumber from the rotation peak at $m = 4$, the lower the
1062 asymptotic toroidal energy level is compared to the poloidal. If anything, the effect is
1063 exaggerated by the small dissipation timescale. When $m = 64$, no more than $\sim 10\%$ of
1064 the energy in the poloidal mode rotates to the toroidal mode before being lost.

1065 Figure 7.6 is arranged analogously to the figures in Section 7.1: each subplot is an inde-
1066 pendent run, drive frequency is constant down each column, and azimuthal modenumber
1067 is constant across each row. Poloidal energy is blue; toroidal energy is red.

1068 The lower energies in Figure 7.6 (compared to Figure 7.1, the analogous dayside runs)
1069 are not entirely due to increased Joule dissipation. Due to the difference in electric
1070 constant between the dayside and nightside magnetospheres², resonant frequencies just
1071 outside the typical ($L_{PP} = 4$) plasmapause fall well outside the $Pc4$ range. None of
1072 the frequencies shown in Figure 7.6, when delivered at $L_{drive} = 5$, align with the local
1073 eigenfrequency.

1074 As in Section 7.1, the 19 mHz run with $m = 1$ is an apparent exception. A large
1075 amount of energy builds up in a third harmonic very close to the outer boundary. The
1076 interaction is likely nonphysical.

1077 **TODO:** It may be significant that $\int \sigma dz$ is constant across all L -shells, but $\int \frac{\sigma}{v_A^2} dz$ is
1078 not.

²See Figure 3.1.

1079 Behavior closer to resonance is shown in Figure 7.7. The plasmapause remains at
1080 $L_{PP} = 4$, but the driving is moved out to $L_{drive} = 6$, at which point the local Alfvén
1081 frequency overlaps the Pc4 frequency band.

1082 There is surprisingly little difference between Figures 7.6 and 7.7 (the subplots of which
1083 are arranged analogously). Asymptotic energy levels vary — in the case of high m and
1084 low frequency, runs in Figure 7.7 are more energetic by an order of magnitude or more
1085 — but the qualitative behavior is the same. Driving is balanced by dissipation over the
1086 course of just a few drive periods. Dissipation outstrips poloidal-to-toroidal rotation in
1087 the case of large azimuthal modenumber. And, unlike on the dayside, the toroidal mode
1088 typically does not match the asymptotic energy level seen in the poloidal mode.

Poloidal (Blue) and Toroidal (Red) Energy: Active Night , $L_{PP} = 4$, $L_{drive} = 5$

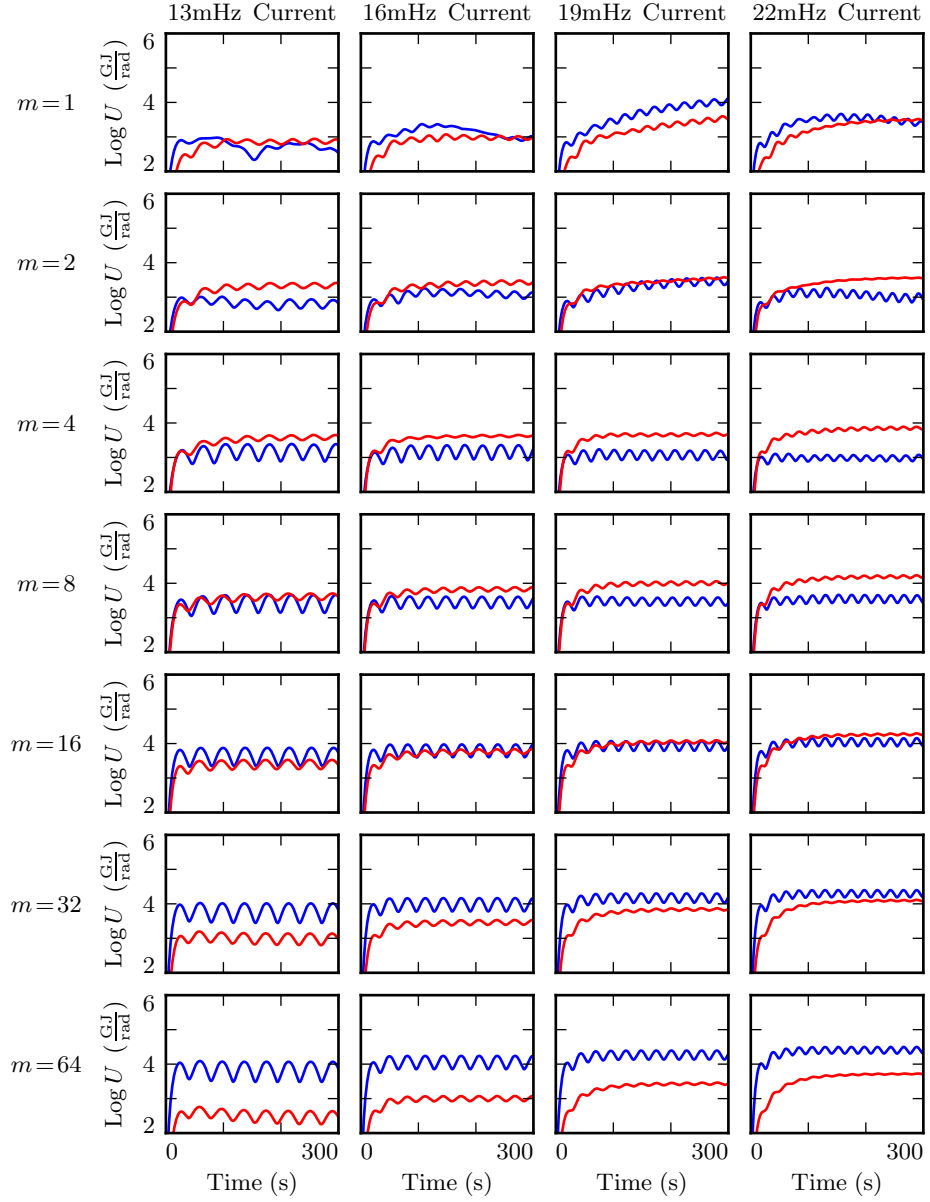


Figure 7.6: On the nightside, driving in the $\text{Pc}4$ band is not resonant at $L \sim 5$. This — combined with the lower ionospheric conductivity — causes the poloidal (blue) and toroidal (red) energies to quickly reach their asymptotic values. As on the dayside, energy rotates from poloidal to toroidal most effectively at small-but-finite m .

Poloidal (Blue) and Toroidal (Red) Energy: Active Night , $L_{PP} = 4$, $L_{drive} = 6$

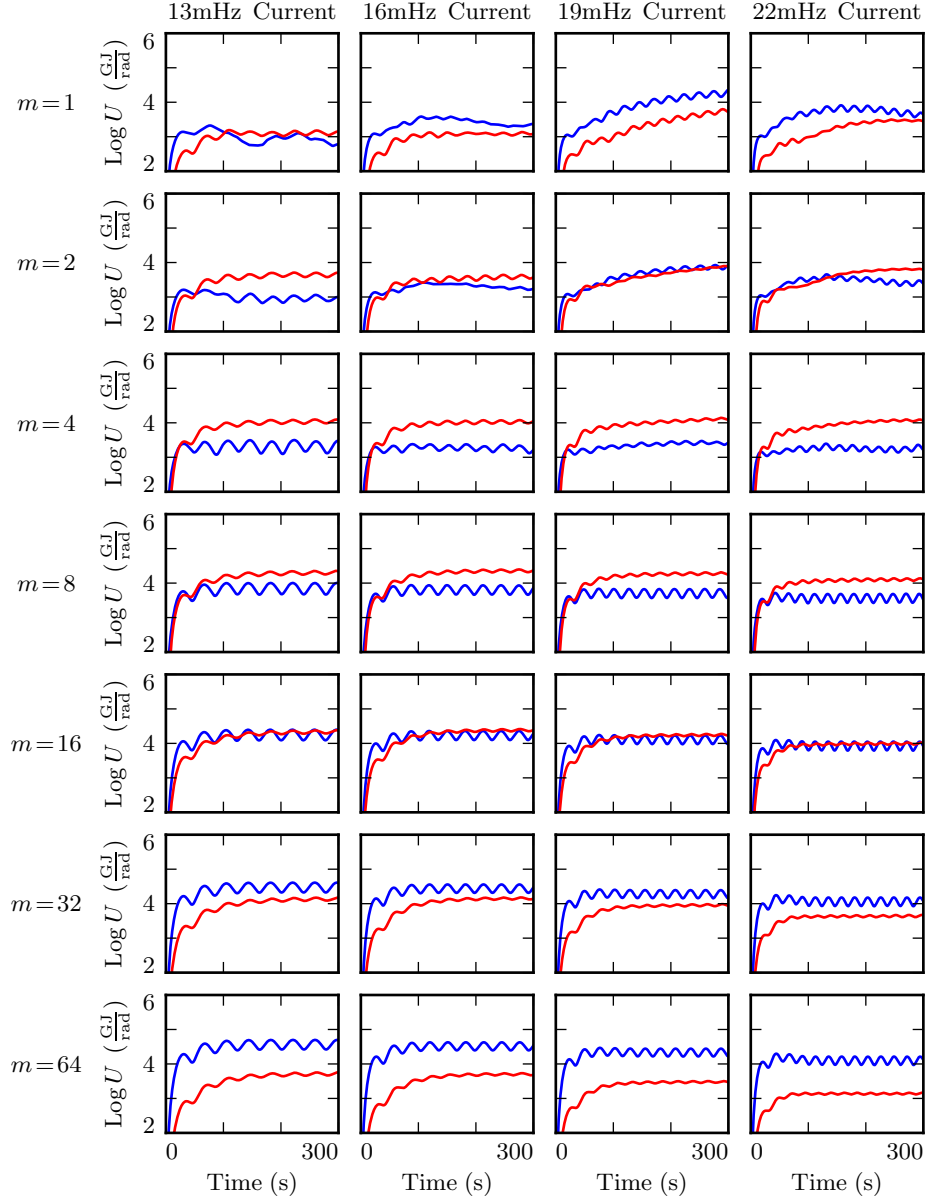


Figure 7.7: Even when the drive frequency does line up with the local Alfvén frequency, the low ionospheric conductivity prevents the accumulation of energy over the course of a large number of drive periods. Asymptotic energies are higher above than in analogous runs shown in Figure 7.6 — but compared to the dayside, the asymptotic energies are still small, and are still reached quickly.

1089 **7.4 Spatial Distribution of Energy: Nightside**

1090 Figure 7.8 shows the radial distribution of poloidal energy on the nightside — a slice of
1091 each run shown in Figure 7.7. Broadly speaking, the behavior is consistent with that
1092 seen in Section 7.2: energy is smeared across L -shells at small m and guided at high
1093 m , with particularly strong energy buildup when the drive frequency matches the local
1094 Alfvén frequency.

1095 As discussed in Section 7.3, the nightside’s relatively low ionospheric conductivity in-
1096 creases the rate of dissipation. Asymptotic energy content is reached quickly, and is
1097 small compared to that seen in analogous dayside runs.

1098 The effect is particularly pronounced at large modenumber, where the poloidal-to-
1099 toroidal rotation timescale is slower than the nightside dissipation timescale. In most
1100 of the dayside runs shown in Section 7.2, the toroidal mode asymptotically exceeds the
1101 poloidal mode both in terms of total energy content and in terms of peak energy density.
1102 On the nightside, the opposite is true. At high modenumber, the asymptotic rotation
1103 from the poloidal mode to the toroidal mode doesn’t occur until most of the energy has
1104 been lost to Joule dissipation. Peak poloidal energy densities at $m = 64$ exceed their
1105 toroidal counterparts — shown in Figure 7.9 — by an order of magnitude.

1106 **TODO:** On the nightside, unlike the dayside, toroidal contours are messy. Why?

Poloidal Energy Density by L-Shell: Active Night , $L_{PP} = 4$, $L_{drive} = 6$

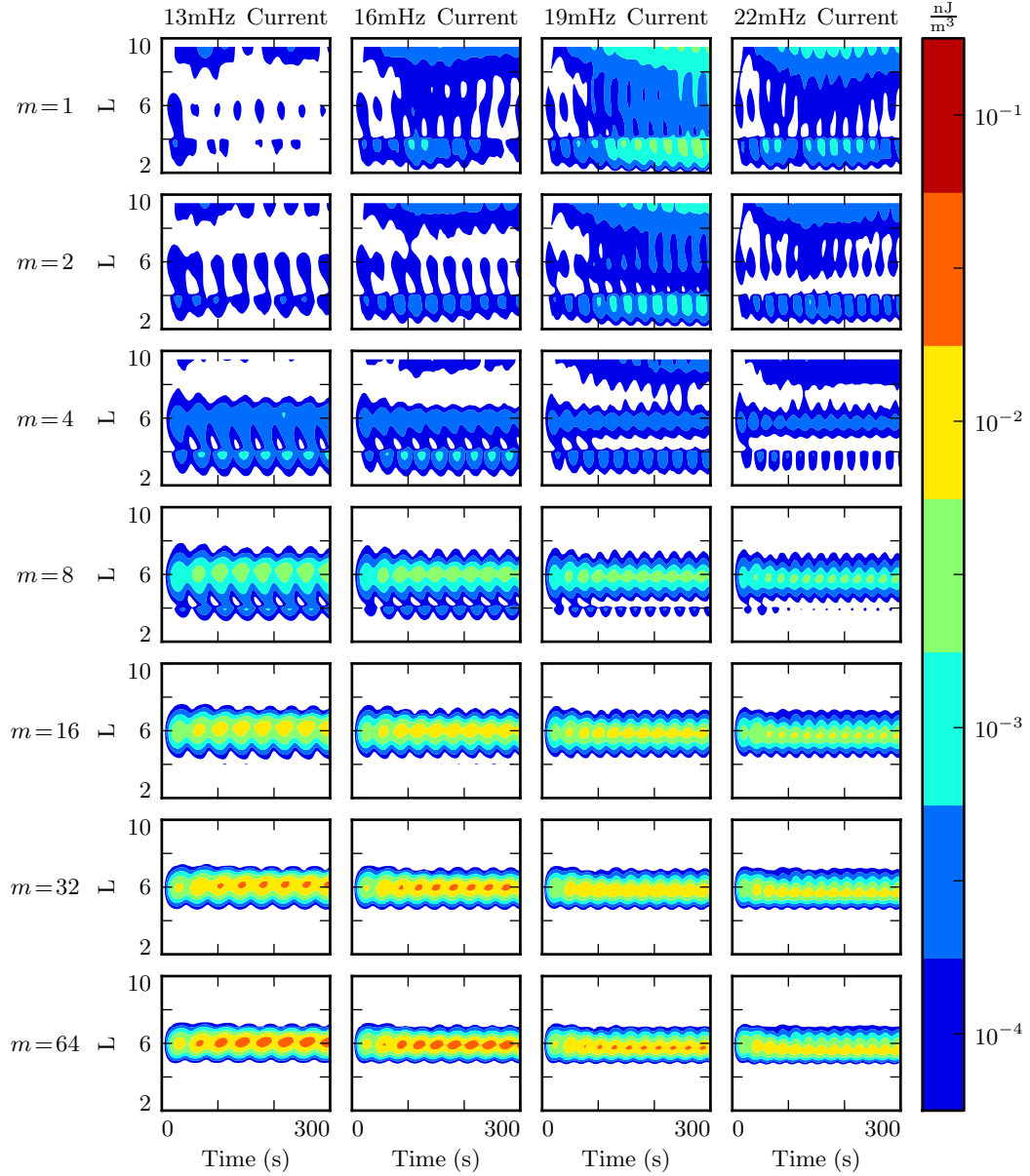


Figure 7.8: The behavior of the poloidal mode on the nightside matches qualitatively with the behavior on the dayside. At low m , energy is lost to the outer boundary. At high m , resonance occurs, but only if the drive frequency is close to the local eigenfrequency. The big difference is that, due to the increased dissipation in the ionosphere, asymptotic energy densities are relatively low, and reached relatively quickly.

Toroidal Energy Density by L-Shell: Active Night , $L_{PP} = 4$, $L_{drive} = 6$

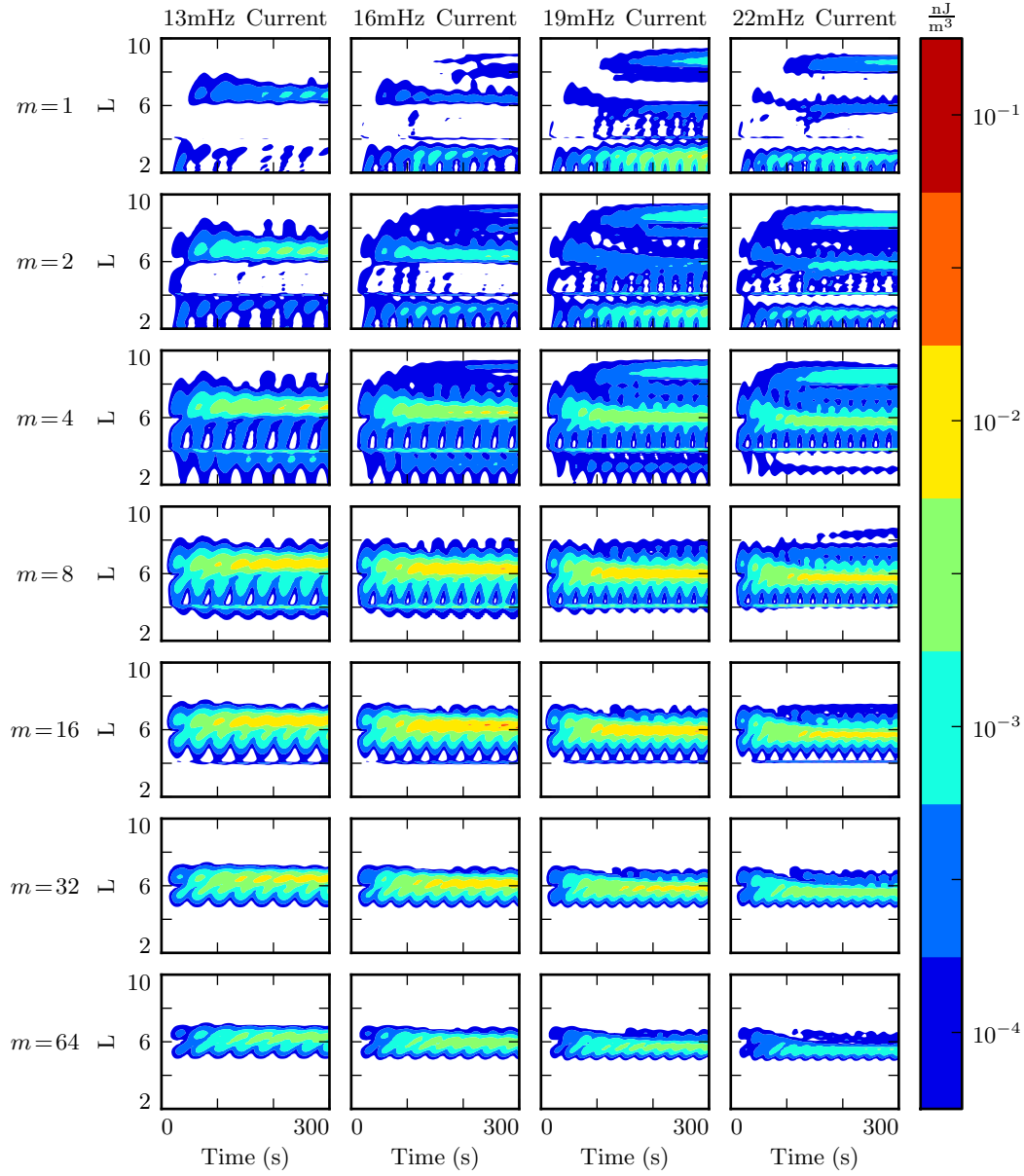


Figure 7.9: In low- m runs, the poloidal mode loses energy to the outer boundary, which impairs the growth of the toroidal mode. At high m , poloidal-to-toroidal rotation is slow compared to dissipative timescales on the nightside. The strongest toroidal waves — which are still weak compared to those on the dayside — thus appear at moderate m .

1107 7.5 Ground Signatures and Giant Pulsations

1108 While the majority of the action is in space, the majority of FLR observations have
1109 been ground-based. The present section explores the same simulations discussed in
1110 Sections 7.1 to 7.4, but in terms of their ground signatures rather than their broad
1111 energy distributions.

1112 As in the figures shown in Sections 7.1 to 7.4, each row in Figures 7.10 and 7.11 shows
1113 runs at a different modenumber. The columns are magnetic field contours; the vertical
1114 axis is latitude, and the horizontal axis is time. The four columns are components of
1115 the magnetic field signatures at the ground: the north-south magnetic field (first and
1116 third columns) and the east-west magnetic field (second and fourth columns). The pair
1117 on the left show a simulation carried out using the active ionospheric profile, and the
1118 pair on the right show a simulation using the quiet profile.

1119 Notably, the magnetic polarization of a low frequency Alfvén wave is rotated by $\sim 90^\circ$ as
1120 it passes through the ionosphere[42]. The east-west field on the ground (B_ϕ) corresponds
1121 to the poloidal polarization in space, and the north-south field on the ground (B_θ)
1122 corresponds to the toroidal mode.

1123 **TODO:** What's going on with the empty frame for nightside, $m = 1, 16\text{ mHz}$?

1124 **TODO:** Don't use 19 mHz! It's wonky at low modenumber. Use 22 mHz instead.

1125 The most striking feature of Figures 7.10 and 7.11 is the modenumber dependence.
1126 As modenumber increases, the magnetic field signatures become sharply localized in
1127 latitude. At high m , ground signatures are concentrated between 60° and 70° , peaking
1128 just below 65° . This shows good agreement with observations of Pgs peaked near 66° .

1129 At low modenumber, magnetic signatures are weak on the ground because the waves
1130 in space are also weak. At high modenumber, waves in space are strong, but so is
1131 the attenuation of magnetic signatures by the ionosphere³. The “sweet spot” at which
1132 magnetic ground signatures are maximized falls at $m = 16$ to $m = 32$. For comparison,
1133 Pgs are generally observed with azimuthal modenumbers of 16 to 35[94].

³See Equation (3.2).

1134 Ground signatures are maximized at $m = 16$ and $m = 32$ on both the dayside (Figure
1135 7.10) and the nightside (Figure 7.11). Dayside signatures are stronger than those on
1136 the nightside, and quiet dayside and quiet nightside responses are stronger than those
1137 on the active dayside and active nightside respectively. The strongest magnetic fields
1138 at the ground are primarily east-west polarized – as Pgs are[94].

1139 TODO: At present, Tuna's ionospheric profiles do not allow the dawn and dusk flanks
1140 to be distinguished from the dayside and nightside.

Magnetic Ground Signatures: 19mHz Current , $L_{PP} = 4$, $L_{drive} = 5$

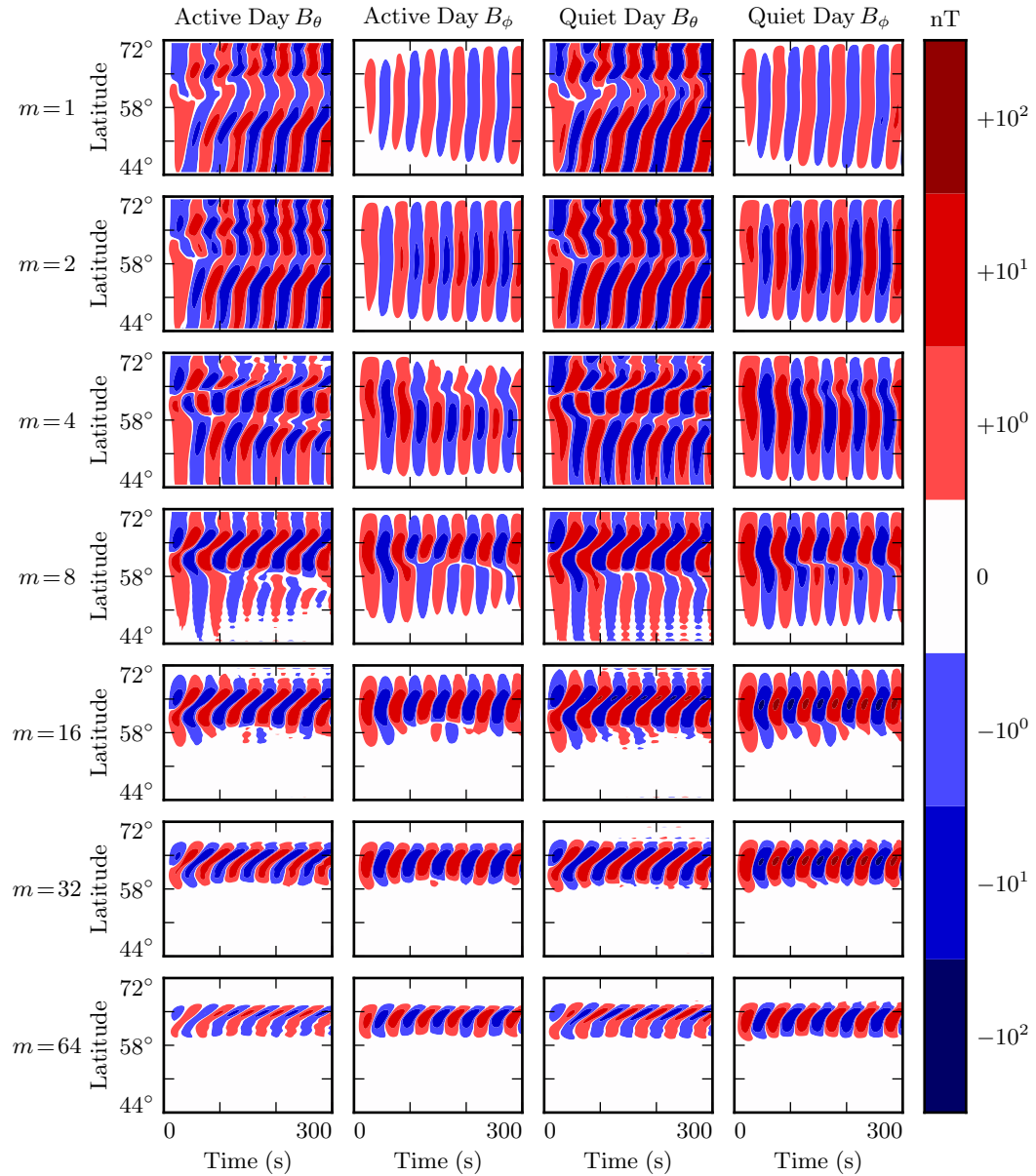


Figure 7.10: TODO: Use 22 mHz instead! At 19 mHz and low m , there's something weird happening at the outer boundary.

Magnetic Ground Signatures: 16mHz Current , $L_{PP} = 4$, $L_{drive} = 5$

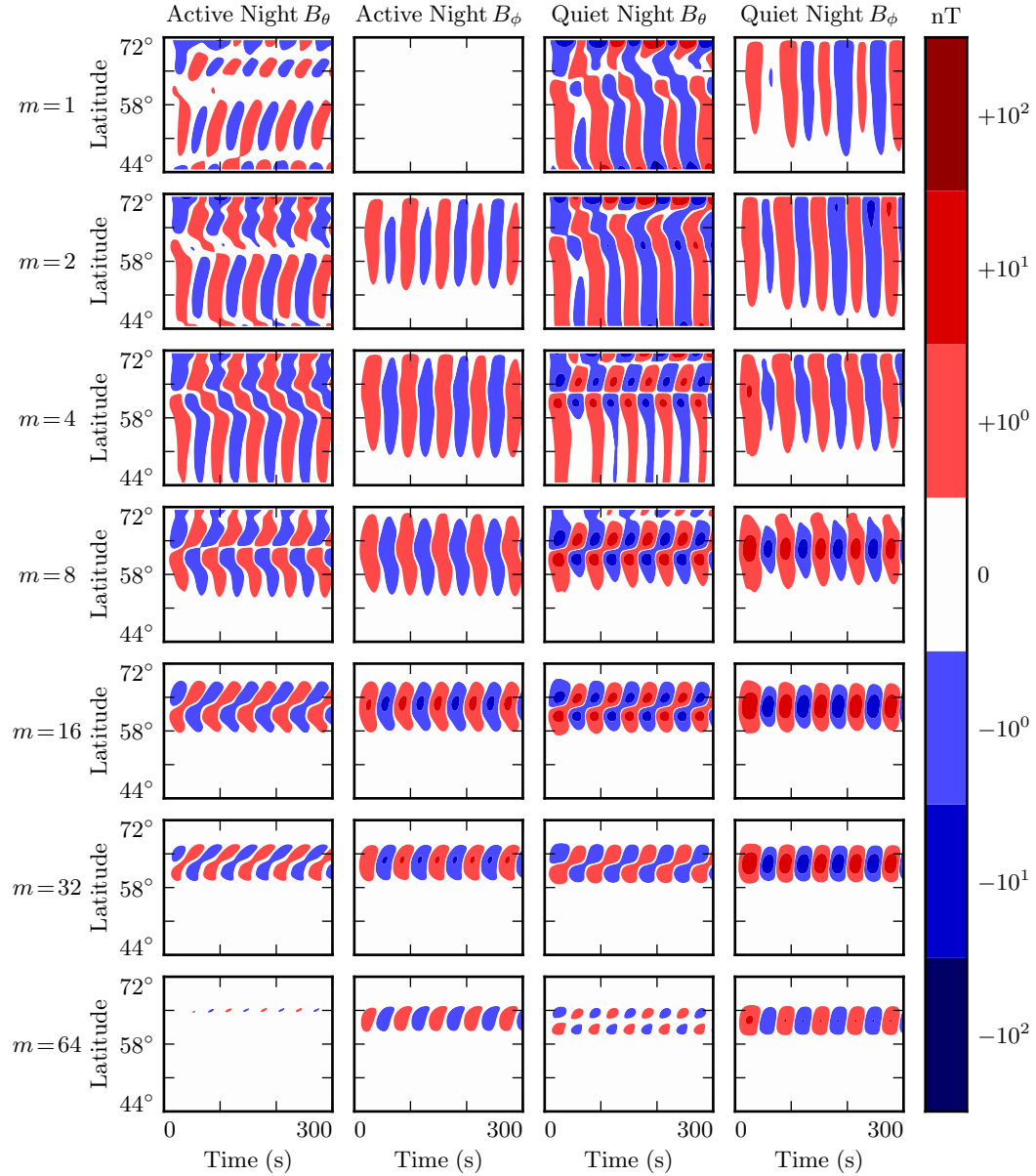


Figure 7.11: Nightside ground signatures are less strongly peaked than those on the dayside, but qualitative features are the same: the strongest signals are in B_ϕ , peaked over just a few degrees in latitude, at a modenumber of 16 or 32, under quiet ionospheric conditions.

1141 **7.6 Discussion**

1142 **TODO:** Make this section read nicely.

1143 Poloidal FLRs rotate to the toroidal mode over time. Toroidal modes do not appear to
1144 rotate back to the poloidal mode. When m is small, the rotation is comparable to an
1145 oscillation period; when m is large, rotation timescales are comparable to ten periods,
1146 sometimes more.

1147 On the dayside, little damping takes place over rotation timescales, so the toroidal mode
1148 asymptotically exceeds the toroidal mode. The exception is waves with low modenumber,
1149 where poloidal waves can escape by propagating across field lines. An evaluation
1150 of what happens then — whether they bounce back off the magnetopause, for example
1151 — is beyond the scope of the present work.

1152 On the nightside, the conductivity of the ionosphere is low enough that damping
1153 timescales become comparable to oscillation timescales. Waves are weaker, since they
1154 are unable to accumulate energy over as many periods. High- m toroidal waves are
1155 particularly weak, since the dissipation timescale is faster than the poloidal-to-toroidal
1156 rotation timescale.

1157 Waves resonate best when the frequency of the driving matches the local eigenfrequency
1158 where it's delivered. The eigenfrequency is significantly affected by the size of the
1159 plasmasphere.

1160 The poloidal mode, due to its compressional character, exhibits an energy profile which
1161 is smeared in L . The toroidal mode, on the other hand, forms sharp resonances where the
1162 drive frequency matches the local eigenfrequency. This may explain why the observed
1163 frequencies of poloidal waves depend weakly on L , while the frequencies of toroidal
1164 waves are strongly dependent on L .

1165 At low m , ground signatures are weak because waves in space are weak because energy
1166 can easily escape through the simulation's outer boundary. At large m , ground signatures
1167 are attenuated by the ionosphere. The “sweet spot” in azimuthal modenumber at
1168 which ground signatures are strongest is around 16 to 32. Furthermore, ground signatures
1169 are strongest when ionospheric profiles corresponding to solar minimum are used.

1170 Driving in the poloidal electric field gives rise to primarily ground signatures polarized
1171 primarily in the east-west direction at the ground. And, when the frequency of the
1172 driving does not match the local eigenfrequency, the high- m resonates weakly in place,
1173 rather than tunneling across field lines to resonate strongly somewhere else.

1174 These findings imply, awkwardly, that the morphology of giant pulsations may reveal
1175 relatively little about their origins. One can consider a hypothetical magnetosphere
1176 subject to constant driving: broadband in frequency, broadband in modenumber, just
1177 outside the plasmapause. Low- m poloidal waves will quickly rotate to the toroidal mode
1178 (and/or propagate away). High- m waves will resonate in place, accumulating energy
1179 over time, and giving rise to “multiharmonic toroidal waves”[91]; Fourier components
1180 that do not match the local eigenfrequency will quickly asymptote. Waves with very high
1181 modenumbers will be attenuated by the ionosphere. The response on the ground will be
1182 significantly stronger during quiet solar conditions. In other words, the measurements
1183 on the ground will look very much like a giant pulsation.

1184 **TODO:** Notably, the present work offers no explanation as to Pgs’ distinctive distribu-
1185 tion in MLT!

1186 **Chapter 8**

1187 **Observations**

1188 TODO: You know what would be great for putting this numerical work in context?

1189 A nice, consistent survey that breaks down the occurrence rate of Pc4 pulsations by
1190 harmonic, etc.

1191 TODO: Anderson[3] located events by visual inspection of AMPTE/CCE data. He
1192 found that toroidal resonances outnumber poloidal ones about three-to-one. “Harmonic
1193 toroidal resonances” are spread 0600 to 1600. “Fundamental toroidal resonances” (which
1194 are not mutually exclusive with harmonic ones!) appear everywhere but dusk. Poloidal
1195 modes occur everywhere but dawn; odd and even harmonics are not distinguished.
1196 Notably, most observation time was spent at $L > 7$. Orbit near the equator, magnetic
1197 field instrumentation, so fundamental poloidal modes would have been hard to observe...
1198 and I need to reread this to figure out how he managed to observe fundamental toroidal
1199 modes!

1200 TODO: Dai[17] found 890 poloidal Pc4 events using RBSP. Due to a cutoff in magnetic
1201 field amplitude, his findings are biased in favor of the even mode. Events are shown to
1202 be most common near noon, but smeared across the dayside, and with a few stragglers
1203 near midnight. Low- m waves were shown to be smeared a bit more, occurring across
1204 the entire dusk flank at low rates.

1205 TODO: Motoba[72] looked specifically at Pgs – 105 events. Seen from midnight to noon,
1206 with a strong peak before dawn, 0300 or so. Events are identified by visual inspection.
1207
1208 TODO: Probably need some fluff here with appropriate citations for RBSP and its
1209 instrumentation.
1210 TODO: The tools used in the present chapter — SPEDAS and the SPICE kernel —
1211 are publicly available. They run best with an IDL license, which is not, but they are
1212 functional using just the (free) IDL virtual machine. The code is wrapped up in a Git
1213 repository: <https://github.com/chizarlicious/RBSP> (maybe should make a GitHub
1214 organization to hold this code, to decouple it from my personal account?).

1215 8.1 Sampling Bias and Event Selection

1216 The present analysis makes use of as much Van Allen Probe data as is available at the
1217 time of writing: October 2012 to August 2015. Between the two probes, that's just over
1218 2000 days of observation.
1219 Notably, the two probes are taken to be independent observers. The vast majority
1220 of Pc4 observations take place near apogee, where the probes are separated by several
1221 hours. Pc4 pulsations tend to be localized in MLT — indeed, this was a key justification
1222 for the model described in Chapter 5. The two probes simultaneously observe the same
1223 event only TODO: … of the time.
1224 TODO: How common is it for one probe to see an event, then the other probe to fly
1225 through that same event an hour or two later?
1226 Electric and magnetic waveform data is cleaned up by averaging over the probe's spin
1227 period, 10.5 s. The three-dimensional electric field is then obtained using the assumption
1228 $\underline{E} \cdot \underline{B} = 0$. Notably, this assumption is taken only when the probe's spin plane is offset
1229 from the magnetic field by at least 15° . The rest of the data — about half — is discarded,
1230 which introduces a sampling bias against the flanks.

1231 A further bias is introduced by the probes' non-integer number of precessions around
1232 Earth. Pc4 pulsations are most commonly observed near apogee. As of July 2014,
1233 apogee had precessed once around Earth[17]. The present work considers roughly one
1234 and a half precessions; the nightside has been sampled at apogee twice as often as the
1235 dayside.

1236 The spatial distribution of usable data — that is, data for which three-dimensional
1237 electric and magnetic fields are available — is shown in Figure 8.1. Bins are unitary in
1238 L (divided at integer L) and in MLT (centered at integer hours). Event distribution in
1239 magnetic latitude is not shown; the Van Allen Probes are localized to within **TODO:**
1240 15° of the equatorial plane.

1241 **TODO:** *L* is italicized and MLT is not? That seems weird.

1242 Awkwardly, coverage is weakest from pre-dawn to the mid-afternoon — the exact regions
1243 where Pc4 pulsations have been shown to peak. In order to compensate for that fact,
1244 results in the present chapter are binned coarsely. Histogram bins are two hours wide
1245 in MLT. Only two bins are used in the radial direction: $L \leq 5$ and $L > 5$.

1246 **TODO:** Most events occur between $L = 4$ and $L = 6$, but splitting at $L = 5$ is otherwise
1247 arbitrary. It might make more sense to split the bins wherever the median event is or
1248 something.

1249 Field measurements are transformed from GSE coordinates into the same dipole coor-
1250 dinates used in Chapters 5 and 7. The z axis is parallel to the background magnetic
1251 field, which is estimated using a ten-minute running average of the magnetic field mea-
1252 surements. The y axis is defined per $\hat{y} \parallel \hat{z} \times \underline{r}$. The x axis is then defined per $\hat{x} \equiv \hat{y} \times \hat{z}$.
1253 This method is described by Liu[58], and guarantees that the axes are right-handed and
1254 pairwise orthogonal.

1255 The \sim 1000 days of usable data are considered half an hour at a time — \sim 60 data points
1256 per event at the ten-second spinfit cadence. This allows for a frequency resolution of
1257 \sim 0.5 mHz in the discrete Fourier transform. Spectra are computed for all six field
1258 components: \tilde{B}_x , \tilde{B}_y , \tilde{B}_z , \tilde{E}_x , \tilde{E}_y , and \tilde{E}_z .

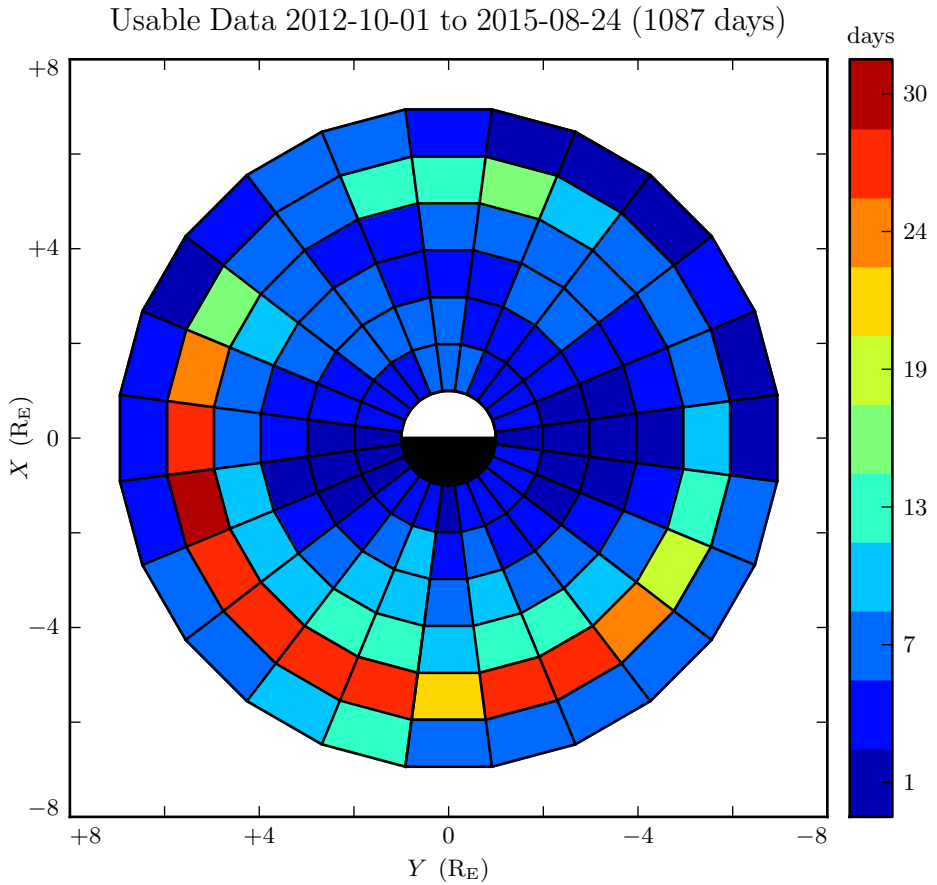


Figure 8.1: Three-dimensional electric field values are computed by assuming $\underline{E} \cdot \underline{B} = 0$. Data is discarded whenever the magnetic field falls within 15° of the spin plane, which introduces a bias against the flanks. Furthermore, the probes have completed only one and a half precessions around Earth; the dayside has been sampled once at apogee, and the nightside twice.

1259 The background magnetic is subtracted off before performing each transform, leaving
 1260 only the magnetic field perturbation along each axis. (As in Chapters 5 and 7, B_x
 1261 refers not to the full magnetic field in the x direction, but to its perturbation from the
 1262 zeroth-order field.) Each waveform is also shifted horizontally so that its mean over the
 1263 thirty minute event is zero.

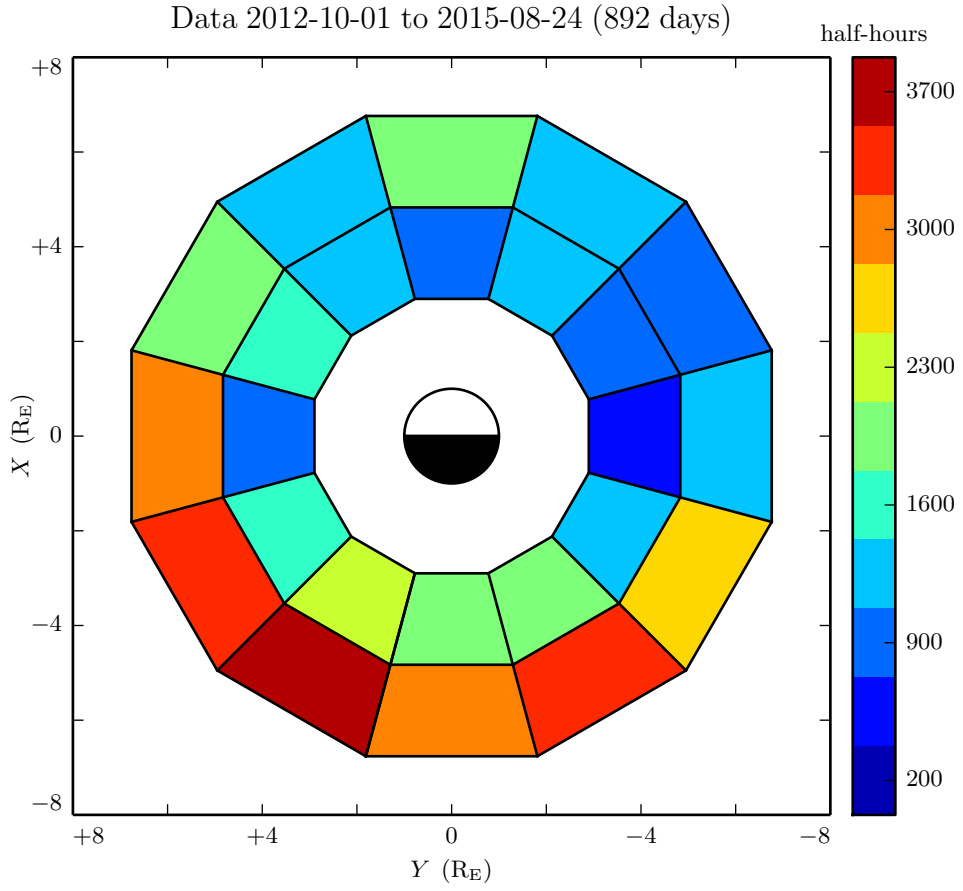


Figure 8.2: **TODO:** This is the sampling distribution used to normalize Dst-agnostic event counts. It's not clear that all of these plots are necessary.

Frequency-domain Poynting flux is computed from the electric and magnetic field transforms. Values are effective at the ionosphere; a factor of L^3 is introduced to account for the compression of the flux tube. Poloidal and toroidal Poynting flux, respectively, are given by:

$$\tilde{S}_P \equiv -\frac{L^3}{\mu_0} \tilde{E}_y \tilde{B}_x^* \quad \tilde{S}_T \equiv \frac{L^3}{\mu_0} \tilde{E}_x \tilde{B}_y^* \quad (8.1)$$

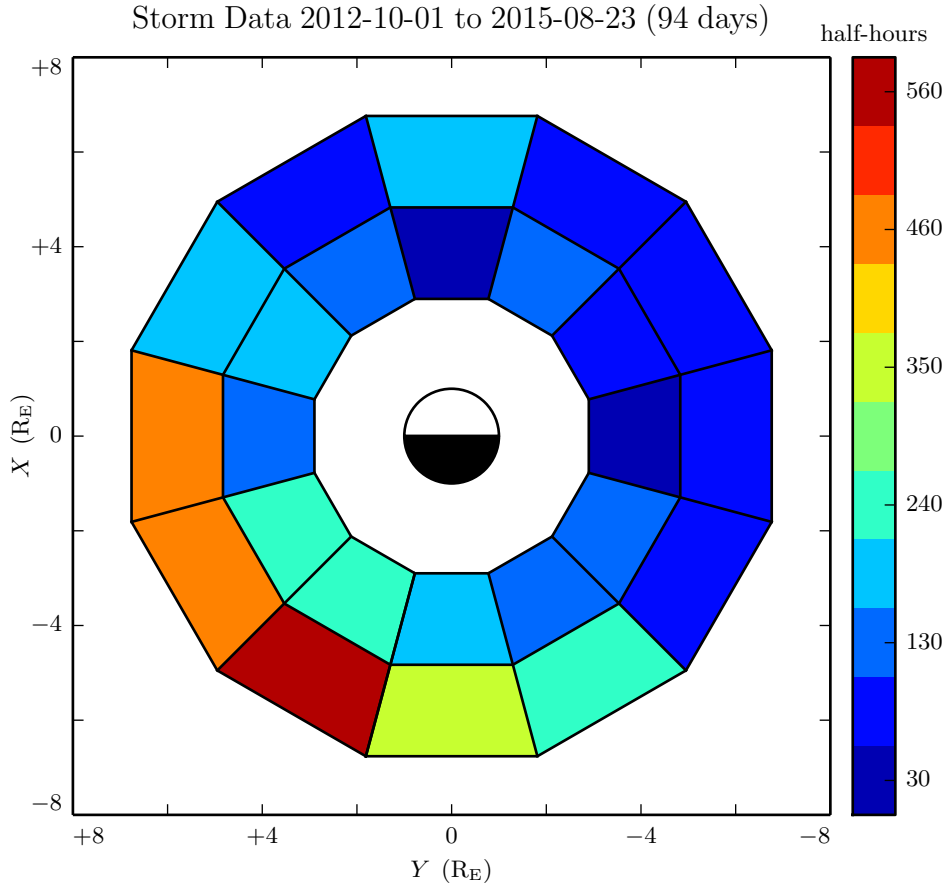


Figure 8.3: TODO: This is the sampling distribution used to normalize event counts at $Dst \geq -30$ nT. It's not clear that all of these plots are necessary.

1264 TODO: The Poynting flux scaled by L^3 to conserve energy. But doesn't the magnetic
 1265 field be scale with L^3 to conserve flux, and the electric field scale with the magnetic
 1266 field?

1267 The Poynting fluxes \tilde{S} for each event are filtered based on frequency, magnitude, and
 1268 phase offset. The poloidal and toroidal channels are checked independently; a given half
 1269 hour can have no event, a poloidal event, a toroidal event, or both.

1270 A Gaussian profile is fit to $|\text{Im}\tilde{S}|$, which corresponds to the magnitude of the standing
 1271 wave (in turn, the real component is the traveling wave). If the fit fails, for example due

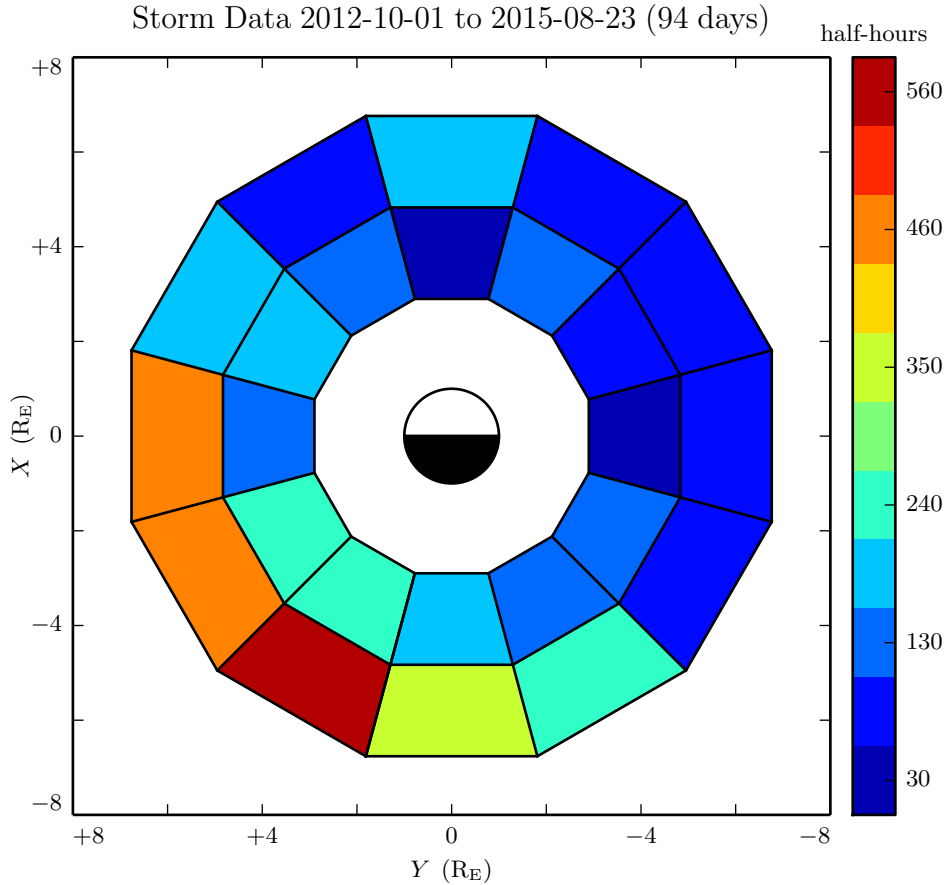


Figure 8.4: **TODO:** This is the sampling distribution used to normalize event counts at $\text{Dst} < -30 \text{ nT}$. It's not clear that all of these plots are necessary.

- 1272 to non-finite values in the data, the event is discarded. The event is also discarded if
- 1273 the peak of the Gaussian does not correspond to the largest spectral feature in the data,
- 1274 standing or traveling; that is, the event is disqualified if the Gaussian is not centered
- 1275 within 5 mHz of the maximum value of $|\tilde{S}|$.
- 1276 Non-Pc4 events are filtered out: any event for which the standing wave Gaussian does
- 1277 not fall in the range 7 mHz to 25 mHz. Notably, no filter is imposed on spectral width.
- 1278 Out of consideration for instrument sensitivity, events are thresholded at a magnitude
- 1279 of $|\text{Im}\tilde{S}| \geq 10^{-2} \text{ mW/m}^2$.

1280 Events are filtered based on the phase offset between the electric and magnetic field
1281 waveforms, given by $\arctan \frac{\text{Im} \tilde{S}}{\text{Re} \tilde{S}}$. For a purely traveling wave, the electric and magnetic
1282 field waveforms are in phase (0°) or in antiphase (180°). Standing waves have a phase
1283 of $\pm 90^\circ$ between their electric and magnetic field components. The events presented
1284 here are filtered conservatively in phase; the standing wave must just barely exceed the
1285 traveling wave (phase between 45° and 135° in absolute value).

1286 **TODO:** A stricter cutoff in magnitude, or in phase, does not obviously affect the dis-
1287 tributions of events... it just shrinks the sample size and makes everything look noisier.

1288

1289 Events are filtered on coherence, to ensure that the phase offset is credible. If the
1290 coherence between \tilde{E} and \tilde{B}^* is less than 0.9, the event is discarded. Coherence and
1291 phase are both measured at the discrete Fourier transform point closest to the peak of
1292 the Gaussian.

1293 Finally, any event within 3° of the magnetic equator is discarded due to ambiguity in
1294 its phase. As discussed in Chapter 3, odd and even harmonics are distinguished by the
1295 sign of the phase offset between the electric and magnetic field. For example, in odd
1296 poloidal modes, an observer north of the equator sees B_x lead E_y by a phase of 90° ,
1297 and an observer below the equator sees the opposite. When the probe is very close to
1298 the equator, an event's parity becomes ambiguous.

1299 **TODO:** We try not to worry too much about first vs third harmonic, since we can't tell
1300 them apart except by guessing at frequency. Chisham and Orr[14] argue that around
1301 $7 R_E$, frequency around 10 mHz precludes higher harmonics. Or maybe look at [35]?

1302 **8.2 Overall Rate of Pc4 Events**

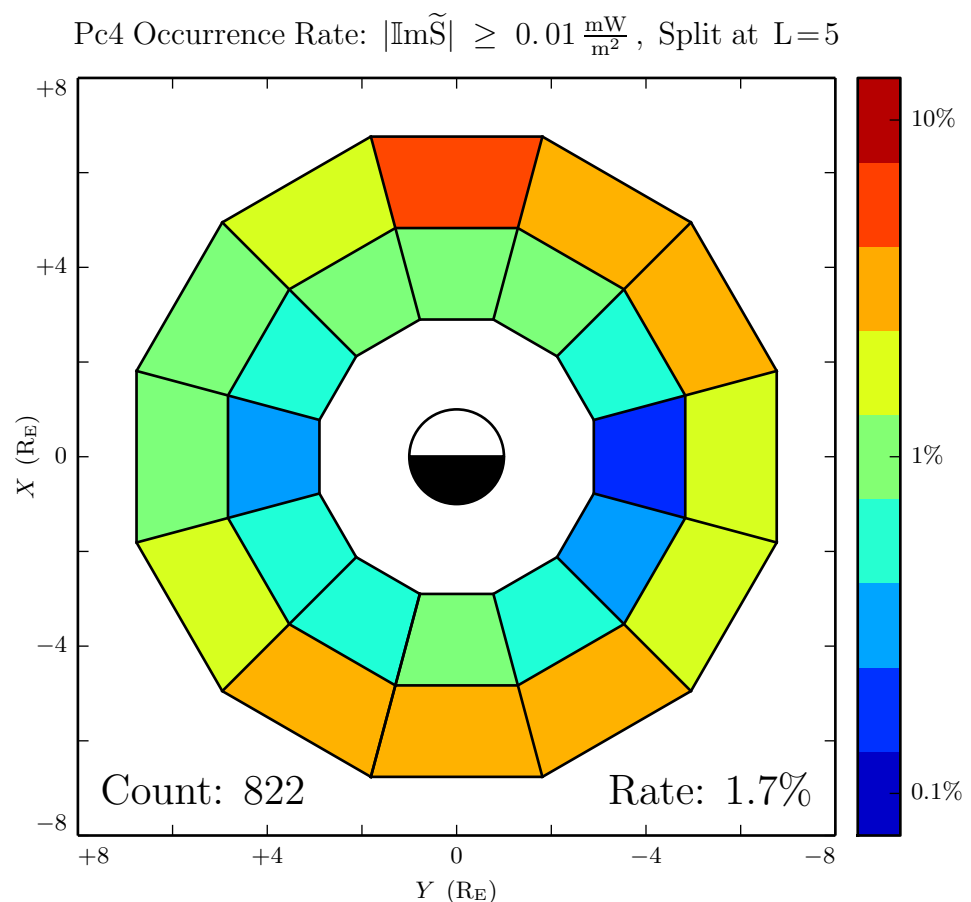


Figure 8.5: TODO: Pc4s are observed at all local times, but are most common near noon and least common near dusk.

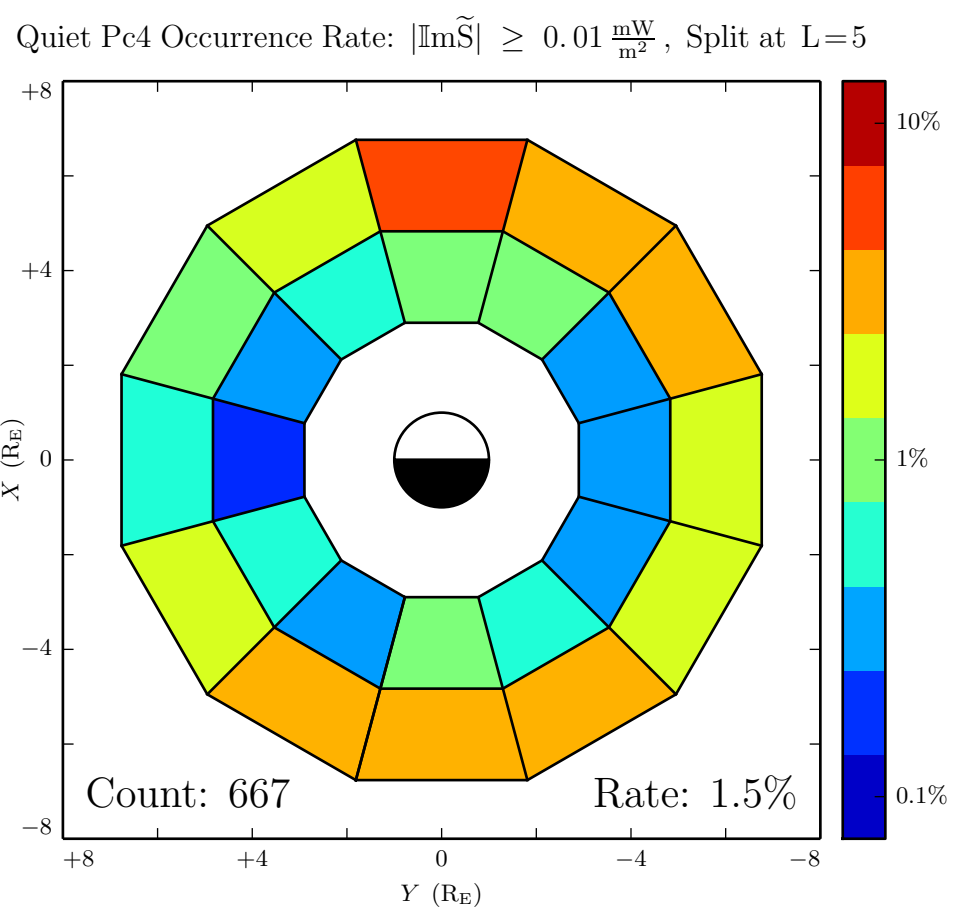


Figure 8.6: **TODO:** ...

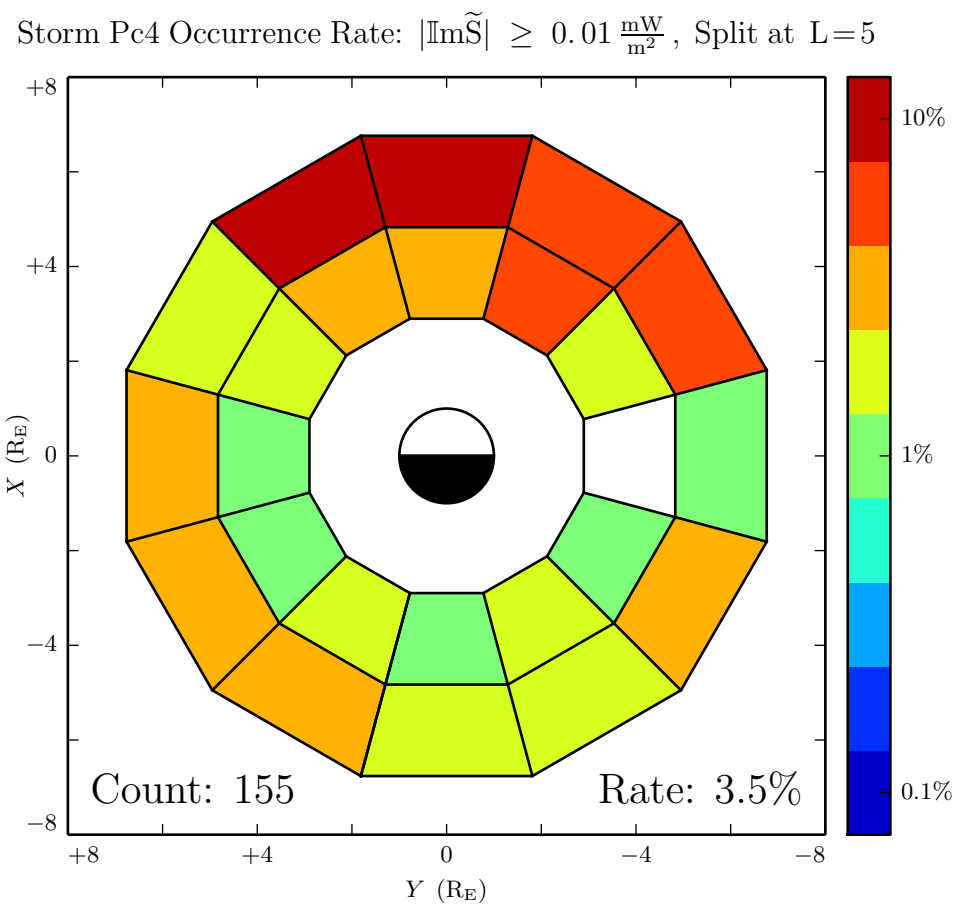


Figure 8.7: TODO: During geomagnetically active times, Pc4 pulsations become significantly more common, particularly near noon.

1303 **8.3 Pc4 Events by Mode**

1304 The filters described in Section 8.1 yield 822 events: 136 odd poloidal modes, 234 even
1305 poloidal modes, 445 odd toroidal modes, and 86 even toroidal modes. The distributions
1306 of those events are shown in Figures 8.8 and 8.10; counts are normalized to the sampling
1307 rates shown in Figures 8.2 and 8.4 respectively.

1308 TODO: It's good to see that even poloidal modes and even toroidal modes are dis-
1309 tributed similarly, since one turns into the other! The relationship is less clear for odd
1310 modes, though odd poloidal modes and odd toroidal modes are both least common at
1311 dusk.

1312 TODO: Odd toroidal events are by far the most commonly observed.

1313 TODO: Even modes are less likely to be observed on the ground? [94]

Pc4 Occurrence Rate by Mode: $|\text{Im}\tilde{S}| \geq 0.01 \frac{\text{mW}}{\text{m}^2}$, Split at L=5

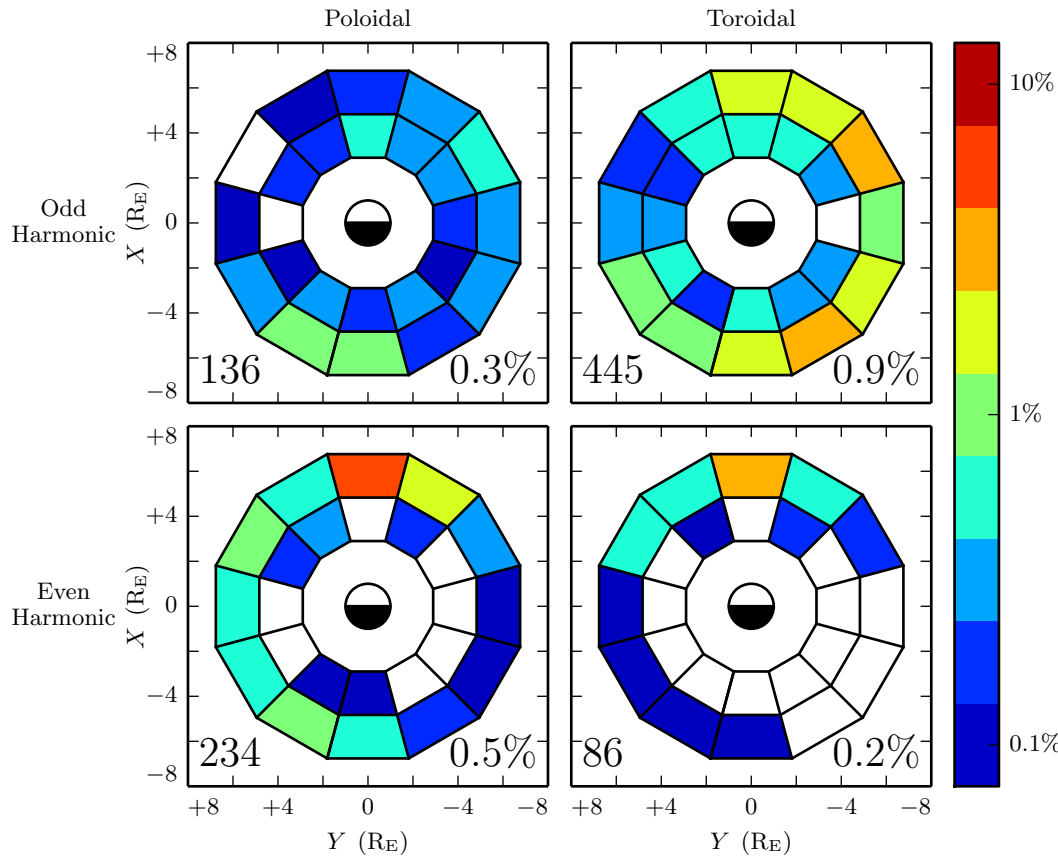


Figure 8.8: TODO: Even harmonics are strongly peaked at noon, with some presence smeared across the dusk side. Odd harmonics, on the other hand, are mostly seen on the dawn side.

Quiet Pc4 Occurrence Rate by Mode: $|\text{Im}\tilde{S}| \geq 0.01 \frac{\text{mW}}{\text{m}^2}$, Split at $L=5$

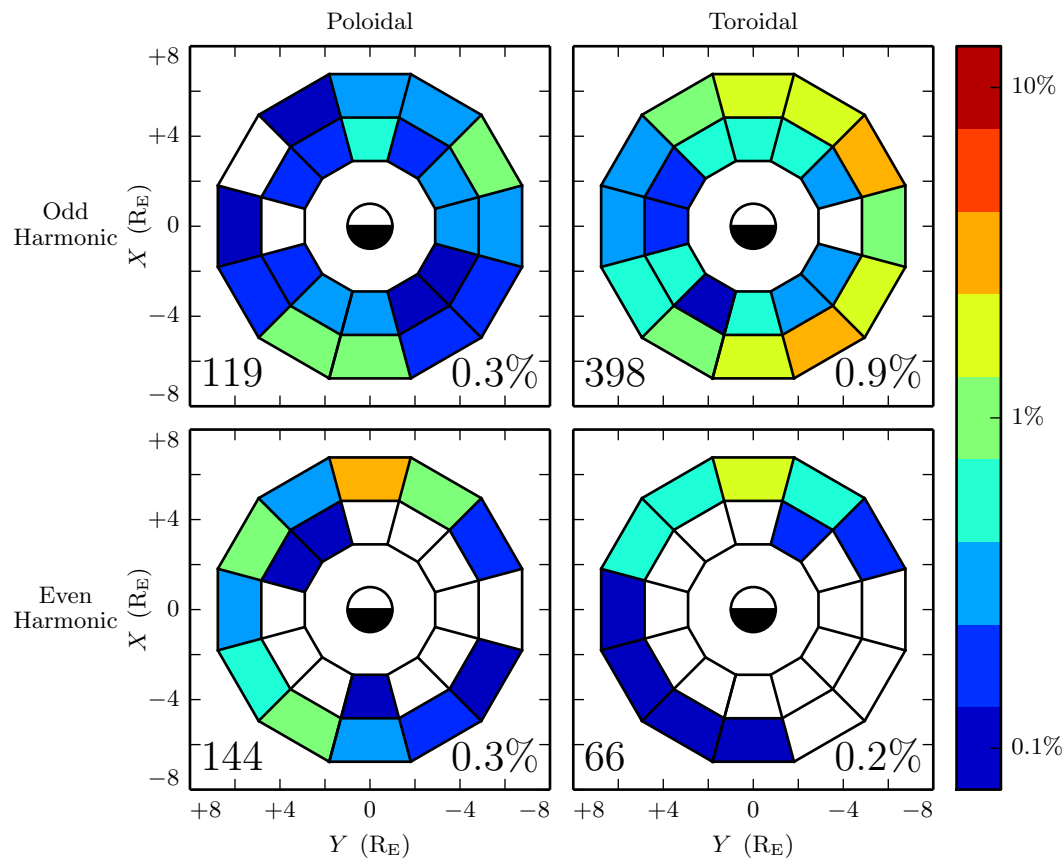


Figure 8.9: **TODO:** ...

Storm Pc4 Occurrence Rate by Mode: $|\text{Im}\tilde{S}| \geq 0.01 \frac{\text{mW}}{\text{m}^2}$, Split at $L=5$

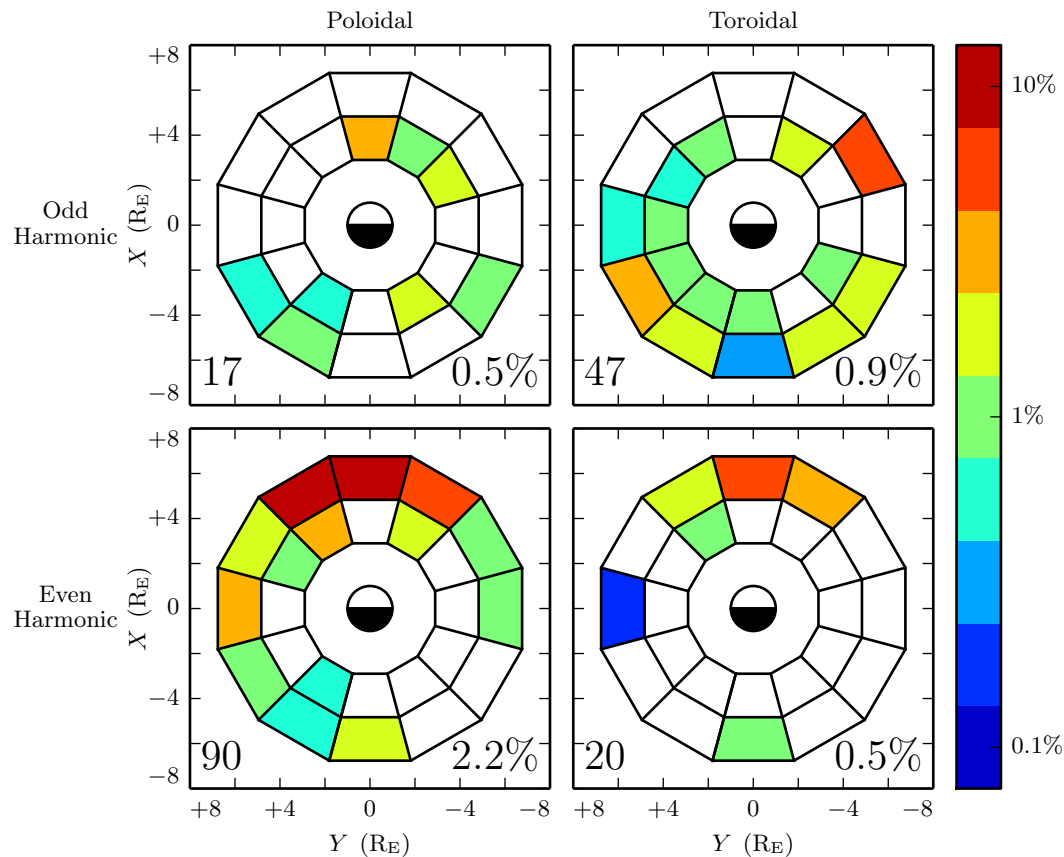


Figure 8.10: TODO: Pc4 events near noon are much more common during geomagnetically active times.

1314 8.4 Pc4 Events Inside and Outside the Plasmapause

1315 TODO: In the present section, bins in the radial direction indicate whether the event
1316 is located inside or outside of the plasmapause. Plasmapause locations are estimated
1317 from work by Scott. Normalization is also computed based on the sampling rate inside
1318 and outside the plasmapause.

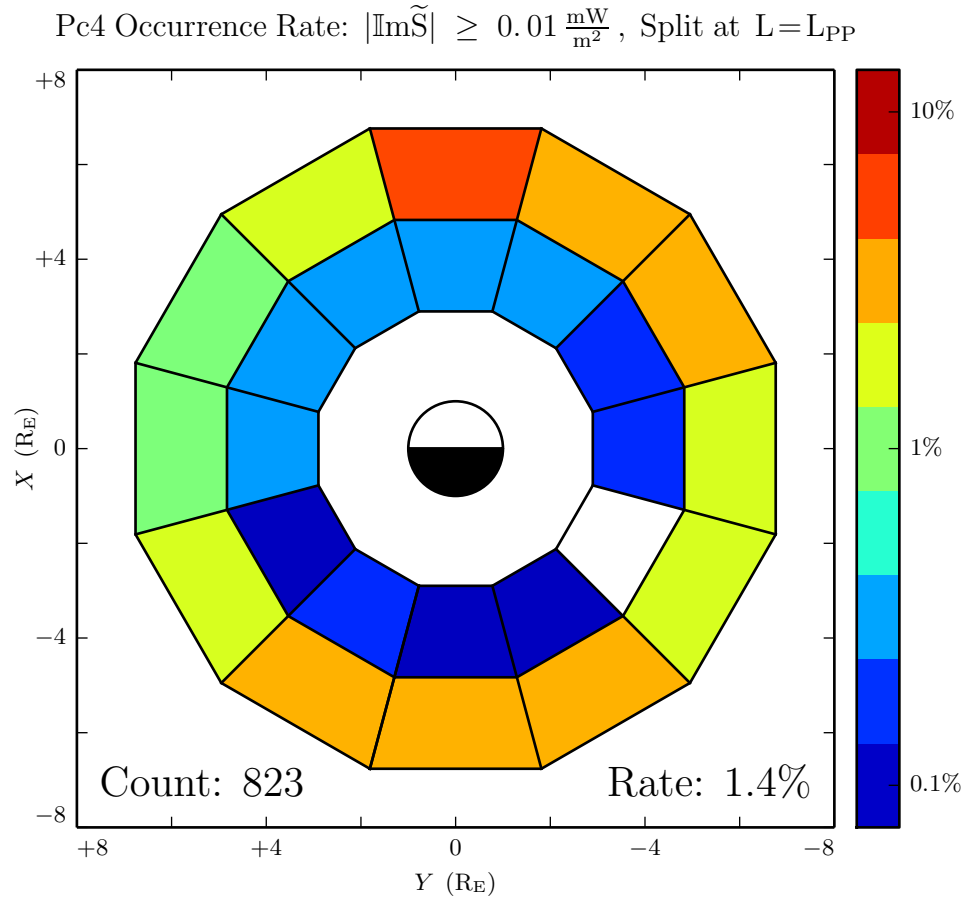


Figure 8.11: TODO: Pc4 events are usually outside the plasmapause.

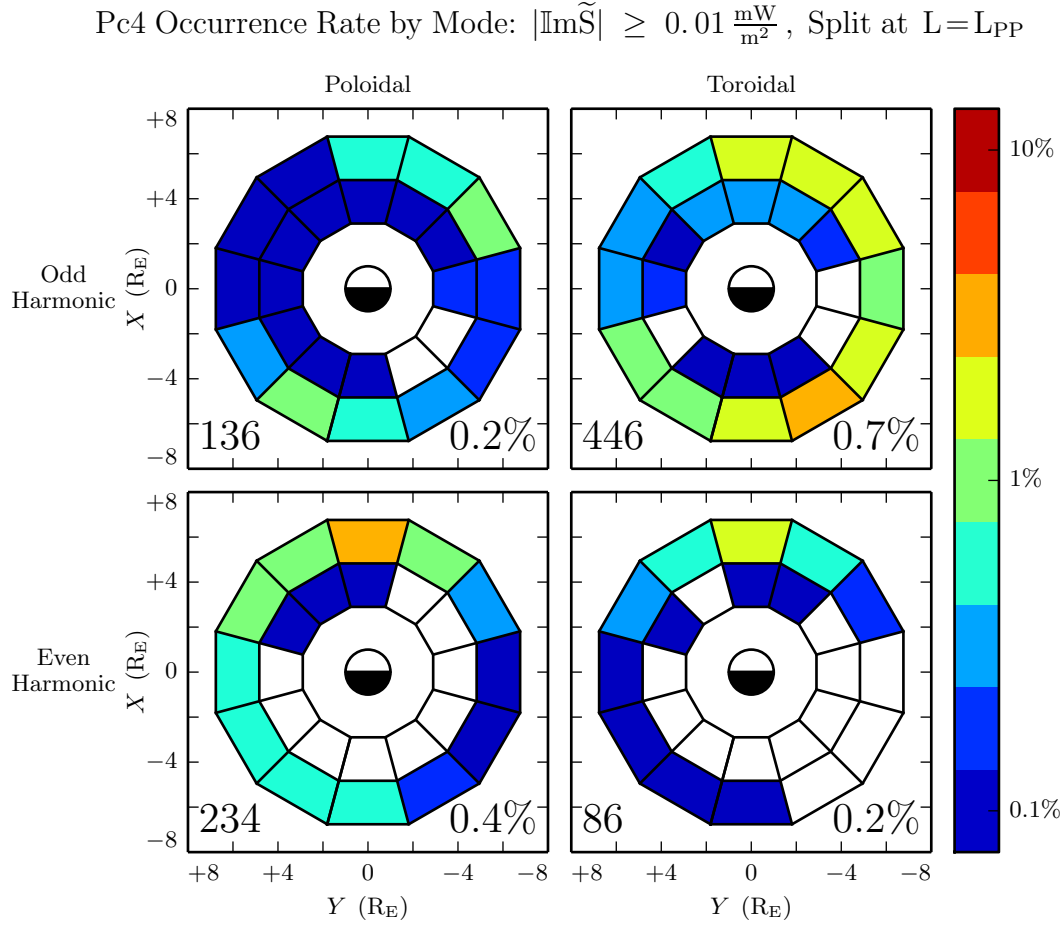


Figure 8.12: TODO: Odd events are sometimes inside the plasmapause. Even events are almost never inside the plasmapause.

1319 8.5 Poloidal Pc4 Events by Compressional Coupling

1320 TODO: Low- m poloidal Pc4 events are coupled to the compressional mode, while high-
1321 m ones are not.

1322 TODO: The value of $\tilde{B}_z/\tilde{B}_x = 0.2$ comes from Dai[17]. Can we match this up to an m
1323 value? Sounds like a job for Tuna!

Poloidal Pc4 by Compressional Coupling: $|\text{Im}\tilde{\mathbf{S}}| \geq 0.01 \frac{\text{mW}}{\text{m}^2}$, Split at $L=5$

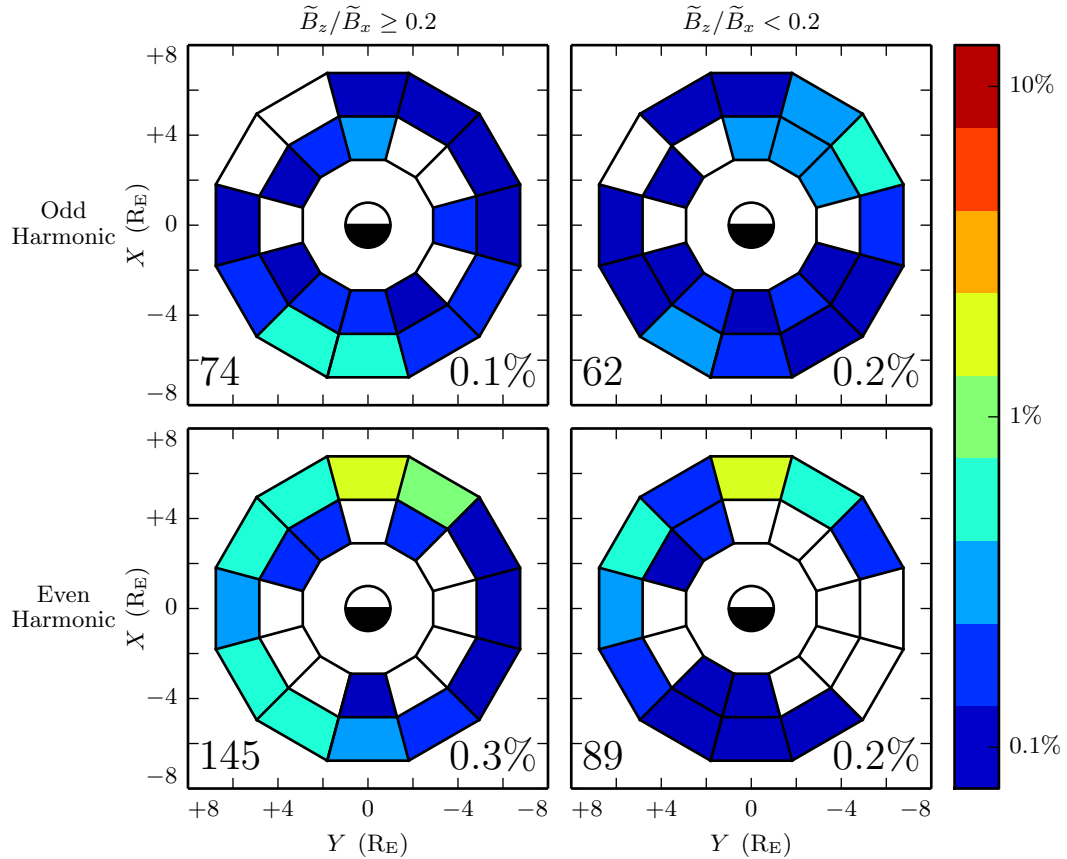


Figure 8.13: TODO: Odd poloidal Pc4 events have a peak pre-noon and another peak near midnight. The pre-noon peak seems to be composed of high- m events, and the midnight peak seems to be low- m events. Low- m even poloidal events are spread broadly across the dusk side, while high- m even events are peaked strongly on the dayside — consistent with Dai's results[17].

Quiet Poloidal Pc4 by Compressional Coupling: $|\text{Im}\tilde{\mathbf{S}}| \geq 0.01 \frac{\text{mW}}{\text{m}^2}$, Split at $L = \xi$

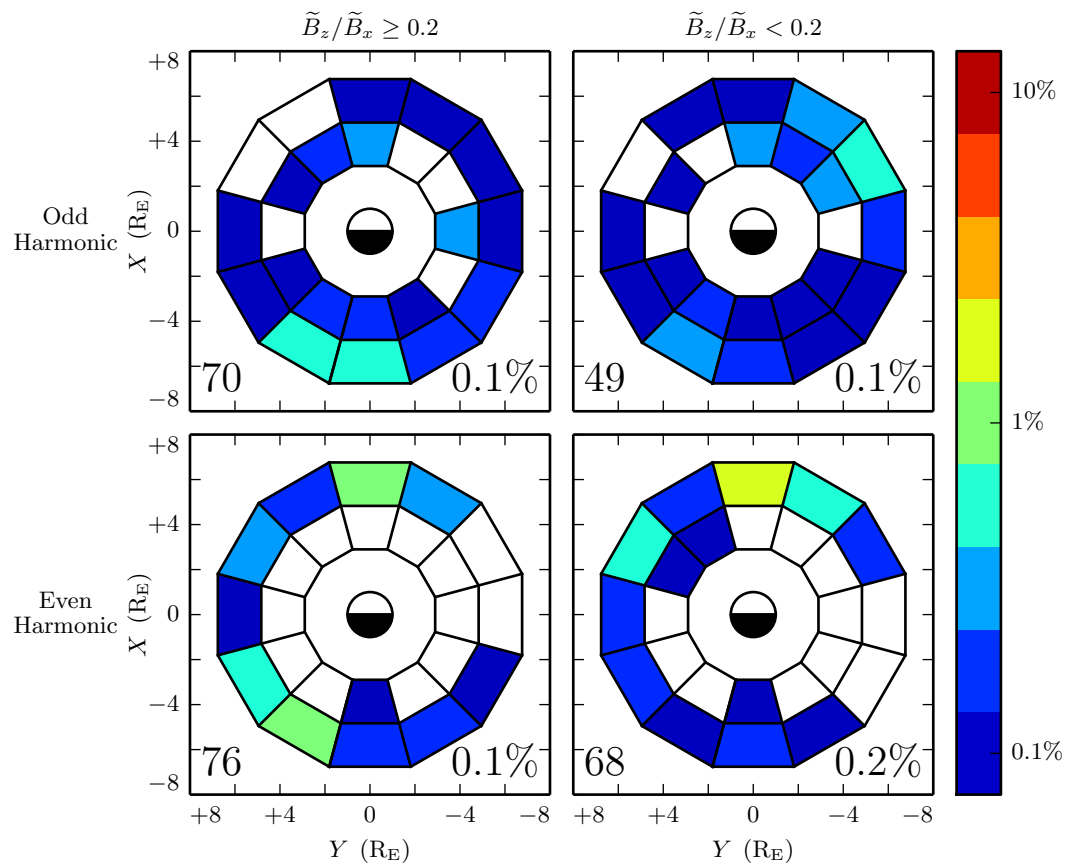


Figure 8.14: TODO: Looks about like Figure 8.13...

Storm Poloidal Pc4 by Compressional Coupling: $|\text{Im}\tilde{S}| \geq 0.01 \frac{\text{mW}}{\text{m}^2}$, Split at $L=5$

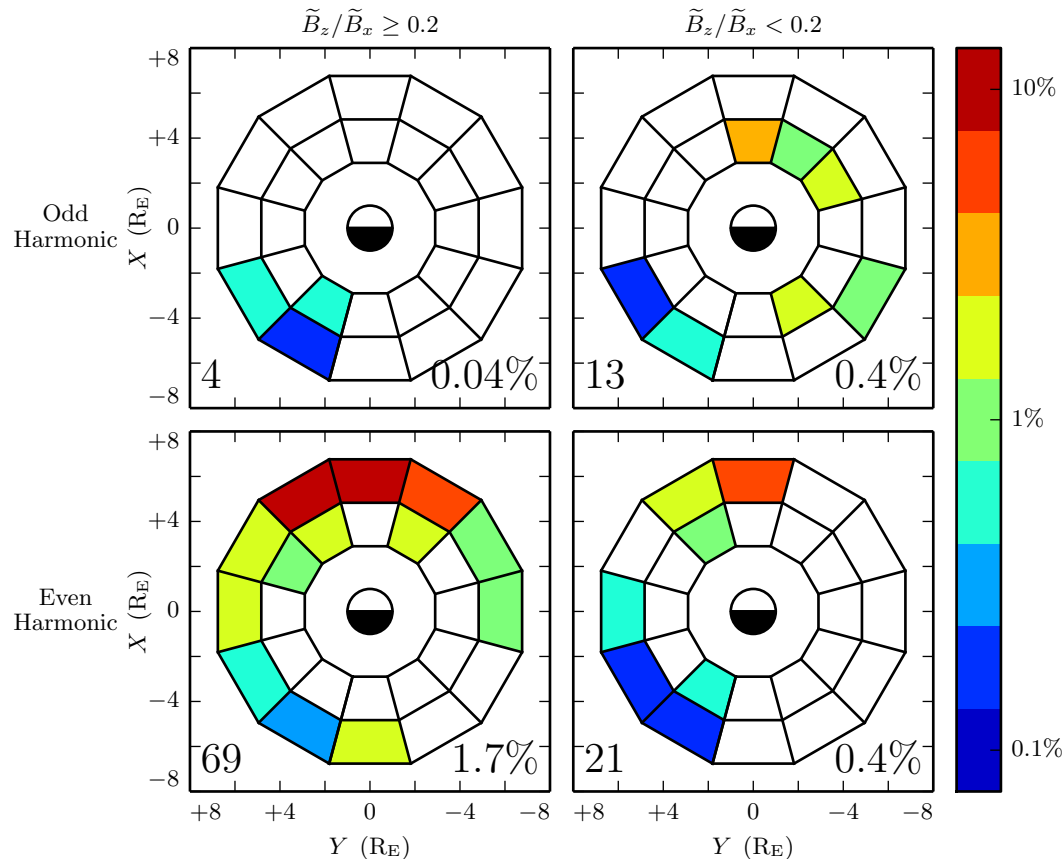


Figure 8.15: TODO: During storm-time, the rate of high- m poloidal modes goes up for both odd and even modes. The rate of low- m even modes goes WAY up. And the rate of low- m odd modes goes down!

1324 **8.6 Pc4 Events by Spectral Width**

1325 TODO: We did a Gaussian fit of each spectrum as part of the event selection process.
 1326 That gives FWHM. Let's divide the events at a FWHM of 1.3 mHz, the (rounded)
 1327 median value.

Poloidal Pc4 by Spectral Width: $|\text{Im}\tilde{S}| \geq 0.01 \frac{\text{mW}}{\text{m}^2}$, Split at L=5

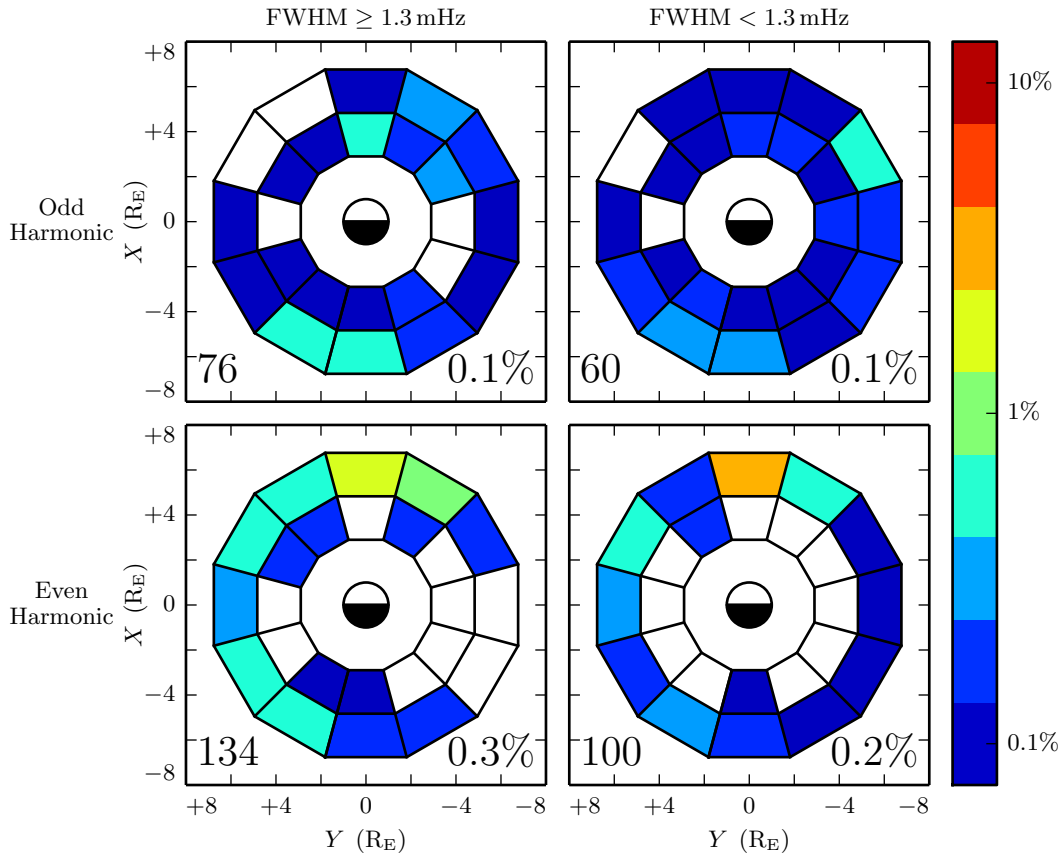


Figure 8.16: TODO: Odd poloidal events skew a bit toward midnight when the spectra are broad/messy. Even poloidal modes skew significantly duskward — or, maybe, nice clean peaks are particularly common near noon.

Quiet Poloidal Pc4 by Spectral Width: $|\text{Im}\tilde{S}| \geq 0.01 \frac{\text{mW}}{\text{m}^2}$, Split at $L=5$

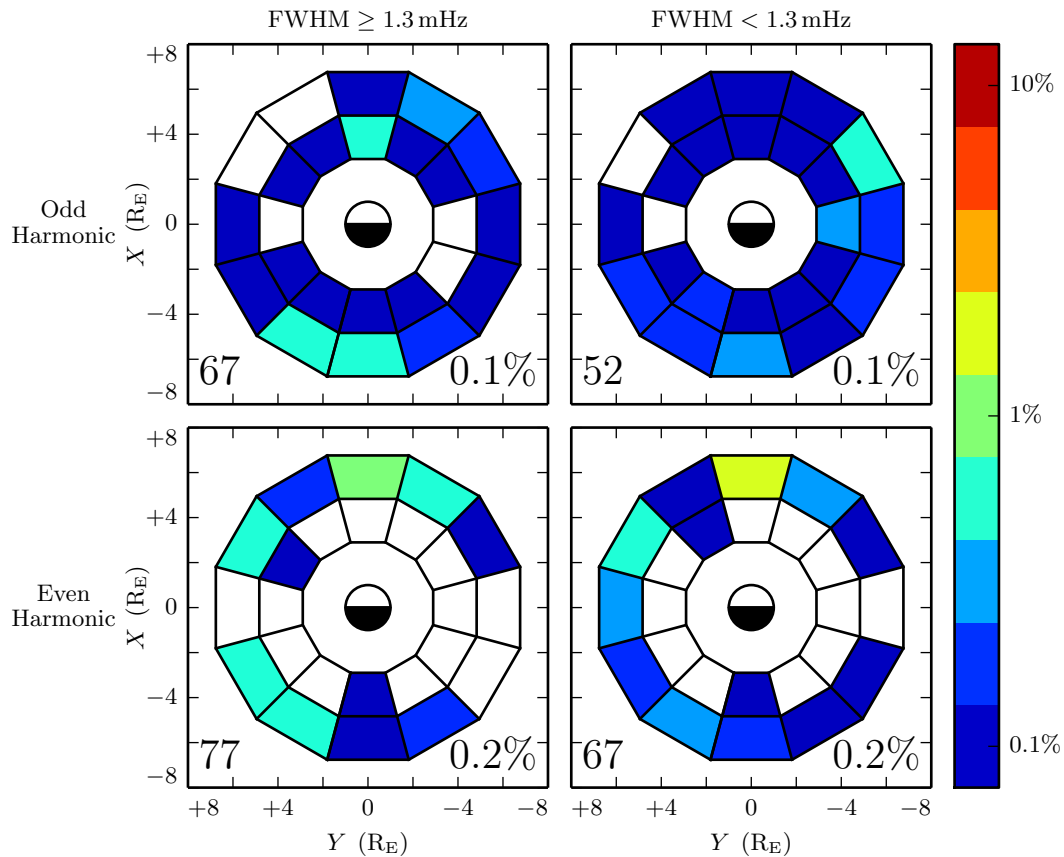


Figure 8.17: TODO: Looks about like Figure 8.16...

Storm Poloidal Pc4 by Spectral Width: $|Im\tilde{S}| \geq 0.01 \frac{mW}{m^2}$, Split at $L=5$

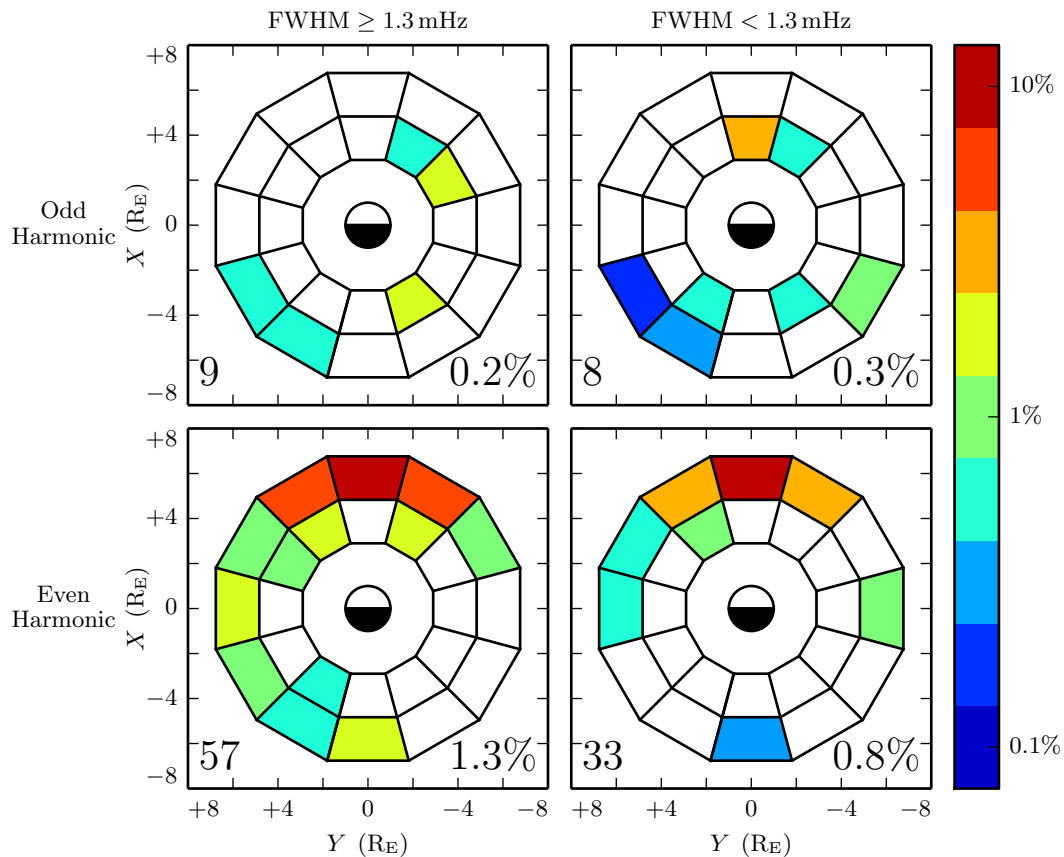


Figure 8.18: TODO: Even poloidal events skew toward broad/messy spectra during storm time, compared to the quiet time distribution of FWHM.

Toroidal Pc4 by Spectral Width: $|\text{Im}\tilde{S}| \geq 0.01 \frac{\text{mW}}{\text{m}^2}$, Split at L=5

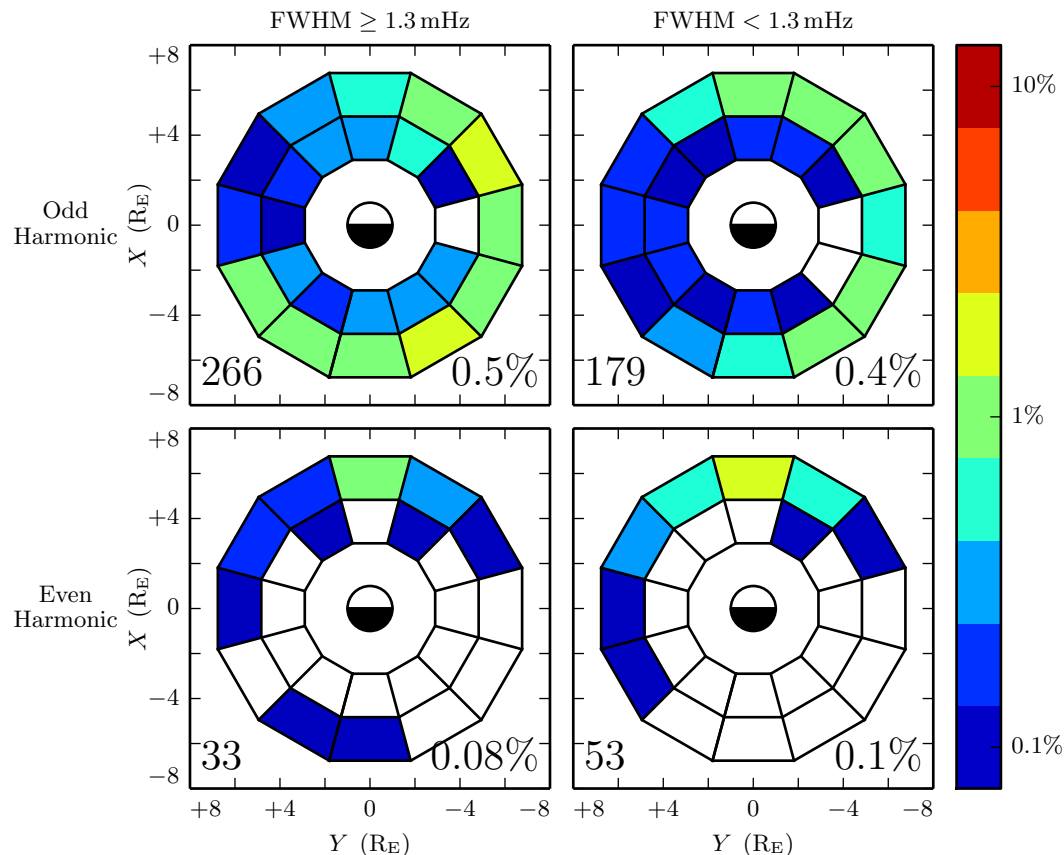


Figure 8.19: TODO: Odd toroidal modes are skewed overall toward broad/messy spectra.

Quiet Toroidal Pc4 by Spectral Width: $|\text{Im}\tilde{S}| \geq 0.01 \frac{\text{mW}}{\text{m}^2}$, Split at $L=5$

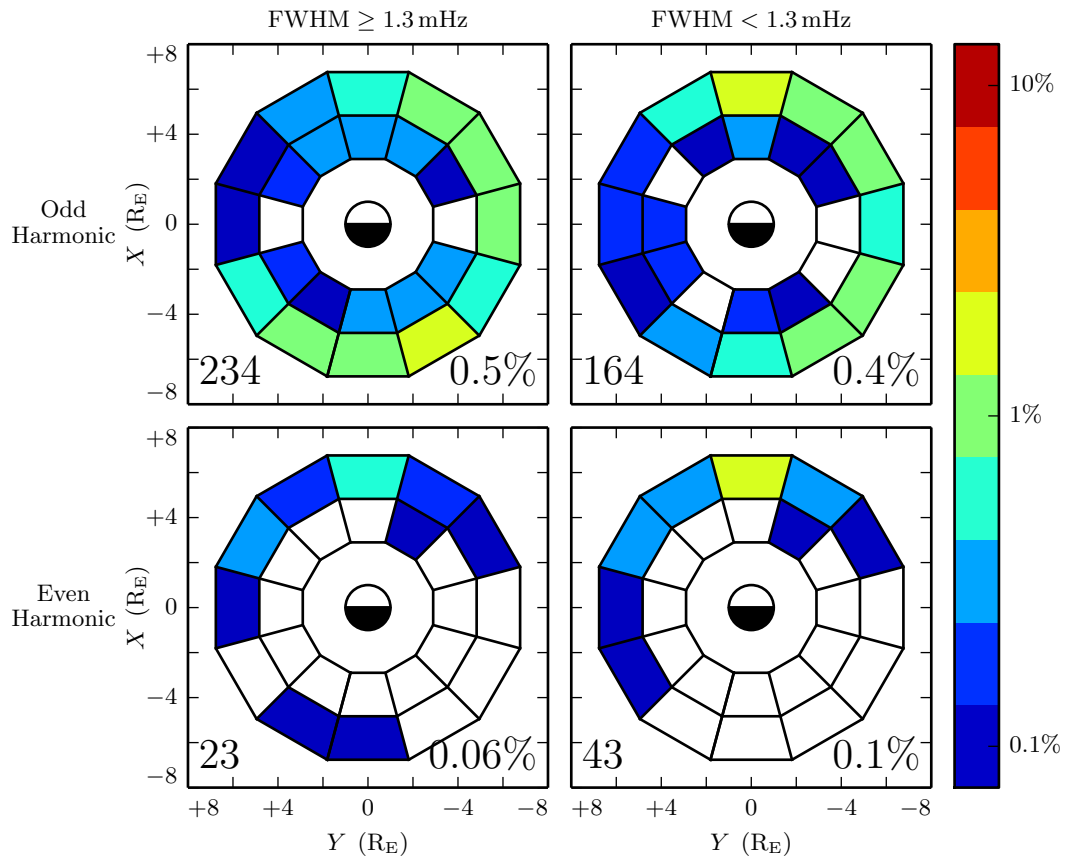


Figure 8.20: **TODO:** ...

Storm Toroidal Pc4 by Spectral Width: $|\text{Im}\tilde{S}| \geq 0.01 \frac{\text{mW}}{\text{m}^2}$, Split at $L=5$

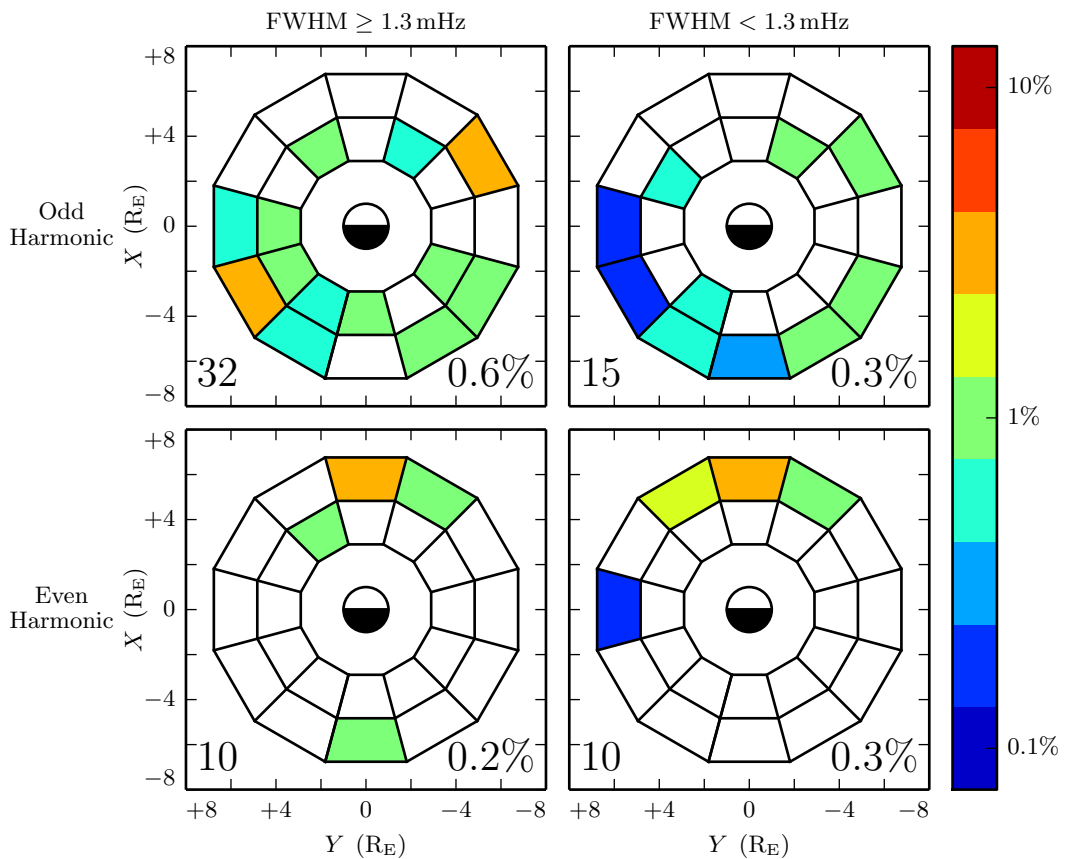


Figure 8.21: TODO: ...

1328 **8.7 Double-Triggering Events**

- 1329 The poloidal and toroidal triggers are checked for events independently. In about 10 %
1330 of cases, both trigger at the same time. In such cases, the poloidal and toroidal event
1331 almost always have the same parity.
- 1332 Odd harmonics are comparably likely to trigger on both the poloidal and toroidal chan-
1333 nels whether or not it's storm time. Even double modes are much more common during
1334 storm time than they are during quiet time.
- 1335 Odd double-triggering events rarely happen twice in the same day — the 24 events in
1336 the top row of Figure 8.22 occur on \sim 20 different dates (and each of the three odd storm
1337 double events is on a different date).
- 1338 Even double-triggering events often happen multiple times in the same day. The 36
1339 calm-time double events are spread over 15 days; the 14 storm double events are spread
1340 over only 7 days.

Itaneous Poloidal + Toroidal Pc4 Occurrence Rate: $|\text{Im}\tilde{S}| \geq 0.01 \frac{\text{mW}}{\text{m}^2}$, Split at

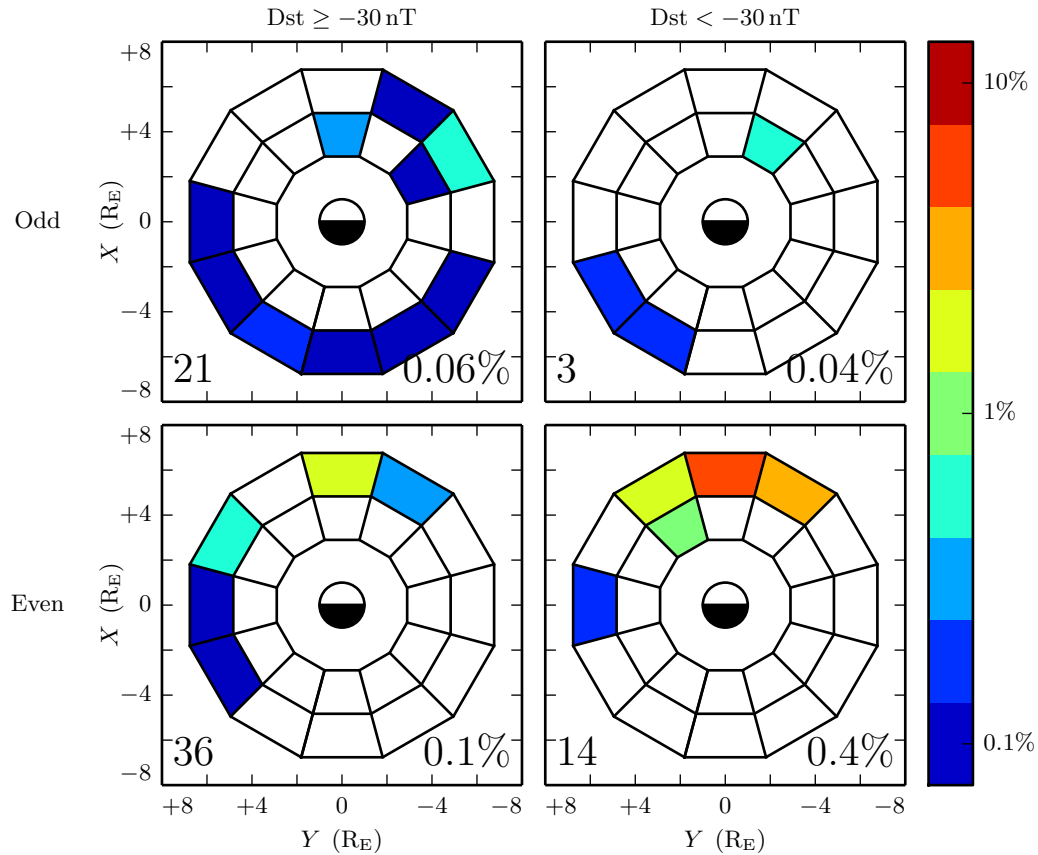


Figure 8.22: **TODO:** ...

1341 8.8 Discussion

1342 **TODO:** ...

1343 **Chapter 9**

1344 **Conclusion**

1345 **9.1 Summary of Results**

1346 TODO: Code development... Chapters 5 and 6

1347 TODO: Make the Git repository public, and link to it.

1348 TODO: Numerical results... Chapter 7

1349 TODO: Re-summarize the Discussion sections, I guess.

1350 TODO: Observational results... Chapter 8

1351 TODO: Link to the Git repository.

1352 **9.2 Future Work**

1353 TODO: Code development.

1354 Arbitrary deformation of grid. Get $\hat{e}_i = \frac{\partial}{\partial u^i} \underline{x}$, then $g_{ij} = \hat{e}_i \cdot \hat{e}_j$, then invert the metric
1355 tensor for contravariant components.

1356 MPI. Time to compute vs time to broadcast. This might make sense for inertial length
1357 scales.

1358 Better ionospheric profiles. Distinction between the dawn and dusk flanks. Maybe even
1359 update the conductivity based on energy deposition — precipitation causes ionization!

1360 IRI ionosphere model. Solar illumination effects.

1361 **TODO: Numerical work.**

1362 More complicated driving. Higher harmonics, non-sinusoidal waveforms. Maybe even
1363 drive based on events?

1364 **TODO: Analysis of RBSP data.**

1365 Basically just do everything over again, twice as well, once the probes have finished
1366 sampling the dayside again.

1367 References

- 1368 [1] S.-I. Akasofu. The development of the auroral substorm. *Planetary and Space*
1369 *Science*, 12(4):273–282, 1964.
- 1370 [2] H. Alfvén. On the cosmogony of the solar system III. *Stockholms Observatoriums*
1371 *Annaler*, 14:9.1–9.29, 1946.
- 1372 [3] B. J. Anderson, M. J. Engebretson, S. P. Rounds, L. J. Zanetti, and T. A. Potemra.
1373 A statistical study of Pc 3-5 pulsations observed by the AMPTE/CCE magnetic
1374 fields experiment, 1. occurrence distributions. *J. Geophys. Res.*, 95(A7):10495,
1375 1990.
- 1376 [4] V. Angelopoulos. The THEMIS mission. *Space Science Reviews*, 141(1-4):5–34,
1377 2008.
- 1378 [5] K. Birkeland. Expédition norvégienne de 1899-1900 pour l'étude des aurores
1379 boréales. *Mat. Naturvidensk. Kl.*, KI(I), 1901.
- 1380 [6] J. P. Boris. A physically motivated solution of the Alfvén problem. *NRL Memo-*
1381 *randum Report*, 2167, 1970.
- 1382 [7] A. Brekke, T. Feder, and S. Berger. Pc4 giant pulsations recorded in Tromsø,
1383 1929-1985. *Journal of Atmospheric and Terrestrial Physics*, 49(10):1027–1032,
1384 1987.
- 1385 [8] C. W. Carlson, R. F. Pfaff, and J. G. Watzin. The fast auroral Snapshot (FAST)
1386 mission. *Geophys. Res. Lett.*, 25(12):2013–2016, 1998.

- 1387 [9] A. A. Chan, M. Xia, and L. Chen. Anisotropic alfvén-balloon modes in Earth's
 1388 magnetosphere. *J. Geophys. Res. Space Physics*, 99(A9):17351–17366, 1994.
- 1389 [10] L. Chen and A. Hasegawa. A theory of long-period magnetic pulsations: 1. steady
 1390 state excitation of field line resonance. *J. Geophys. Res.*, 79(7):1024–1032, 1974.
- 1391 [11] L. Chen and A. Hasegawa. Kinetic theory of geomagnetic pulsations: 1. internal
 1392 excitations by energetic particles. *J. Geophys. Res.*, 96(A2):1503, 1991.
- 1393 [12] L. Chen, R. White, C. Cheng, F. Romanelli, J. Weiland, R. Hay, J. V. Dam,
 1394 D. Barnes, M. Rosenbluth, and S. Tsai. Theory and simulation of fishbone-type
 1395 instabilities in beam-heated tokamaks. Technical report, 1984.
- 1396 [13] C. Z. Cheng and Q. Qian. Theory of ballooning-mirror instabilities for anisotropic
 1397 pressure plasmas in the magnetosphere. *J. Geophys. Res.*, 99(A6):11193, 1994.
- 1398 [14] G. Chisham and D. Orr. Statistical studies of giant pulsations (pgs): Harmonic
 1399 mode. *Planetary and Space Science*, 39(7):999–1006, 1991.
- 1400 [15] W. D. Cummings, R. J. O'Sullivan, and P. J. Coleman. Standing Alfvén waves in
 1401 the magnetosphere. *J. Geophys. Res.*, 74(3):778–793, 1969.
- 1402 [16] L. Dai. Collisionless magnetic reconnection via Alfvén eigenmodes. *Phys. Rev.*
 1403 *Lett.*, 102(24), 2009.
- 1404 [17] L. Dai, K. Takahashi, R. Lysak, C. Wang, J. R. Wygant, C. Kletzing, J. Bonnell,
 1405 C. A. Cattell, C. W. Smith, R. J. MacDowall, S. Thaller, A. Breneman, X. Tang,
 1406 X. Tao, and L. Chen. Storm time occurrence and spatial distribution of Pc4
 1407 poloidal ULF waves in the inner magnetosphere: A Van Allen Probes statistical
 1408 study. *J. Geophys. Res. Space Physics*, 120:4748–4762, 2015.
- 1409 [18] L. Dai, K. Takahashi, J. R. Wygant, L. Chen, J. Bonnell, C. A. Cattell, S. Thaller,
 1410 C. Kletzing, C. W. Smith, R. J. MacDowall, D. N. Baker, J. B. Blake, J. Fennell,
 1411 S. Claudepierre, H. O. Funsten, G. D. Reeves, and H. E. Spence. Excitation of
 1412 poloidal standing Alfvén waves through drift resonance wave-particle interaction.
 1413 *Geophys. Res. Lett.*, 40:4127–4132, 2013.

- 1414 [19] A. W. Degeling, R. Rankin, and Q.-G. Zong. Modeling radiation belt electron
1415 acceleration by ULF fast mode waves, launched by solar wind dynamic pressure
1416 fluctuations. *J. Geophys. Res. Space Physics*, 119(11):8916–8928, 2014.
- 1417 [20] W. D. D’haeseleer, W. N. G. H. J. D. Callen, and J. L. Shohet. *Flux Coordinates*
1418 and *Magnetic Field Structure*. Springer-Verlag, New York, 1991.
- 1419 [21] D. Q. Ding, R. E. Denton, M. K. Hudson, and R. L. Lysak. An MHD simulation
1420 study of the poloidal mode field line resonance in the Earth’s dipole magneto-
1421 sphere. *J. Geophys. Res.*, 100:63–77, 1995.
- 1422 [22] J. W. Dungey. The attenuation of Alfvén waves. *J. Geophys. Res.*, 59(3):323–328,
1423 1954.
- 1424 [23] J. W. Dungey. Interplanetary magnetic field and the auroral zones. *Phys. Rev.*
1425 *Lett.*, 6(2):47–48, 1961.
- 1426 [24] A. Einstein. Die grundlage der allgemeinen relativitätstheorie. *Ann. Phys.*,
1427 354:769–822, 1916.
- 1428 [25] S. R. Elkington, M. K. Hudson, and A. A. Chan. Acceleration of relativistic
1429 electrons via drift-resonant interaction with toroidal-mode Pc-5 ULF oscillations.
1430 *Geophys. Res. Lett.*, 26(21):3273–3276, 1999.
- 1431 [26] M. J. Engebretson, D. L. Murr, K. N. Erickson, R. J. Strangeway, D. M. Klumpar,
1432 S. A. Fuselier, L. J. Zanetti, and T. A. Potemra. The spatial extent of radial
1433 magnetic pulsation events observed in the dayside near synchronous orbit. *J.*
1434 *Geophys. Res.*, 97(A9):13741, 1992.
- 1435 [27] P. T. I. Eriksson, L. G. Blomberg, A. D. M. Walker, and K.-H. Glassmeier. Poloidal
1436 ULF oscillations in the dayside magnetosphere: a Cluster study. *Ann. Geophys.*,
1437 23(7):2679–2686, 2005.
- 1438 [28] S. Fujita and T. Tamao. Duct propagation of hydromagnetic waves in the upper
1439 ionosphere, 1, electromagnetic field disturbances in high latitudes associated with
1440 localized incidence of a shear Alfvén wave. *J. Geophys. Res.*, 93(A12):14665, 1988.

- 1441 [29] K.-H. Glassmeier. Magnetometer array observations of a giant pulsation event. *J.
1442 Geophys.*, 48:127–138, 1980.
- 1443 [30] K.-H. Glassmeier. On the influence of ionospheres with non-uniform conductivity
1444 distribution on hydromagnetic waves. *J. Geophys.*, 54(2):125–137, 1984.
- 1445 [31] K.-H. Glassmeier, S. Buchert, U. Motschmann, A. Korth, and A. Pedersen. Concerning
1446 the generation of geomagnetic giant pulsations by drift-bounce resonance
1447 ring current instabilities. *Ann. Geophysicae*, 17:338–350, 1999.
- 1448 [32] K.-H. Glassmeier, D. Klimushkin, C. Othmer, and P. Mager. ULF waves at
1449 mercury: Earth, the giants, and their little brother compared. *Advances in Space
1450 Research*, 33(11):1875–1883, 2004.
- 1451 [33] C. Goertz. Kinetic alfvén waves on auroral field lines. *Planetary and Space Science*,
1452 32(11):1387–1392, 1984.
- 1453 [34] C. K. Goertz and R. W. Boswell. Magnetosphere-ionosphere coupling. *J. Geophys.
1454 Res.*, 84(A12):7239, 1979.
- 1455 [35] C. A. Green. Giant pulsations in the plasmasphere. *Planetary and Space Science*,
1456 33(10):1155–1168, 1985.
- 1457 [36] J. L. Green and S. Boardsen. Duration and extent of the great auroral storm of
1458 1859. *Advances in Space Research*, 38(2):130–135, 2006.
- 1459 [37] C. Greifinger and P. S. Greifinger. Theory of hydromagnetic propagation in the
1460 ionospheric waveguide. *J. Geophys. Res.*, 73(23):7473–7490, 1968.
- 1461 [38] B. C. Hall. *Lie Groups, Lie Algebras, and Representations*. Graduate Texts in
1462 Mathematics. Springer, New York, second edition, 2015.
- 1463 [39] Y. X. Hao, Q.-G. Zong, Y. F. Wang, X.-Z. Zhou, H. Zhang, S. Y. Fu, Z. Y.
1464 Pu, H. E. Spence, J. B. Blake, J. Bonnell, J. R. Wygant, and C. A. Kletzing.
1465 Interactions of energetic electrons with ULF waves triggered by interplanetary
1466 shock: Van allen probes observations in the magnetotail. *J. Geophys. Res. Space
1467 Physics*, 119(10):8262–8273, 2014.

- 1468 [40] L. Harang. *Pulsations in the terrestrial magnetic records at high latitude stations.*
1469 Grondahl, 1942.
- 1470 [41] O. Hillebrand, J. Muench, and R. L. McPherron. Ground-satellite correlative
1471 study of a giant pulsation event. *Journal of Geophysics Zeitschrift Geophysik*,
1472 51:129–140, 1982.
- 1473 [42] W. J. Hughes. The effect of the atmosphere and ionosphere on long period mag-
1474 netospheric micropulsations. *Planet. Space Sci.*, 22:1157–1172, 1974.
- 1475 [43] W. J. Hughes. Magnetospheric ULF waves: A tutorial with a historical perspec-
1476 tive. In M. J. Engebretson, K. Takahashi, and M. Scholer, editors, *Solar Wind*
1477 *Sources of Magnetospheric Ultra-Low-Frequency Waves*, volume 81 of *Geophys.*
1478 *Monogr.*, pages 1–12. American Geophysical Union, Washington, DC, 1994.
- 1479 [44] W. J. Hughes and D. J. Southwood. The screening of micropulsation signals by
1480 the atmosphere and ionosphere. *J. Geophys. Res.*, 81(19):3234–3240, 1976.
- 1481 [45] W. J. Hughes, D. J. Southwood, B. Mauk, R. L. McPherron, and J. N. Barfield.
1482 Alfvén waves generated by an inverted plasma energy distribution. *Nature*,
1483 275(5675):43–45, 1978.
- 1484 [46] J. A. Jacobs, Y. Kato, S. Matsushita, and V. A. Troitskaya. Classification of
1485 geomagnetic micropulsations. *J. Geophys. Res.*, 69(1):180–181, 1964.
- 1486 [47] T. Karlsson and G. T. Marklund. A statistical study of intense low-altitude electric
1487 fields observed by freja. *Geophys. Res. Lett.*, 23(9):1005–1008, 1996.
- 1488 [48] Y. Kato and T. Tsutomu. Hydromagnetic oscillations in a conducting medium
1489 with hall conduct-ivity under the uniform magnetic field. *Science reports of the*
1490 *Tohoku University. Ser. 5, Geophysics*, 7(3):147–164, 1956.
- 1491 [49] M. C. Kelley. *The Earth’s Ionosphere*. Academic Press, San Diego, second edition,
1492 1989.
- 1493 [50] R. L. Kessel. Solar wind excitation of pc5 fluctuations in the magnetosphere and
1494 on the ground. *J. Geophys. Res.*, 113(A4), 2008.

- 1495 [51] D. Y. Klimushkin, P. N. Mager, and K.-H. Glassmeier. Toroidal and poloidal
1496 Alfvén waves with arbitrary azimuthal wavenumbers in a finite pressure plasma
1497 in the earth's magnetosphere. *Annales Geophysicae*, 22(1):267–287, 2004.
- 1498 [52] S. Kokubun. Observations of Pc pulsations in the magnetosphere: Satellite-ground
1499 correlation. *J. Geomagn. Geoelec*, 32(Supplement2):SII17–SII39, 1980.
- 1500 [53] S. Kokubun, K. N. Erickson, T. A. Fritz, and R. L. McPherron. Local time asym-
1501 metry of Pc 4-5 pulsations and associated particle modulations at synchronous
1502 orbit. *J. Geophys. Res.*, 94(A6):6607–6625, 1989.
- 1503 [54] D.-H. Lee and K. Kim. Compressional MHD waves in the magnetosphere: A new
1504 approach. *J. Geophys. Res.*, 104(A6):12379–12385, 1999.
- 1505 [55] A. S. Leonovich and V. A. Mazur. Structure of magnetosonic eigenoscillations of
1506 an axisymmetric magnetosphere. *J. Geophys. Res.*, 105(A12):27707–27715, 2000.
- 1507 [56] W. Liu, J. B. Cao, X. Li, T. E. Sarris, Q.-G. Zong, M. Hartinger, K. Takahashi,
1508 H. Zhang, Q. Q. Shi, and V. Angelopoulos. Poloidal ULF wave observed in the
1509 plasmasphere boundary layer. *J. Geophys. Res. Space Physics*, 118(7):4298–4307,
1510 2013.
- 1511 [57] W. Liu, T. E. Sarris, X. Li, S. R. Elkington, R. Ergun, V. Angelopoulos, J. Bonnell,
1512 and K. H. Glassmeier. Electric and magnetic field observations of Pc4 and Pc5
1513 pulsations in the inner magnetosphere: A statistical study. *J. Geophys. Res.*,
1514 114(A12), 2009.
- 1515 [58] W. Liu, T. E. Sarris, X. Li, R. Ergun, V. Angelopoulos, J. Bonnell, and K. H.
1516 Glassmeier. Solar wind influence on Pc4 and Pc5 ULF wave activity in the inner
1517 magnetosphere. *J. Geophys. Res.*, 115(A12), 2010.
- 1518 [59] W. Liu, T. E. Sarris, X. Li, Q.-G. Zong, R. Ergun, V. Angelopoulos, and K. H.
1519 Glassmeier. Spatial structure and temporal evolution of a dayside poloidal ULF
1520 wave event. *Geophys. Res. Lett.*, 38(19), 2011.
- 1521 [60] R. L. Lysak. Magnetosphere-ionosphere coupling by Alfvén waves at midlatitudes.
1522 *J. Geophys. Res.*, 109, 2004.

- 1523 [61] R. L. Lysak and D. hun Lee. Response of the dipole magnetosphere to pressure
1524 pulses. *Geophys. Res. Lett.*, 19(9):937–940, 1992.
- 1525 [62] R. L. Lysak and Y. Song. A three-dimensional model of the propagation of Alfvén
1526 waves through the auroral ionosphere: first results. *Adv. Space Res.*, 28:813–822,
1527 2001.
- 1528 [63] R. L. Lysak, C. L. Waters, and M. D. Sciffer. Modeling of the ionospheric Alfvén
1529 resonator in dipolar geometry. *J. Geophys. Res. Space Physics*, 118, 2013.
- 1530 [64] P. N. Mager and D. Y. Klimushkin. Giant pulsations as modes of a transverse
1531 Alfvénic resonator on the plasmapause. *Earth, Planets and Space*, 65(5):397–409,
1532 2013.
- 1533 [65] I. R. Mann, E. A. Lee, S. G. Claudepierre, J. F. Fennell, A. Degeling, I. J. Rae,
1534 D. N. Baker, G. D. Reeves, H. E. Spence, L. G. Ozeke, R. Rankin, D. K. Milling,
1535 A. Kale, R. H. W. Friedel, and F. Honary. Discovery of the action of a geophysical
1536 synchrotron in the Earth’s Van Allen radiation belts. *Nature Communications*, 4,
1537 2013.
- 1538 [66] I. R. Mann and A. N. Wright. Finite lifetimes of ideal poloidal Alfvén waves. *J.
1539 Geophys. Res.*, 100:23677–23686, 1995.
- 1540 [67] I. R. Mann, A. N. Wright, and A. W. Hood. Multiple-timescales analysis of ideal
1541 poloidal Alfvén waves. *J. Geophys. Res.*, 102(A2):2381–2390, 1997.
- 1542 [68] T. Maynard, N. Smith, S. Gonzalez, et al. Solar storm risk to the North American
1543 electric grid. 2013.
- 1544 [69] K. McGuire, R. Goldston, M. Bell, M. Bitter, K. Bol, K. Brau, D. Buchenauer,
1545 T. Crowley, S. Davis, F. Dylla, H. Eubank, H. Fishman, R. Fonck, B. Grek,
1546 R. Grimm, R. Hawryluk, H. Hsuan, R. Hulse, R. Izzo, R. Kaita, S. Kaye, H. Kugel,
1547 D. Johnson, J. Manickam, D. Manos, D. Mansfield, E. Mazzucato, R. McCann,
1548 D. McCune, D. Monticello, R. Motley, D. Mueller, K. Oasa, M. Okabayashi,
1549 K. Owens, W. Park, M. Reusch, N. Sauthoff, G. Schmidt, S. Sesnic, J. Strachan,
1550 C. Surko, R. Slusher, H. Takahashi, F. Tenney, P. Thomas, H. Towner, J. Valley,

- 1551 and R. White. Study of high-beta magnetohydrodynamic modes and fast-ion
1552 losses in PDX. *Phys. Rev. Lett.*, 50(12):891–895, 1983.
- 1553 [70] R. L. McPherron. The role of substorms in the generation of magnetic storms.
1554 *Washington DC American Geophysical Union Geophysical Monograph Series*,
1555 98:131–147, 1997.
- 1556 [71] R. L. McPherron, G. K. Parks, D. S. Colburn, and M. D. Montgomery. Satellite
1557 studies of magnetospheric substorms on august 15, 1968: 2. solar wind and outer
1558 magnetosphere. *J. Geophys. Res.*, 78(16):3054–3061, 1973.
- 1559 [72] T. Motoba, K. Takahashi, J. V. Rodriguez, and C. T. Russell. Giant pulsations on
1560 the afternoonside: Geostationary satellite and ground observations. *J. Geophys.*
1561 *Res. Space Physics*, 120:8350–8367, 2015.
- 1562 [73] NASA. Coordinated data analysis (workshop) web.
- 1563 [74] NASA. Near miss: The solar superstorm of july 2012.
- 1564 [75] M. Nicolet. The collision frequency of electrons in the ionosphere. *Journal of*
1565 *Atmospheric and Terrestrial Physics*, 3(4):200–211, 1953.
- 1566 [76] L. G. Ozeke and I. R. Mann. Energization of radiation belt electrons by ring
1567 current ion driven ULF waves. *J. Geophys. Res.*, 113(A2), 2008.
- 1568 [77] E. M. Poulter, W. Allan, E. Nielsen, and K.-H. Glassmeier. Stare radar observa-
1569 tions of a PG pulsation. *J. Geophys. Res.*, 88(A7):5668, 1983.
- 1570 [78] J. A. Proehl, W. Lotko, I. Kouznetsov, and S. D. Geimer. Ultralow-frequency
1571 magnetohydrodynamics in boundary-constrained geomagnetic flux coordinates.
1572 *J. Geophys. Res.*, 107(A9):1225, 2002.
- 1573 [79] H. R. Radoski. A note on oscillating field lines. *J. Geophys. Res.*, 72(1), 1967.
- 1574 [80] H. R. Radoski. A theory of latitude dependent geomagnetic micropulsations: The
1575 asymptotic fields. *J. Geophys. Res.*, 79, 1974.

- 1576 [81] R. Rankin, J. C. Samson, and V. T. Tikhonchuk. Parallel electric fields in dis-
1577 persive shear alfvén waves in the dipolar magnetosphere. *Geophys. Res. Lett.*,
1578 26(24):3601–3604, 1999.
- 1579 [82] B. Rolf. Giant micropulsations at abisko. *J. Geophys. Res.*, 36(1):9, 1931.
- 1580 [83] G. Rostoker, H.-L. Lam, and J. V. Olson. PC 4 giant pulsations in the morning
1581 sector. *J. Geophys. Res.*, 84(A9):5153, 1979.
- 1582 [84] J. C. Samson, L. L. Cogger, and Q. Pao. Observations of field line resonances,
1583 auroral arcs, and auroral vortex structures. *J. Geophys. Res.*, 101(A8):17373–
1584 17383, 1996.
- 1585 [85] H. J. Singer, W. J. Hughes, and C. T. Russell. Standing hydromagnetic waves
1586 observed by ISEE 1 and 2: Radial extent and harmonic. *J. Geophys. Res.*,
1587 87(A5):3519, 1982.
- 1588 [86] D. J. Southwood. Some features of field line resonances in the magnetosphere.
1589 *Planetary and Space Science*, 22(3):483–491, 1974.
- 1590 [87] D. J. Southwood. A general approach to low-frequency instability in the ring
1591 current plasma. *J. Geophys. Res.*, 81(19):3340–3348, 1976.
- 1592 [88] J. Stratton and N. J. Fox. Radiation belt storm probes (RBSP) mission overview.
1593 In *2012 IEEE Aerospace Conference*. Institute of Electrical & Electronics Engi-
1594 neers (IEEE), 2012.
- 1595 [89] E. Sucksdorff. Giant pulsations recorded at sodankyl during 19141938. *Terrestrial
1596 Magnetism and Atmospheric Electricity*, 44(2):157–170, 1939.
- 1597 [90] K. Takahashi, J. Bonnell, K.-H. Glassmeier, V. Angelopoulos, H. J. Singer, P. J.
1598 Chi, R. E. Denton, Y. Nishimura, D.-H. Lee, M. Nosé, and W. Liu. Multipoint
1599 observation of fast mode waves trapped in the dayside plasmasphere. *J. Geophys.
1600 Res.*, 115(A12), 2010.
- 1601 [91] K. Takahashi, K.-H. Glassmeier, V. Angelopoulos, J. Bonnell, Y. Nishimura, H. J.
1602 Singer, and C. T. Russell. Multisatellite observations of a giant pulsation event.
1603 *J. Geophys. Res.*, 116:A11223, 2011.

- 1604 [92] K. Takahashi, M. D. Hartinger, V. Angelopoulos, K.-H. Glassmeier, and H. J.
1605 Singer. Multispacecraft observations of fundamental poloidal waves without
1606 ground magnetic signatures. *J. Geophys. Res. Space Physics*, 118:4319–4334, 2013.
- 1607 [93] K. Takahashi, R. W. McEntire, A. T. Y. Lui, and T. A. Potemra. Ion flux oscillations
1608 associated with a radially polarized transverse Pc 5 magnetic pulsation. *J.
1609 Geophys. Res.*, 95(A4):3717, 1990.
- 1610 [94] K. Takahashi, N. Sato, J. Warnecke, H. Lühr, H. E. Spence, and Y. Tonegawa.
1611 On the standing wave mode of giant pulsations. *J. Geophys. Res. Space Physics*,
1612 97(A7):10717–10732, 1992.
- 1613 [95] B. J. Thompson and R. L. Lysak. Electron acceleration by inertial alfvén waves.
1614 *J. Geophys. Res.*, 101(A3):5359–5369, 1996.
- 1615 [96] S. M. Thompson and M. G. Kivelson. New evidence for the origin of giant pulsations.
1616 *J. Geophys. Res.*, 106(A10):21237–21253, 2001.
- 1617 [97] V. T. Tikhonchuk and R. Rankin. Electron kinetic effects in standing shear alfvén
1618 waves in the dipolar magnetosphere. *Physics of Plasmas*, 7(6):2630, 2000.
- 1619 [98] B. T. Tsurutani, W. D. Gonzalez, G. S. Lakhina, and S. Alex. The extreme
1620 magnetic storm of 12 september 1859. *Journal of Geophysical Research: Space
1621 Physics*, 108(A7), 2003. 1268.
- 1622 [99] A. Y. Ukhorskiy. Impact of toroidal ULF waves on the outer radiation belt elec-
1623 trons. *J. Geophys. Res.*, 110(A10), 2005.
- 1624 [100] J. Veldkamp. A giant geomagnetic pulsation. *Journal of Atmospheric and Ter-
1625 restrial Physics*, 17(4):320–324, 1960.
- 1626 [101] J. A. Wanliss and K. M. Showalter. High-resolution global storm index: Dst versus
1627 sym-h. *Journal of Geophysical Research: Space Physics*, 111(A2):n/a–n/a, 2006.
1628 A02202.
- 1629 [102] C. L. Waters, R. L. Lysak, and M. D. Sciffer. On the coupling of fast and shear
1630 Alfvén wave modes by the ionospheric Hall conductance. *Earth Planets Space*,
1631 65:385–396, 2013.

- 1632 [103] C. L. Waters and M. D. Sciffer. Field line resonant frequencies and ionospheric
1633 conductance: Results from a 2-d MHD model. *J. Geophys. Res.*, 113(A5), 2008.
- 1634 [104] D. M. Wright and T. K. Yeoman. High-latitude HF doppler observations of ULF
1635 waves: 2. waves with small spatial scale sizes. *Ann. Geophys.*, 17(7):868–876,
1636 1999.
- 1637 [105] J. R. Wygant, A. Keiling, C. A. Cattell, R. L. Lysak, M. Temerin, F. S. Mozer,
1638 C. A. Kletzing, J. D. Scudder, V. Streitsov, W. Lotko, and C. T. Russell. Evidence
1639 for kinetic alfvn waves and parallel electron energization at 46 re altitudes in the
1640 plasma sheet boundary layer. *Journal of Geophysical Research: Space Physics*,
1641 107(A8):SMP 24–1–SMP 24–15, 2002.
- 1642 [106] B. Yang, Q.-G. Zong, Y. F. Wang, S. Y. Fu, P. Song, H. S. Fu, A. Korth, T. Tian,
1643 and H. Reme. Cluster observations of simultaneous resonant interactions of ULF
1644 waves with energetic electrons and thermal ion species in the inner magnetosphere.
1645 *J. Geophys. Res.*, 115(A2), 2010.
- 1646 [107] K. Yee. Numerical solution of initial boundary value problems involving maxwell's
1647 equations in isotropic media. *IEEE Trans. Antennas Propagat.*, 14(3), 1966.
- 1648 [108] T. K. Yeoman and D. M. Wright. ULF waves with drift resonance and drift-bounce
1649 resonance energy sources as observed in artificially-induced HF radar backscatter.
1650 *Ann. Geophys.*, 19(2):159–170, 2001.
- 1651 [109] Q.-G. Zong, X.-Z. Zhou, X. Li, P. Song, S. Y. Fu, D. N. Baker, Z. Y. Pu, T. A.
1652 Fritz, P. Daly, A. Balogh, and H. Réme. Ultralow frequency modulation of ener-
1653 getic particles in the dayside magnetosphere. *Geophys. Res. Lett.*, 34(12), 2007.
- 1654 [110] Q.-G. Zong, X.-Z. Zhou, Y. F. Wang, X. Li, P. Song, D. N. Baker, T. A. Fritz,
1655 P. W. Daly, M. Dunlop, and A. Pedersen. Energetic electron response to ULF
1656 waves induced by interplanetary shocks in the outer radiation belt. *J. Geophys.*
1657 *Res.*, 114(A10), 2009.